Model-based Analysis of Temporal Patterns in Atrioventricular Node Conduction During Atrial Fibrillation

Karlsson, Mattias

2022

Document Version:
Publisher's PDF, also known as Version of record

Model-based Analysis of Temporal Patterns in Atrioventricular Node Conduction During Atrial Fibrillation

Mattias Karlsson

Department of Biomedical Engineering
Faculty of Engineering
Lund University

Model-based Analysis of Temporal Patterns in Atrioventricular Node Conduction During Atrial Fibrillation

Mattias Karlsson

LUND
UNIVERSITY

Licentiate Dissertation
Biomedical Engineering
Lund, December 2022

Dissertation for the degree of Licentiate of Engineering in Biomedical Engineering.

Department of Biomedical Engineering
Lund University
P.O. Box 118, SE-221 00 LUND, SWEDEN

ISBN: 978-91-8039-483-3 (print)
ISBN: 978-91-8039-484-0 (pdf)
ISRN: LUTEDX/TEEM-1132-SE
Report No. 5/22
Printed in December 2022 Sweden by *Tryckeriet i E-huset*, Lund.

Dedicated to Patrik Nilsson.
The man who started it all.

Populärvetenskaplig sammanfattning

Förmaksflimmer är den vanligaste arytmin inom den vuxna befolkningen och antas drabba mellan 1 av 3 och 1 av 4 under deras livstid [5]. Under förmaksflimmer slår hjärtat både oregelbundet och ovanligt fort, vilket leder till försämrat blodflöde i kroppen. Även om de allra flesta klarar av att ha förmaksflimmer utan allvarliga direkta följder så ökar risken för både blodproppar och stroke.

Patienter med permanent förmaksflimmer ges oftast läkemedel som minskar pulsen, vanligtvis betablockerare eller kalciumflödeshämmare. Man behöver ofta pröva olika läkemedel innan man hittar ett som fungerar bra. Detta prövande tar både tid och riskerar att landa i ett läkemedel som fungerar tillräckligt bra, men ej optimalt.

Under förmaksflimmer regleras pulsen till stor del av atrioventrikulärknutan (AV-knutan). Detta leder till att de elektrofysiologiska egenskaperna hos denna knuta till stor del avgör läkemedelsutfallet. Att kunna uppskatta dessa elektrofysiologiska egenskaper, och se hur de påverkas av olika läkemedel, är därför av stort intresse.

I denna avhandling har en matematisk modell av AV-knutan skapats, tillsammans med ett ramverk för robust och effektiv skattning av modellparametrar baserat på enbart EKG-mätningar. Vi har dessutom visat att olika läkemedelstyper på en populationsnivå påverkar de elektrofysiologiska egenskaperna i AV-knutan på olika sätt. Detta, tillsammans med att vi kan skatta de elektrofysiologiska egenskaperna hos AV-knutan för enskilda individer, utgör ett viktigt steg mot att kunna förutse läkemedelseffekter och på så sätt stötta och hjälpa till med val av läkemedel under förmaksflimmer.

Abstract

The lifetime risk of developing atrial fibrillation (AF) is estimated to be between 1 in 3 to 1 in 4 individuals, making it the most common arrhythmia in the world [5]. For persistent AF, rate control drugs with the purpose to affect the conduction properties of the atrioventricular (AV) node are the most common treatment. The drug of choice varies between β-blockers and calcium channel blockers, often chosen empirically. This can lead to long periods of time before sufficient treatment is found. However, due to the physiological differences between the drug types, it could be possible to predict the effect of the drugs and thus assist in treatment selection. The main focus of this thesis is therefore to assess drug-dependent differences in the AV node, using non-invasive measurements.

This thesis comprises an introduction to the subject as well as two papers. The first paper proposes a framework for assessing the conduction properties of the AV node non-invasively using a mathematical model of the AV node in combination with a genetic algorithm.

The second paper is a continuation of the work in paper I, where the proposed workflow was adapted to assess the drug-dependent effect on the AV node of four different rate control drugs during a period of 24 hours.

The methods presented in this thesis have made it possible to assess both the refractory period and the conduction delay in the AV node in a robust way using ECG, and by doing so found population-related differences in AV node conduction properties between drug types.

List of Publications

Included

The licentiate dissertation is based on two journal publications. The publications are included in the order listed below.

[1] Mattias Karlsson, Frida Sandberg, Sara Ulimoen, and Mikael Wallman "Non-invasive Characterization of Human AV-Nodal Conduction Delay and Refractory Period During Atrial Fibrillation," in *Frontiers in Physiology*, pp. 1849, 2021.

[2] Mattias Karlsson, Mikael Wallman, Pyotr Platonov, Sara Ulimoen, and Frida Sandberg "ECG Based Assessment of Circadian Variation in AV-nodal Conduction During AF – Influence of Rate Control Drugs," in *Frontiers in Physiology*, pp. 2015, 2022.

The author has contributed to the papers as follows.

Paper I. Contributed to the conception and design of the study and performed the analysis. Designed the model changes as well as the genetic algorithm for parameter estimation. Drafted and wrote the manuscript.

Paper II. Contributed to the conception and design of the study and performed the analysis. Designed the genetic algorithm, the method for uncertainty estimation, and the mixed-effect model for calculating the circadian variation. Drafted and wrote the manuscript.

Related

Parts of the work have been presented at conferences. The related conference papers listed below are not included in the thesis.

[3] Mattias Karlsson, Mikael Wallman, Sara Ulimoen, and Frida Sandberg "Non-invasive Characterization of Human AV-Nodal Conduction Delay and Refractory Period During Atrial Fibrillation," in Computing in Cardiology, Brno, Czech Republic, September, 2021.

[4] Mattias Karlsson, Mikael Wallman, Pyotr Platonov, Sara Ulimoen, and Frida Sandberg "Drug Dependent Circadian Variations in AV-nodal Properties During Atrial Fibrillation," in Computing in Cardiology, Tampere, Finland, September, 2022.

Acknowledgments

As with most things in life, this thesis is not entirely self-made. I have over the years leading up to this thesis had support from friends and colleagues, and some of which I see as both. First, I would like to thank the two most influential persons regarding this work, my two main supervisors Mikael Wallman and Frida Sandberg. Thank you both for all time spent reading my scratchy first drafts and helping me transform them into something readable. I would also like to thank my boss and supervisor Mats Jirstrand for his support in all things work-related. Furthermore, I would also like to thank Pyotr Platonov for his supervision regarding everything medical.

I spend most of my working hours in Gothenburg, thus this acknowledgment would not be complete without a big thank you to my colleagues at FCC. A special thanks go out to my fellow Ph.D. students Marcus, Viktor, and Julia, for all lunches, fikas, and afterworks. Even though I spend most of my time in Gothenburg, a significant part of my years is now spent in Lund. I would therefore also like to thank my colleagues at BME in Lund, with special thanks to my fellow Ph.D. students in the signal processing group Felix, Mostafa, and Hesam, with an extra special thanks to Felix for the creation of Figure 2.1. Moreover, a special thanks also go to my office mates Johan and Lorenzo for making my office hours in Lund something special.

In addition, I would also like to thank my friends and family. Not necessarily for any help on this thesis, but for making my free time so much better. The final thanks goes to Patrik Nilsson, to whom this thesis is dedicated to. You taught me to be proud of my achievements in school, that science was worth pursuing, and overall started it all.

Mattias Karlsson
Göteborg, November, 2022

Contents

Part I

Introduction

Chapter 1
Background and Aim

This chapter gives a short introduction to the background and aims of this thesis. Firstly, atrial fibrillation (AF) is introduced followed by a description of the idea and application of mathematical modeling, in Section 1.1, followed by the motivation and aim for the thesis, in Section 1.2, before the outline of the thesis is presented, in Section 1.3.

1.1 Background

Atrial fibrillation is the most common arrhythmia in the world, characterized by rapid and irregular contraction of the atria, originating from a highly disorganized electrical activity [5]. The prevalence of AF in the European Union per age group is shown in Figure 1.1, where a clear correlation with age can be seen. Atrial fibrillation is also associated with an increased risk of mortality, mainly due to heart failure or stroke [6, 7].

During AF, the ventricles are partly protected from the highly disorganized electrical activity of the atria by the atrioventricular (AV) node, which acts as a gatekeeper between the atria and the ventricles. The AV node is capable of blocking and delaying incoming impulses, preventing the ventricles from having as rapid and irregular contraction as the atria. However, the blocking and delaying of impulses performed by the AV node are in many cases not sufficient to maintain a healthy heart rate.

Fortunately, the conduction properties of the AV node can be modified using rate control drugs. There are mainly two different types of rate control drugs used for AF treatment, β-blockers and calcium channel blockers, with different physiological effects [5]. On a population level, both drug types have been shown to reduce the heart rate [8]. However, on an individual level, they can have vastly different impacts on

the ventricular activation rate, and the ultimate choice of drug type for a given patient is often made empirically [5]. One of the main physiological differences between the two drug types is their effect on the autonomic nervous system (ANS), which is also known to affect the maintenance and initiation of AF. Thus, patient-specific information about the ANS could potentially aid in therapeutic choices. In this thesis, we focus on quantifying circadian variation in AV-nodal conduction properties as a marker for ANS modulation. However, directly measuring the conduction properties in the AV node during AF non-invasively is not possible, thus, another approach is needed.

Mathematical models have long been used as a tool to describe the world, analyze the interaction between components of complex systems, and make predictions. From Newton's law to Maxwell's equations, models are used in every field of science and engineering, and with the ever-increasing computing power at hand, mathematical models are now more used than ever. A model aims to represent a real-world system in an objective, simplified, and useful way. Due to the nature of a model, all models are wrong. However, they can still be useful. A common usage of models is to fit them to data in order to draw conclusions about reality, which indeed is what we will be using the models for in this thesis.

By using a mathematical model of the AV node, it is possible to assess temporal patterns in the conduction properties from electrocardiogram (ECG) recordings, thereby making it possible to assess circadian variation and indirectly the impact of the ANS. To make a model useful in a clinical setting, it should preferably only use non-invasive data for the fitting to reduce the risk of complications.

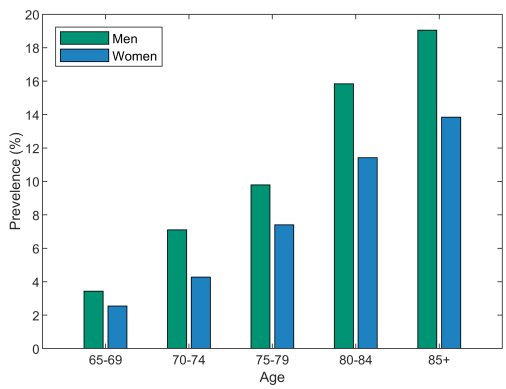

Figure 1.1: Prevalence of AF in the Italian population, assumed representative for the European Union, stratified by age and gender [9].

1.2 Motivation and Aims

The hypothesis is thus that circadian variation in the AV node properties can provide information useful for assisting in treatment selection. Therefore, the overall goal is to quantify the circadian variations in the AV node properties during baseline and under the influence of different rate control drugs in a robust and non-invasive way. This is addressed in this research by the following three aims:

Aim 1: To create a mathematical model of the AV node during AF capable of detailed physiological insights on an individual level.

Aim 2: To estimate model parameters in a robust and computationally efficient way using non-invasive data.

Aim 3: To apply the model and estimation method to patient data at baseline and under the influence of different types of drugs to analyze drug-dependent differences in the circadian variation in the AV node properties.

1.3 Thesis Outline

This thesis comprises two parts, the introduction (part I) and the two included papers (part II). Part I contains seven chapters. In Chapter 1, Background and Aim, the background to AF and mathematical modeling together with the aims of this thesis are found. Chapter 2, The Human Cardiovascular System, introduces the anatomy of the heart, with focus on the conduction system, which needs to be understood before modeling the heart during AF. In Chapter 3, Atrial Fibrillation, the origination, treatment options, and ECG during AF are described, to give a deeper understanding of the heart condition. Chapter 4, Cardiac Modeling, switches the focus from medical to engineering. The chapter contains an introduction to cardiac modeling as well as an overview of previous models of the AV node including the model presented in paper I. Further, in Chapter 5, Model Fitting and Parameter Estimation, optimization is introduced together with several optimization algorithms, which are needed in order to find model parameters resulting in model outputs resembling data. As the name suggests, Chapter 6, Summary of Papers, includes a summary of the two included papers found in part II. Finally, in Chapter 7, Outlook and Conclusion, the potential future research areas relating to this work are presented, as well as a conclusion for the thesis.

Chapter 2

The Human Cardiovascular System

Before it is possible to understand the function of the heart during AF, it is necessary to understand it during normal sinus rhythm. In this section, the anatomy of the heart will firstly be presented, in Section 2.1; from the overall mechanics down to the cellular events that make a heart beat. Secondly, the conduction system of the heart will be introduced in Section 2.2, including the sinoatrial (SA) node and the AV node.

2.1 Cardiac Anatomy and Mechanical Function

The main function of the heart is to pump blood around in the body, oxygenating the cells. As shown in Figure 2.1, the heart consists of four chambers; two atria and two ventricles. Deoxygenated blood returns from the body to the heart via the superior and inferior vena cava to the right atrium, which then contracts and pumps it into the right ventricle. The right ventricle then pumps the blood to the lungs via the left and right pulmonary arteries, where it releases carbon dioxide and receives oxygen. This blood returns to the heart into the left atrium via the left and right pulmonary veins. The left atrium then pumps the blood into the left ventricle, which in turn pumps it back into the body via the aorta. In order for the chambers to pump the blood, they need to be able to contract, thus the chambers consist mostly of cardiac muscle tissue – the myocardium. The thickness of the myocardium section of the heart walls differs between chambers to match the different functions. The atria have thinner walls compared to the ventricles since the workload is less, and the left ventricle – which pumps blood throughout the whole body – has thicker walls than the right ventricle.

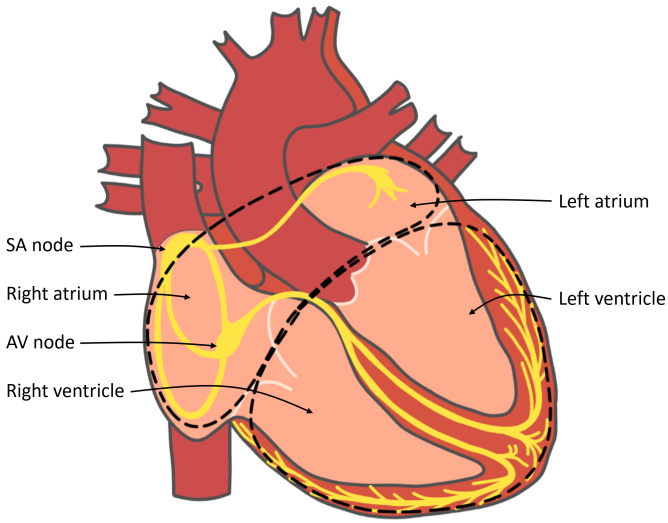

Figure 2.1: A schematic figure of the human heart with the conduction system highlighted in yellow. The figure was created by Felix Plappert with inspiration from [10].

2.1.1 Cardiomyocytes

The myocardium is made up of cardiac muscle cells, the cardiomyocytes. Each cardiomyocytes contains long contractile fibers, the myofibrils, which in turn contain both thick filaments (myosin) and thin filaments (actin) that are responsible for the contraction of the cells [11]. The contraction occurs when the heads of the myosin bind to the actin and forms a cross-bridge between the filaments. Each myosin head contains adenosine triphosphate – an organic compound that provides energy in living cells – which it splits to receive energy, pulling the thick and thin filaments towards each other shortening the myofibril. After that, the myosin head binds to another adenosine triphosphate, detaches from the actin, and starts this process over again. All the myosin heads in one myofibril work together to contract that specific myofibril, and all myofibrils in each cell work together to contract that specific cell. For a contraction of a whole chamber to occur, all the myocytes in said chamber contract. However, this does not happen spontaneously. The myosin heads in a relaxed muscle cell are blocked from binding due to the protein tropomyosin covering the binding sites. When these blocking tropomyosins bind to calcium ions (Ca^{2+}), they change shape and cease to block. The Ca^{2+} originates from the sarcoplasmic reticulum storing Ca^{2+} inside the cells, and from outside the cells transmitted through Ca^{2+}-specific ion channels as well as the T-tubules during an action potential – a rapid rise and fall in membrane potential across the cell membrane [11].

The generation of said action potential depends mainly on two components; the existence of specific types of ion channels and a resting potential. The specific types of channels allow different ions to diffuse across the plasma membrane, where the direction of diffusion occurs from higher to lower concentration, creating an ionic current that changes the membrane potential. The ion channels are guarded by a gate, controlling when and if ions can pass through. There are two types of ion channels contributing to the action potential, the leaky channels, which open and close seemingly randomly, and the voltage-gated channels, which open in response to a change in the membrane potential. The difference in voltage between the inside and the outside of the plasma membrane in a cardiomyocyte is created by outflow of potassium ions (K^+) through numerous leaky K^+ channels and inflow of sodium ions (Na^+) through other, fewer, leaky Na^+ channels. This, combined with sodium-potassium pumps, pumping Na^+ out and K^+ into the cell, creates a stable resting membrane potential.

However, when a stimulus (e.g. an influx of ions from an adjacent cell) causes the membrane potential to change from the resting potential above a threshold level, an action potential is initiated in the cell, as shown in phase 4 in Figure 2.2a. This stimulus starts phase 0 and activates the voltage-gated Na^+ channels, rapidly raising the membrane potential by the influx of Na^+ [12]. The Na^+ gates are only open for a short amount of time before closing, which together with the opening of K^+ channels starts the decrease in membrane potential, causing phase 1. Moreover, Ca^{2+} channels are also activated during phase 0, although with a slower opening and closing, causing the influx of Ca^{2+} to occur later than the Na^+ and persist for longer. This inflow of Ca^{2+} together with the outflow of K^+ causes the plateau shown in phase 2. Phase 3 starts with the closing of the Ca^{2+} channels, resulting in re-polarization of the cell by the K^+ channels. This results in a resting potential and phase 4. Each cardiac muscle cell is connected to adjacent muscle cells by intercalated discs. These discs contain gap junctions, allowing a rapid flow of ions between cells, thereby propagating potential changes and initiating new action potentials [12].

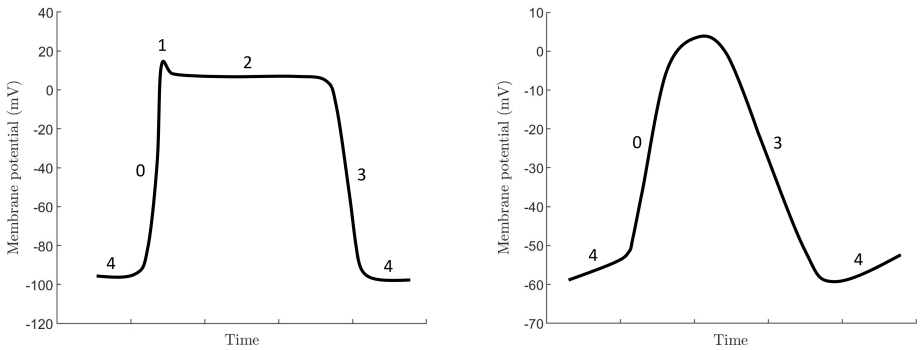

(a) Cardiomyocyte **(b)** Pacemaker cell

Figure 2.2: Action potential in a cardiomyocyte (a) and in a pacemaker cell (b). Note that there is no distinct phase in the pacemaker cell resembling phase 1 or 2 in the cardiomyocyte.

2.2 Conduction System of the Heart

The action potential starting the contraction of the myocardium begins in the SA node, located in the right atrial wall, and propagates throughout the whole conduction system. The SA node creates a new action potential periodically, with a rate determent by the blood demand of the body. The blood demand, and in turn the rate of the SA node, is regulated by the ANS. The action potential from the SA node is conducted by gap junction in the intercalated discs throughout both atria, resulting in simultaneous contraction.

Before the action potential reaches the ventricles, it is conducted through the lone conduction point between the chambers, the AV node. The action potential propagates from the SA node to the AV node via the three internodal pathways, as shown in Figure 2.1, which have a higher conduction velocity compared to the other myocardium in the atria [13]. The AV node acts as a gatekeeper, delaying or blocking incoming electrical impulses based on the impulse rate. The evolutionary reason for this delay is to regulate the timing between atrial and ventricular contractions for efficient pumping of blood. When the AV node conducts an impulse, it arrives at the bundle of His, which splits into the right and left bundle branches. The impulse then conducts through these branches to the Purkinje fibers, activating the contraction of the ventricles. The Purkinje fibers consist of specialized cardiomyocytes which give rise to a higher conduction velocity than other cardiomyocytes and the internodal pathways [14]. This structured conduction route is altered during cardiac arrhyth-

mias, such as AF. During AF, the normal function of the SA node is blocked by the rapid electrical activations of the surrounding tissue, leaving it unable to initiate a new action potential. Instead, the AV node plays a more significant role.

2.2.1 Sinoatrial node

As previously mentioned, cardiac electrical activation is normally initiated by the SA node. In healthy hearts, the SA node keeps a steady pace of electrical activation. To achieve this, the SA node consists of a specialized group of cardiomyocytes known as pacemaker cells, which continuously produce action potentials and in turn sets the rhythm of the heart. In contrast to the other cardiomyocytes, the pacemaker cells do not have a resting potential but instead begin to depolarize automatically immediately after re-polarization. In order for the SA node to keep a steady pace of electrical activation, specific anatomy and a unique set of ion channels are necessary. In the non-SA node myocardium, a steady outward current of K^+ ions by leaky K^+ channels is present, creating a stable resting potential. This stable potential is absent in the SA node, which, together with four inward ion currents, makes pacemaking possible. The action potential in pacemaker cells is shown in Figure 2.2b, and can be divided into three phases; a pacemaker potential phase (4), a depolarization phase (0), and a repolarization phase (3). The numbering of these phases is in relation to the five phases for the action potential in non-pacemaker cardiomyocytes, as shown in 2.2a. The most significant difference between the action potential in the cardiomyocyte and in the pacemaker cells exists in phase 4, the resting potential phase. Phase 4 in the pacemaker cardiomyocytes occurs directly after repolarisation, where the majority of K-channels close, reducing the K^+ ion current outward from the cell [15]. The highly negative membrane potential of the cell also activates the hyperpolarization-activated cyclic nucleotide-gated channels, increasing the pacemaker potential by an inward K^+ and Na^+ current. Further increase of the pacemaker potential is created by the release of stored calcium inside the sarcoplasmic reticulum. This extra calcium is then exchanged by a trade of one Ca^{2+} to three Na^+, creating an inwards current. The last part of phase 4 is the opening of the so-called T-type Ca^{2+} channels, a fast-opening type of Ca^{2+} channel, as well as the slow-opening of the so-called L-type Ca^{2+} channels, transporting Ca^{2+} back into the cell. Both of these are voltage-gated channels, activated when the membrane potential reaches a certain threshold. During phase 0, the membrane potential rises rapidly due to the now fully opened L-type channels, and both the T-type channel and the hyperpolarization-activated cyclic nucleotide-gated channels close. In phase 3, the L-type channels close and the K^+ channels open. This re-polarizes the membrane potential, creates the electrical impulse that will later activate the heart, and sets up the situation in which phase 4 starts from [15].

2.2.2 Atrioventricular node

The function of the AV node is twofold. The most important part for a healthy heart is its ability to delay incoming electrical impulses, which is important in order to optimize the pumping of the heart. This delay of the electrical impulses is partly caused by a lower number of gap junctions connecting the cells in the AV node and by the relatively small diameter of the AV node cells [16]. The diameter for AV nodal cells is 7 μm, compared to 50 μm for the Purkinje fibers [16]. Additionally, the action potential of the AV node has a slow upstroke, caused by an absence of a large Na^+ channel density, instead leaving the slower Ca^{2+} channels as the main driver of the upstroke phase [17]. The other function of the AV node is to filter out high frequencies among the atrial impulses, which it achieves by blocking impulses. This blocking occurs when the cells in the AV node are in their refractory state.

Complex blocking and delaying patterns are possible in the AV node due to its dual pathway electrophysiology. The AV node has been found to functionally have two different pathways, one fast pathway (FP) and one slow pathway (SP) [18, 19]. The refractory period of the FP is longer, but it conducts impulses faster compared to the SP. The structure of the cardiomyocytes within the pathways differ, where the FP has longer cells with a larger diameter and the SP shorter cells with a smaller diameter [17]. The dual pathways are thought to be the main components of the complex behavior of the AV node. It has been shown that during a standard S1-S2 protocol – when electrodes are used to deliver impulses in a pulse train at a constant interval (S1) between pulses, followed by a single premature pulse after a shorter interval (S2) – the conduction occurred consistently through the FP for S2 rates slower than 600 ms [19]. Furthermore, for faster S2 rates, the AV node used both the FP and the SP [19]. However, the precise anatomical and molecular substrate of these pathways are not yet fully understood [20]. Moreover, the AV node junction plays an important role in the AV node conduction properties [21]. Based on electrophysiological recordings of the rabbit AV node junction, different types of AV node cells have been classified; the atrial-nodal cells, the nodal cells, and the nodal-His cells [22, 23].

Another important factor of the AV node is its ability to be affected by concealed conduction, a partial activation of the AV node that does not result in ventricular activation. Even without a direct outcome, the concealed conduction can still impact the conduction characteristics of the AV node for subsequent impulses [24]. Moreover, the AV node can also function as a pacemaker if the SA node is non-functioning, with an intrinsic activation rate of 20-60 times per minute [17].

Chapter 3
Atrial Fibrillation

In order to create a mathematical model of the AV node during AF, it is first necessary to understand the cardiac arrhythmia itself. This chapter will therefore start (Section 3.1) by discussing the origination and classification of AF, followed by information about the different methods for AF treatments (Section 3.2), before a brief explanation of the ECG during AF is covered (Section 3.3).

3.1 Origination of Atrial Fibrillation

As stated before, AF is categorized by rapid and irregular electrical activity in the atrial chambers, affecting the beating of both atria and ventricles. Atrial fibrillation originates when the electrical signal activating the atrium does not terminate properly, but instead whirls in chaotic patterns that extinguish the normal activation from the SA node. For AF to be present, there needs to be a trigger in the atrial myocardium. This trigger has been proposed to arise from several different phenomena, further strengthening the argument for individual treatment. One such trigger is the Ca^{2+} handling instability, where increased spontaneous release events of sarcoplasmic reticulum Ca^{2+} trigger the fibrillation [25]. Other studies of the triggers found that over 90% of the triggers originated from the pulmonary veins, the majority in the left superior vein [26, 27].

However, a trigger by itself is not enough for AF to occur. There are also factors related to the maintenance of AF necessary for a trigger to result in AF [28]. To this day, there is still an ongoing debate about the mechanisms responsible for the perpetuation of AF [29, 30], mainly between multi-wavelet reentry and focal drivers [31]. In addition, the structure and electrical re-modeling of the atria are the main factors for the perpetuation of AF, where the electrophysiology of the cardiomyocytes

changes due to activation of fibroblasts, deposition of enhanced connective tissue, and fibrosis [5]. The main electrical change is the slowing of conduction velocity in the cardiomyocytes located in the atria, originating from changes to the L-type Ca^{2+} channels [32]. This can be caused by structural heart disease and hypertension, but also by AF itself. Thus, AF begets AF [33]. All this results in different patients with similar AF symptoms having different underlying physiological reasons, creating a need for individualized treatment.

Atrial fibrillation can be classified into five different types; first diagnosed AF, if it has not been diagnosed before; paroxysmal AF, if it terminates within seven days; persistent AF, if it lasts longer than seven days or requires intervention for restoration of sinus rhythm (cardioversion); long-standing persistent AF, if it continues for over a year; and permanent AF, when it is accepted by both patient and physician [5]. For permanent AF, the long-term variation – mainly regulated by the ANS – is of interest, since the two recommended first-line rate control drug types, β-blockers and calcium channel blockers, have different physiological effects in this regard.

3.2 Treatments

There are three main treatment goals for patients with AF. The first is ischemic stroke prevention by anticoagulation therapy, which reduces the risk of stroke but does not affect AF directly [5, 28]. The second treatment is heart rate control aimed at achieving normal heart rate during ongoing AF, to improve quality of life and reduce the risk of other heart-related problems such as a decrease in ventricular contractile function. Rate control does not aim to terminate AF, but strives toward reducing the heart rate [28]. The third one is rhythm control, used to prevent AF or restore normal rhythm during AF. Rhythm control is mostly used for patients where rate control has been ineffective, or for patients who remain symptomatic despite adequate rate control [28].

3.2.1 Rhythm control

Rhythm control includes both the restoration and maintenance of normal sinus rhythm. Acute restoration of sinus rhythm can be achieved either by electrical cardioversion using electrodes applied on the chest or with pharmacological cardioversion using antiarrhythmic drugs. For pharmacological cardioversion of recent onset AF, vernakalant, flecainide, and propafenone are recommended [5, 34, 35, 36]. Long-term maintenance of sinus rhythm can be archived either by antiarrhythmic drugs or via catheter ablation, where the latter is accomplished by isolation of the pulmonary veins

and in some cases additional ablation lines in the atria. Furthermore, catheter ablation has shown to be more effective than antiarrhythmic drugs if performed by experienced teams [37].

3.2.2 Rate control

Rate control is an integral part of AF treatment and management, and is recommended in most patients suffering from AF [5]. Even if, in some patients, the high ventricular rate has no direct impact on the patient, there is still a risk of heart complications such as reduction of cardiac pumping capacity if left untreated [28]. There are several pharmacological treatments used for rate control, such as β-blockers, non-dihydropyridine calcium channel blockers, and digitalis. However, only β-blockers and calcium channel blockers are recommended as first-line treatments [5]. β-blockers used for AF treatment, typically metoprolol or carvedilol, block the β_1 receptors in the heart and as a result reduce the effect of the sympathetic nervous system, thus reducing the heart rate. A stimulus of β_1 receptors increases the inward Ca^{2+} current through the L-type channels, hence blocking these receptors results in a prolongation of the action potential, as described in Section 2.1.1 [38]. The non-dihydropyridine calcium channel blockers, typically verapamil or diltiazem, reduce the heart rate by preventing the L-type calcium channels from opening, which reduces the conduction velocity in the SA and AV node cells. Moreover, combination therapy of β-blockers, calcium channel blockers, and digoxin are also used [39]. However, little robust evidence exists to inform the most efficient type and intensity of the rate control treatment [40]. Furthermore, ablation of the AV node and the implantation of a pacemaker is also an option, however usually only used as a last resort when drugs are ineffective [5].

3.3 Electrocardiography During Atrial Fibrillation

The diagnosis of AF is based on the ECG, thus it is understandable that the ECG of a person with AF has distinguishable features compared to an ECG of a person without. In a healthy heart, as described in Section 2.2, the SA node starts an action potential that propagates throughout the atria, leading to the atria contraction. This atrial depolarization is visible in the ECG as the P-wave. After the action potential has been conducted through the AV node, it propagates throughout the ventricles, leading to ventricle contraction. This depolarization is visible in the ECG as the QRS complex. The series of intervals between successive R waves in the ECG is denoted as the RR interval series. During the QRS complex, the repolarization of the atria also takes place, but is insignificantly noticeable on the curve. Lastly, the repolarization of the ventricles is visible in the ECG as the T wave.

There are three main features visible from the ECG that are used for detection and diagnosis of AF; RR interval irregularity, P-wave absence, and presence of atrial fibrillatory waves (f-waves), all visible in Figure 3.1 [28]. The rapid and irregular activity in the atria during AF results in rapid and irregular stimulus to the AV node, and in turn irregular RR intervals, as is shown in Figure 3.2a. In fact, several AF-detection algorithms are based solely on the irregularity of the RR intervals [41, 42], since it is more easily and robustly extracted from the ECG. Furthermore, the time series of intervals between consecutive heartbeats can also be extracted from the photoplethysmogram, often measured from a light source together with a photodetector by smartwatches. Since the time series of intervals between consecutive heartbeats is the same as the RR interval series, several AF-detection algorithms have in recent years been based on the photoplethysmogram [43, 44]. During sinus rhythm, the P-wave represents the depolarization in the atria. However, since the electrical activity in the atria during AF is rapid and irregular, there is no clear P-wave, but instead constant f-waves. Even though the presence of f-waves is in itself vital information for detecting AF, more detailed parameters of the f-wave can be used for a more detailed characterization of the atrial electrical activity. The dominant atrial frequency can be estimated from the f-wave via the dominant peak in the frequency spectrum, and the amplitude of the f-waves has been used in clinical studies [45]. A hidden Markov model has been used to track the dominant frequency of the f-waves from the ECG in a robust way [46]; which is used in paper I and paper II in this thesis. However, QRS removal is necessary before this is possible, since the f-waves have a far smaller amplitude than the QRS complex. This can be achieved with several different methods, such as average beat subtraction, adaptive filtering, or blind source separation [47, 48, 49]. The f-waves have also been extracted using a voting scheme on four different template subtraction algorithms [50].

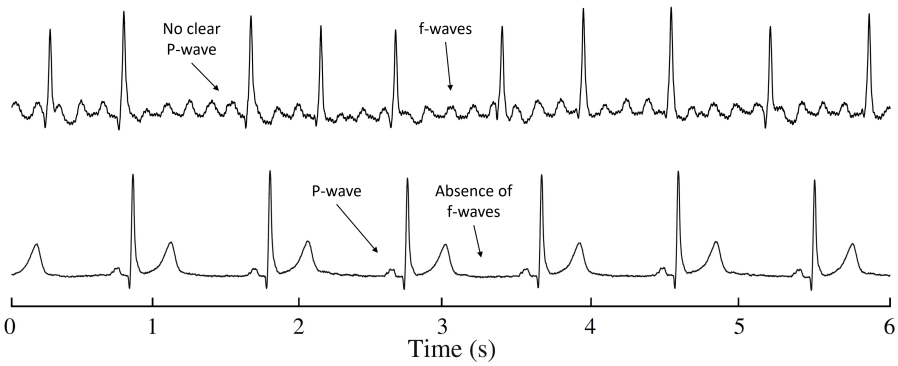

Figure 3.1: Difference between the ECG during AF (top) and normal sinus rhythm (bottom), where the three main differences; RR interval irregularity, P-wave absence, and presence of f-waves, are shown (reprinted from [28] with permission).

3.3.1 Representations of the RR interval series during atrial fibrillation

Since the RR interval series is a useful representation of the activity of the heart, especially during AF, it is useful to represent it explicitly. The RR interval series can be represented and visualized by a histogram. From Figure 3.2b, it is clear that the histogram of the RR interval series differs substantially between normal sinus rhythm and during AF; where the histogram during sinus rhythm has a more narrow RR interval histogram whereas the histogram during AF is much more scattered. In addition, using the number of data points in each bin, it is possible to compare data from different models or patients, which has previously been done to estimate AV node model parameters [51]. Another method of visualizing the RR interval series is by using the Poincaré plot, i.e., a scatter plot of successive pairs of the RR interval series. The Poincaré plot can be used to analyze nonlinear aspects of the heart rate, since it captures more dynamics in the series compared with the histograms [28]. For normal sinus rhythm, the Poincaré plot has one compact area where all points land, in contrast to the Poincaré plot during AF which is more spread out, as seen in Figure 3.2c. A fitness function (see Section 5.1.3) based on the Poincaré plot was used to estimate model parameters in paper I and paper II of this thesis. Other methods, such as autocorrelation, Shannon entropy, and root mean square of the successive differences, have also been used to characterize the RR interval series during AF [1, 52, 53].

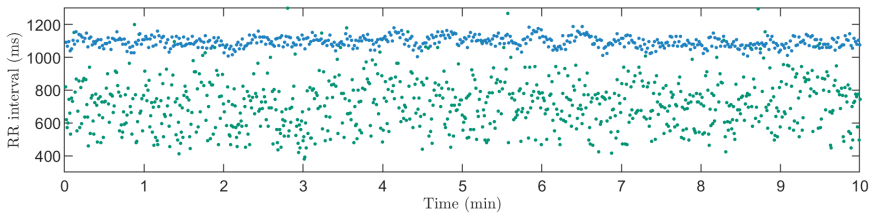

(a) RR interval series

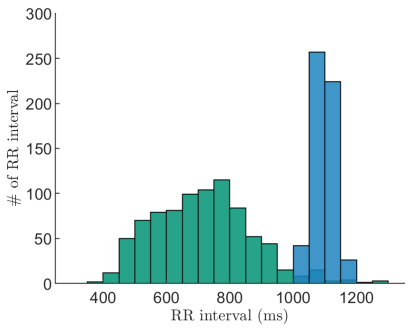

(b) Histogram of the RR interval series

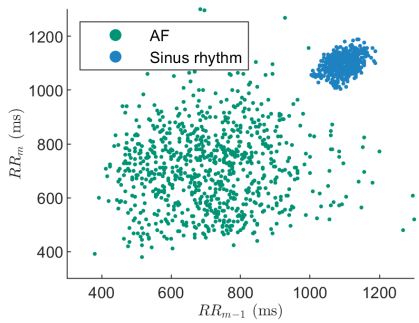

(c) Poincaré plot of the RR interval series

Figure 3.2: A comparison of the RR interval series (a), the histogram of the RR interval series (b), and the Poincaré plot of the RR interval series (c) during AF (green) and during normal sinus rhythm (blue). Data from the MIT-BIH Atrial Fibrillation Database [54].

Chapter 4
Cardiac Modeling

There have been multiple mathematical models of the human heart over the years, ranging from models describing the whole heart to models of specialized components such as the AV node. Some models are created in order to gain a deeper understanding of the heart, whiles others are designed to find interpersonal differences between patients for personalized treatment selection. Since the focus of this thesis is on electrophysiology models of the heart, only those models will be further considered.

This chapter will start with an overview of the field of cardiac electrophysiology modeling, in Section 4.1, before narrowing in on models of the AV node, in Section 4.2. Different types of AV node models will be presented, before ending the chapter with a detailed description of the specific model designed for assessing the conduction delay and refractory period of the AV node during AF proposed in Paper I.

4.1 Cardiac Electrophysiology Models

The electrophysiology of the heart can and has been modeled in numerous ways, depending on the purpose of the model. For the electrophysiology, the action potential is of interest. As described in Section 2.1.1, the action potential in cardiac cells is largely dependent on the Na^+, K^+, and Ca^{2+} channels, and thus several models of these ion channels are combined to model the action potential. These ionic currents are often modeled using Markov models, where the Hodgkin-Huxley current model can be seen as a subclass [55]. The Hodgkin-Huxley models [56] are dynamic descriptions of voltage-dependent ion channel gating in a membrane, and are often combined to create action potential models. The complexity of the action potential models has evolved over the years. Comparing the first model of the action potential in the heart which uses three ion channel sub-models [57] to more recent models [58, 59], the

number of ion channel sub-models has had a tenfold increase.

These larger models result in a large number of model parameters, increasing the difficulty of interpreting and understanding the relationship between model parameters and model output. Thus, the purpose of the model is important, and model reductions as well as more simplistic models are of interest. Model reduction is based on the idea that some model parameters are redundant – often found through sensitivity analysis – and used to create 'reduced' versions of complex models [60]. More simplistic models, often designed for a minimal phenomenological representation, such as a simplified geometry, have also been created for the same reasons [61, 62].

4.2 AV Node Models

Several models of the AV node have been created in recent years, with different levels of complexity for different intents. A number of AV node models relevant to this thesis are summarized here; starting with three designed mainly to widen the understanding of the AV node, before describing two designed mainly for individual assessment of the AV node properties.

A unified model describing ventricular pacing, conduction delays, and refractoriness for the AV node during AF has been proposed by Lian et al. presented in [63]. This model is divided into four interconnected components. The first component is an AF generator, which generates the incoming impulses to the AV node via a Poisson process. A Poisson process is commonly used to create incoming impulses into the AV node, and it is a stochastic process with one parameter, often named λ, representing the mean arrival rate. The second component describes the AV junction, including the AV node, as a lumped structure characterized by several electrical properties such as the refractory period and conduction delay. The dynamics of the AV junction recovery and delay are described using an exponential recurrence relation. The third component models the ventricles which can affect the AV junction through retrograde waves. The fourth and final component in the model is an electrode capable of regulating pacing. All four components are connected to be capable of affecting each other. The model has been used to investigate the impact of conduction properties and AF rate on the ventricular rate as well as the electrotonic modulation in the AV junction. It is capable of simulating RR series similar to observed RR series during AF. However, due to the lumped structure of the AV junction, the model lacks spatial resolution in the AV node and dual pathway physiology.

The AV node model proposed by Climent et al. in [64] describes the conduction delay of the AV node for the FP and the SP. The conduction delay for both pathways is modeled as an exponential function, and the parameters describing the exponential functions were determined using data from in vitro pacing on rabbit hearts. For validating the model during AF, irregularly distributed AA intervals were used as input to both model and the in vitro rabbit hearts. The model incorporates concealed conduction, i.e., a stimulation inside the AV node that does not activate the ventricles but leads to a change in conduction characteristics, by calculating the conduction delay of the two pathways. The pathway with lower conduction delay retrogradely invades the other, causing a concealed conduction. The concealed conduction affects the coming impulse by a modification of the parameter values of the exponential function of the pathway with a higher conduction delay. This model improved the knowledge of the complex and poorly understood characteristics of the conduction time and dual pathways of the AV node during arrhythmias such as AF by, for example, simulating ablation of both pathways.

A biophysically detailed action potential model of the SA node, right atrium, and AV node, describing and analyzing the functions of the conduction system, has been proposed by Inada et al. in [65]. The model describes the rabbit heart as a one-dimensional multicellular network of cell models. The model characterizes the AV node in terms of three different AV node cell models describing different regions of the AV node; the region of atrio-nodal cells representing the start of the AV node, the region of nodal cells representing the middle of the AV node, and the region of nodal-His cells representing the end of the AV node. All the cells for each region are based on action potential recordings of rabbit hearts and are made up of the different ion currents inside a cell. Each of these cells uses a nonlinear dynamic system of 26 simultaneous ordinary differential equations to describe action potential dynamics. The SP is modeled by 200 cell models and the FP by 150, creating the standard dual pathway structure of the AV node. To simulate AF in the model, stimuli with random intervals were introduced into the string of atrial cells before the AV node. The model incorporates the typical physiological characteristics of the AV node tissue and has been used to analyze the rich behavior of the AV node such as the effect of Ca^{2+} channel blocking and AV node pacemaking.

A statistical model of the AV node has been proposed by Corino et al. in [66] with further development in [67, 68], and was specially designed for AF. The purpose of this model is to assess the electrophysiology properties of the AV node based solely on the ECG. It is a lumped model structure that still accounts for concealed conduction, relative refractoriness, and dual pathways. Incoming impulses from the atria are generated to the AV node following a Poisson process and each impulse into the model

either results in a ventricular activation or is blocked due to the AV node being in its refractory phase. The length of the refractory period is made up of a deterministic and a stochastic part. The deterministic part is split into two parts, representing the two pathways of the AV node. Moreover, the stochastic part is assumed to be uniformly distributed. The mean arrival rate used for simulating atrial activation to the AV node is estimated from the atrial activity, which in turn is extracted from the ECG using spatiotemporal QRST cancellation [69]. The remaining model parameters are estimated by jointly maximizing the log-likelihood function. This model has been shown to replicate 88% of RR interval series, where the comparison was made between the probability density function of the model and an empirical probability density function. However, the interpretation of the model parameters can be problematic, since several characteristic features of the AV node are grouped together.

4.3 Network Model of the AV Node

The event-based phenomenological model I proposed in [1] following the work in [51] has separate parameters for the refractory period and the conduction delay, which in turn makes it easy to interpret. Similar to the previous model, the purpose is to assess the electrophysiology properties of the AV node based on ECG. The model describes the AV node as a network of 21 nodes, divided into the FP, the SP, and a coupling node, as shown in Figure 4.1. The nodes correspond to a localized section of the AV node, where each pathway is modeled with ten nodes. Each of these nodes either transmits an incoming impulse to all adjacent nodes, adding a conduction delay, or blocks the impulse completely. This block of the impulse will occur if the impulse arrives during a node's refractory phase. The refractory period and conduction delay for the pathway node i is updated for each incoming impulse n according to Equation 4.1, 4.2 and 4.3,

$$R_i(n) = R_{min} + \Delta R(1 - e^{-\tilde{t}_i(n)/\tau_R}) \tag{4.1}$$

$$D_i(n) = D_{min} + \Delta D e^{-\tilde{t}_i(n)/\tau_D} \tag{4.2}$$

$$\tilde{t}_i(n) = t_i(n) - t_i(n-1) - R_i(n-1), \tag{4.3}$$

where $t_i(n)$ is the arrival time of impulse n at node i and $\tilde{t}_i(n)$ the diastolic interval preceding impulse n. Negative time for $\tilde{t}_i(n)$ indicates that the node is in its refractory state and, as a consequence, the node will block incoming impulses. The refractory period and conduction delay in the pathways are thus defined by three parameters each; the minimum value R_{min} and D_{min}; the maximum prolongation ΔR and ΔD; and the time constants τ_R and τ_D. Each parameter is assumed to be

identical for the nodes in the SP and FP, respectively. Even though all nodes associated with the same pathway will have the same parameters, each node will still have its own value for the refractory and delay time due to the ever-changing arrival time of the impulses to each node. Moreover, the coupling node models the connection between the end of the AV node to the bundle of His, the bundle of His itself, and the Purkinje fibers. In contrast to the pathway nodes, the refractory period and conduction delay for the coupling node are set to constant values. The refractory period is set to the mean of the ten shortest RR intervals, and the conduction delay is set to 60 ms, based on clinical studies. The impulses to the model are created by a Poisson process with mean arrival rate λ estimated from the f-waves and are propagated throughout the network in an event-based fashion. The system is solved fast using a modified version of Dijkstra's algorithm [70]. By using an event-based model, several interesting properties besides the model parameters themself can be studied, such as the amount of concealed conduction, the ratio of impulses propagating through the different pathways, and the histogram and Poincaré plot of modeled RR interval series.

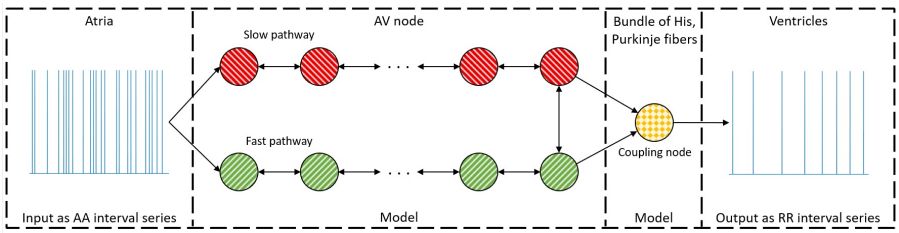

Figure 4.1: A schematic representation of the network model, divided into the slow pathway (red), fast pathway (green), and a coupling node (yellow). The input to the model is created using a Poisson process, representing atrial activation, and the output represents ventricular activation [1].

Chapter 5
Model Fitting and Parameter Estimation

With a mathematical model and data at hand, the next step is to estimate the model parameters. Estimation is often accomplished using the probabilistic approach, which assumes that the data can be described according to a probability distribution. Some of the more common estimators for this include maximum likelihood estimation and the maximum a posteriori estimator [71]. However, without a probabilistic interpretation, there is a need for other techniques.

Optimization is a general term for finding the optimum of some function in a parameter space. Hence, with a function describing how close the model output is to the data, parameter estimation can be achieved by optimization. Such a function is henceforth called a target function and its inverse an error function. Optimizing the parameters is synonymous with finding the maximum of the target function. A function can have several maxima, both global and local. A local maximum – the maximum value in a limited area – can be hard to distinguish from a global one. Given access to the analytical form of the function, it is possible to find a maximum by differentiating and solving for zero. However, in practice, this situation is rare, and thus other forms of optimization are needed.

In this chapter, the general differences between optimization strategies will first be presented in Section 5.1, together with a brief description of different optimization algorithms relevant to this thesis. Emphasis is put on the genetic algorithm and dynamic optimization, since paper I and paper II make use of the genetic algorithm, and paper II focuses on dynamic optimization. This chapter will then follow with the idea of using a mixed-effect model to estimate parameter trends, in Section 5.2, before concluding with a description of uncertainty estimation, in Section 5.3.

5.1 Optimization Algorithms

Optimization algorithms are here divided into two categories; iterative algorithms converging to a solution,[1] or heuristics algorithms which do not necessarily converge. The iterative methods can further be divided depending on if they are evaluating the Hessian, the gradient, or only function values. If the Hessians or gradients can be calculated, they are beneficial for improving the rate of convergence. If the Hessians or gradients cannot be calculated, numerical approximations are needed. The main drawback with this method is local maxima, since the gradient is zero regardless if it is a local or global maximum. In these cases, heuristic optimizers are often used. Although they are not guaranteed to converge to a maximum, heuristic optimizers can be very useful, for example for functions with noisy error surfaces where gradient or Hessian methods would struggle.

An additional component in optimization adding complexity is optimization in a dynamic environment, when the values of the target function, and thus the global optimum, vary over time. Hence, the problem is not only to find the global optimum, but to track it over time. Such a problem is named a dynamic optimization problem and is of interest since trends in model parameters give important insights into many real-world problems. The most common algorithms for dynamic optimization problems are the population-based heuristic optimizers, such as evolution or swarm intelligence based algorithms [72, 73]. For these algorithms, loss of diversity, i.e., how different parameter sets in the population are compared to each other, is one of the most critical challenges [74, 75]. There has therefore been a great number of methods created to address this, mostly based on replacing individuals in the populations in clever ways.

Given a target function, which often is problem-specific, there are several optimization algorithms to choose from. There are more optimization algorithms created than can be discussed here, or in any document, which is why only a number of approaches relevant to work on AV node models are presented and discussed here.

5.1.1 Gradient descent

Possibly the most commonly used approach, gradient descent is an iterative method where the gradient or approximate gradient is explicitly used to minimize the error function [76]. Each iteration evaluates the gradient of the error function to determine what direction the next step should be taken. The method is based on Equation 5.1

[1] Given a non-pathological function and a reasonable step size.

$$\boldsymbol{x}_{n+1} = \boldsymbol{x}_n - \boldsymbol{\gamma}\nabla F(\boldsymbol{x}_n), \tag{5.1}$$

where $\boldsymbol{x}_n$ is the current parameter vector, $\boldsymbol{x}_{n+1}$ is the next one, $\nabla F(\boldsymbol{x}_n)$ is the gradient at point $\boldsymbol{x}_n$, and $\boldsymbol{\gamma}$ is the step size. The simplicity and effectiveness of gradient descent make it useful when the gradient is known. However, it is prone to get stuck at local optima if such exists. Hence, the result might not be a global optimum and is thus highly affected by the choice of starting position. It can also be very sensitive to the choice of step size; where a too-small step size converges slowly and a too-large step size might prohibit the algorithm from converging to a local optima due to overshooting.

5.1.2 Particle swarm optimization

Particle swarm optimization is a heuristic optimization algorithm based on swarm intelligence inspired by the movement and social interaction in schools of fish and flocks of birds [77, 78]. Particle swarm optimization is made up of a swarm of particles, where each particle is the set of parameters that should be estimated. Particle swarm optimization has in recent years been used in a vast variety of fields, for example to optimize the optical efficiency of solar power towers [79] and to support decision-making in marine oil spill responses [80]. Either the search space or groups of particles in the algorithm can be divided into different subsets called topologies. Each particle searches by itself, with guidance and knowledge of the best-found solution in its topology. Each particle updates its position according to Equation 5.2,

$$\boldsymbol{v}_{n+1} = w_1\boldsymbol{v}_n + w_2\boldsymbol{r}_1(\boldsymbol{p} - \boldsymbol{x}_n) + w_3\boldsymbol{r}_2(\boldsymbol{g} - \boldsymbol{x}_n), \tag{5.2}$$

where $\boldsymbol{v}_n$ is the previous step, $\boldsymbol{p}$ is the best position the particle has previously found (evaluated on the target function), $\boldsymbol{g}$ is the best position found by any particle in the current topology, $\boldsymbol{r}_1$ and $\boldsymbol{r}_2$ are random vectors, w_1, w_2, w_3 are weighting factors, $\boldsymbol{v}_{n+1}$ is the step taken, and $\boldsymbol{x}_n$ is the current parameter set. Hence, the next position for the parameter vector, $\boldsymbol{x}_{n+1}$, is calculated as

$$\boldsymbol{x}_{n+1} = \boldsymbol{x}_n + \boldsymbol{v}_{n+1}. \tag{5.3}$$

As with all heuristic optimizers, one drawback is that it is not guaranteed to find a maximum. However, the broadness of the search makes it less likely to get stuck in local optima compared to the gradient descent and the genetic algorithm. The nature

of the algorithm makes it very suitable for use on dynamic optimization problems, since the particles will move around the error surface when the surface is changing, gradually improving on previously found solutions for slowly changing error surfaces.

5.1.3 Genetic algorithm

The genetic algorithm is a heuristic optimization algorithm based on biological evolution inspired by Darwin's concept of natural selection, with elements of mutation, crossover, and selection [81, 82]. A genetic algorithm is made up of a population of individuals, where each individual is the set of parameters that should be estimated, here denoted $\boldsymbol{x}_{n,i}$ with n denoting the generation and i the specific individual in the population. The population of individuals is first generated randomly before every individual is evaluated by a target function, in this context called a fitness function. The next generation of individuals is then created through a combination of selection, crossover, and mutation. Selection imitates natural selection and is used to choose two 'parents' from the population. Selection is most often performed by tournament selection or roulette wheel selection. In tournament selection, several individuals are randomly chosen and the fittest individual based on the fitness scores is selected with a certain probability. For selection by the roulette wheel, each individual has a probability of selection based on their fitness score, thus fitter individuals have a larger part of the wheel. Moreover, crossover is a concept mimicking breeding in nature and combines the genetic information from two parents to generate a new individual for the next generation. Mutation, on the other hand, introduces a random alteration in an individual.

An example of selection, crossover, and mutation is shown in Figure 5.1, where the two individuals $\boldsymbol{x}_{n,i}$ and $\boldsymbol{x}_{n,j}$ are first selected with a probability based on their fitness value. Two points between 1 and the number of parameters in the individuals are then randomly generated, as shown as c_1 and c_2 in Figure 5.1a, and the parameter values from the two parents are switched to create two offsprings, $\boldsymbol{x}_{n+1,i}$ and $\boldsymbol{x}_{n+1,j}$. Each parameter value for these two offsprings has a probability of being mutated, as shown in Figure 5.1b. New individuals are created in this fashion until there are as many individuals in generation $n + 1$ as in the previous generation. This process of creating new generations is further continued until a termination criterion is met, which can be that an individual with a fitness value above a predefined threshold is found, that a fixed number of generations or time has passed, or that the best solution does not change between generations. Genetic algorithms have been used to find solutions to complex problems such as designing a specialized antenna [83] or predicting the inflation rate [84], and can be very useful when no gradient or Hessian can be calculated, or when noise renders them unusable. One main drawback of this

method is the randomness it introduces, thus the results can vary from estimation to estimation. Moreover, it is also a heuristic algorithm, thus it is not guaranteed to find a maximum. The nature of the genetic algorithm makes it very suitable for use on dynamic optimization problems, since the fitness of the individuals will change over time, similar to how a change in climate causes real-world animals to evolve.

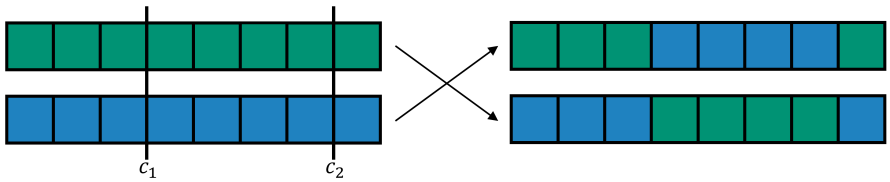

(a) Two point crossover

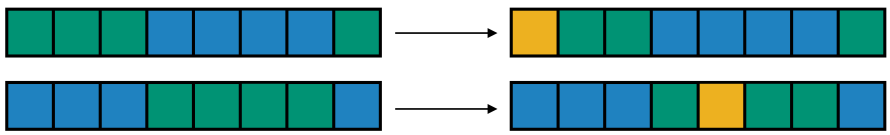

(b) Mutation

Figure 5.1: A schematic representation of crossover in a genetic algorithm between two parents (left) to their children (right) can be seen in (a). Following, a mutation of these children can be seen in (b). For this illustration, the value for the eight parameters (squares) is represented by colors.

5.2 Mixed-effect Modeling

Dynamic optimization often results in parameter estimation trends, a time series of the model parameters. It can thus be useful to analyze the trends by fitting them to a model describing the parameters over time. When different patients and drugs are included, as often is the case studying biomedical data, the mixed-effects model structure – containing both fixed effects and random effects – is of interest [85]. Using a mixed-effect model, the fixed effect can describe the overall effect of a drug on a population, whereas the random effects describe each patient's individual response. A linear mixed-effect model can be represented by Equation 5.4,

$$\boldsymbol{y} = \boldsymbol{X}\boldsymbol{\beta} + \boldsymbol{Z}\boldsymbol{u} + \boldsymbol{\epsilon}, \tag{5.4}$$

where $\boldsymbol{y}$ is the known vector of observations, $\boldsymbol{\beta}$ the unknown vector of fixed effects, $\boldsymbol{u}$ the unknown vector of random effects, $\boldsymbol{\epsilon}$ the unknown vector of random errors,

and $\boldsymbol{X}$ and $\boldsymbol{Z}$ are the known design matrices relating the observations to the fixed and random effects, respectively. In paper II, a simple linear mixed-effect model was used to estimate the circadian variation in the parameter trends based on a sinusoid with three parameters; a mean, an amplitude, and a phase shift.

5.3 Uncertainty Estimation

An important aspect when estimating model parameters is their uncertainty. Without a proper measure of the uncertainty, it is not possible to determine the quality of the estimates and thus their usability. Uncertainty in this sense includes both the uncertainty in the estimator and in the resulting parameter's effect on the model. A straightforward approach to understanding the estimator uncertainty when using a heuristics optimizer is to run the optimizer several times, and compare the spread of the resulting parameters, which was done in paper I. The uncertainty estimation using this approach will depend on the specific parameter values, and is thus not necessarily equal for all possible parameter values. To understand the parameter's effect on the model, a sensitivity analysis is often used. The simplest and most common type of sensitivity analysis is the one-at-a-time approach, where only one parameter is perturbed at a time, keeping all others at a constant value [86]. The drawback of this technique is its inability to take information about covariance between parameters into account. An alternative is to use variance-based sensitivity analysis, often referred to as Sobol's method, which is a global sensitivity analysis [87]. Using Sobol's method, it is possible to derive the so-called 'total-effect' index measuring the contribution to the output variance for each parameter including the variance caused by interactions with all other parameters. For analytically tractable functions, the total-effect index can be analytically evaluated. However, for non-analytically tractable functions or models, it can be estimated using a Monte Carlo method [88]. A version of Sobol's method was used to estimate the parameter uncertainty in paper II, where the sensitivity analysis was computed in a limited area around the optimum parameter set.

Chapter 6
Summary of Papers

The two papers included in this thesis are together addressing the three aims stated in Section 1.2. The first aim – to create a mathematical model of the AV node during AF capable of detailed physiological insights on an individual level – is addressed in paper I. The second aim – to estimate model parameters in a robust and computationally efficient way using non-invasive data – is addressed in paper I and paper II. In paper I, the parameters are estimated using 20 min long RR interval series. In paper II, the parameter trends during 24 hours are instead estimated. The last aim – to apply the model and estimation method to patient data at baseline and under the influence of different types of drugs to analyze drug-dependent differences in the circadian variation in the AV node properties – is addressed in paper II, where differences in conduction delay could be seen between different drug types.

6.1 Paper I: Non-invasive Characterization of Human AV-Nodal Conduction Delay and Refractory Period During Atrial Fibrillation

In the paper entitled 'Non-invasive Characterization of Human AV-Nodal Conduction Delay and Refractory Period During Atrial Fibrillation' we propose the network model described in Section 4.3. This model is based on the work in [51], here named the reference model, where the coupling node in the network is changed from belonging to the slow pathway to its own type of node. The refractory period for the coupling node is changed to no longer depend on the diastolic interval, and the conduction delay is fixed. Together with the proposed model, we also presented an associated workflow comprised of a problem-specific fitness function based on the Poincaré plot, which utilizes the dynamics in the RR interval series, together with a problem-

specific genetic algorithm.

In contrast to the reference model presented in [51], the proposed model in paper I is able to replicate the dynamics in the RR interval series extracted from the ECG, as visualized by the Poincaré plot and autocorrelation in Figure 6.1. Furthermore, the problem-specific genetic algorithm enabled estimation of the conduction delay and refractory period in the AV node non-invasively in a robust way, and was evaluated using both ECG and simulated data. The results implied that drug-dependent differences in the AV node conduction properties could be assessed using this model.

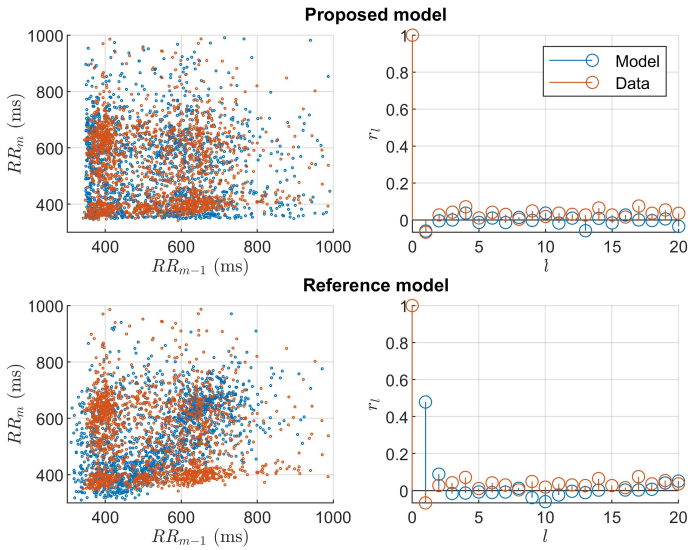

Figure 6.1: A comparison of the Poincaré plot (left) and autocorrelation (right) between the proposed model and workflow in paper I (top), and the reference model and workflow in [51] (bottom).

6.2 Paper II: ECG Based Assessment of Circadian Variation in AV-nodal Conduction During AF - Influence of Rate Control Drugs

The paper entitled 'ECG Based Assessment of Circadian Variation in AV-nodal Conduction During AF - Influence of Rate Control Drugs' uses the model presented in paper I to study long-term variations in the conduction delay and refractory period. In order to obtain a long-term assessment of these properties, a problem-specific genetic algorithm designed for dynamic optimization problems was designed. The hyper-parameters in the genetic algorithm were tuned during the optimization, based on changes in the RR interval series characteristics. This enabled the genetic algorithm to quickly search for different promising regions whenever the RR interval characteristics changed rapidly, while at the same time being able to search for the optimal solutions within an already promising region when the characteristics changed slowly.

The model and workflow were used to fit the refractory period and conduction delay of the AV node during 24 hours from ambulatory ECGs from 59 patients acquired during baseline and under the influence of four rate control drugs; two calcium channel blockers and two β-blockers.

From the estimated model parameter trends, a mixed-effect model was used to quantify the drug-dependent mean (α_m) and circadian variation (β_m). This analysis revealed drug-dependent differences in the conduction properties, as shown in Figure 6.2. The difference is most notable for the maximum prolongation of the conduction delay (ΔD^{FP} and ΔD^{SP}), where the β-blockers reduced the circadian variation more compared to the calcium channel blockers.

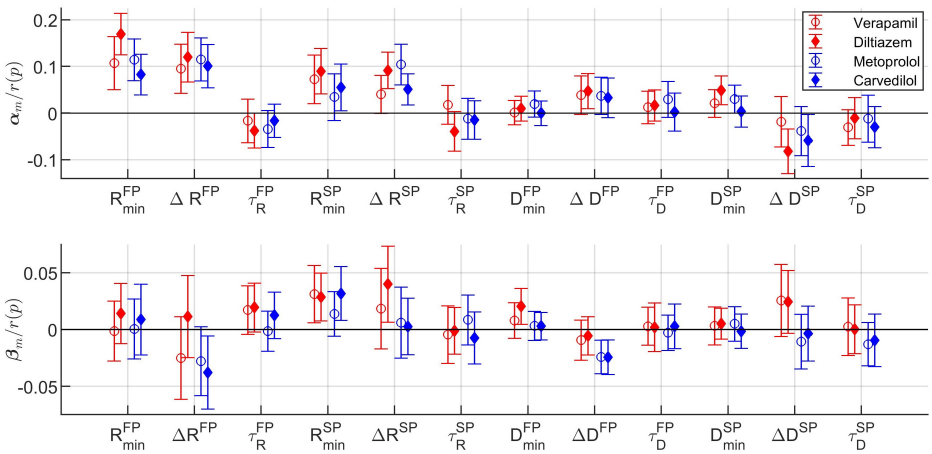

Figure 6.2: The fixed effect deviation from baseline for the linear mixed-effect model with corresponding 95% confidence intervals for the cosinor mean (top) and cosinor amplitude (bottom) for each of the twelve model parameters and four drugs. The confidence intervals not overlapping zero indicate a significant difference from baseline ($p < 0.05$).

Chapter 7
Outlook and Conclusion

In this thesis, a method for long-term assessment of the AV node conduction properties has been developed and evaluated in detail. The method consists of a mathematical model with associated parameter estimation in form of a problem-specific genetic algorithm. This method has enabled the analysis of drug-dependent differences in circadian variation of AV node conduction properties, which showed drug-dependent differences in the circadian variation for the conduction delay between β-blockers and calcium channel blockers.

As of now, the assessment of the refractory period and the conduction delay of the AV node is comprised in the twelve model parameters. From the model parameters, the exponential function determining the conduction properties for each pathway, shown in Equations 4.1 and 4.2, are known. However, these are a function of the diastolic interval. As a consequence, the refractory period or conduction delay at a given time for each pathway is not explicitly known from the model parameters. Thus, model reduction or combining the model parameters into four combined parameters, one for each conduction property in the respective pathway, would increase the interpretation of the model output.

The parameters of the network model of the AV node interact to a high degree, resulting in a high uncertainty in the model parameter estimation; since a minor change in one parameter could be counteracted by a minor change in a related parameter. This is especially important for the parameters relating to the minimum value and the maximum prolongation. Thus, high-frequency variation in the estimated model parameters shown in paper II could potentially be counteracted by a combination of parameters or a model reduction.

With access to Holter ECG for patients suffering from persistent AF during baseline and with different rate control drugs, an interesting question is prediction. Is it possible to use the estimated parameter trends during baseline together with basic information such as age or sex to predict the outcome with the different rate control drugs? The results from paper II, where the different drug types had different effects on the parameters, suggest that it is. Hence, investigating the patient-specific temporal patterns in the conduction properties of the AV node could potentially aid in therapeutic choices.

In conclusion, we can now non-invasively assess the temporal patterns in the conduction delay and the refractory period in the AV node during 24 hours, which have the potential to in an objective way assist in treatment selection for AF.

References

[1] M. Karlsson, F. Sandberg, S. R. Ulimoen, and M. Wallman, "Non-invasive characterization of human AV-nodal conduction delay and refractory period during atrial fibrillation," *Frontiers in physiology*, p. 1849, 2021.

[2] M. Karlsson, M. Wallman, P. G. Platonov, S. R. Ulimoen, and F. Sandberg, "ECG based assessment of circadian variation in AV-nodal conduction during AF—influence of rate control drugs," *Frontiers in physiology*, p. 2015, 2022.

[3] M. Karlsson, M. Wallman, S. R. Ulimoen, and F. Sandberg, "Non-invasive characterization of atrio-ventricular properties during atrial fibrillation," in *2021 Computing in Cardiology (CinC)*, vol. 48, pp. 1–4, IEEE, 2021.

[4] M. Karlsson, M. Wallman, P. G. Platonov, S. R. Ulimoen, and F. Sandberg, "Drug dependent circadian variations in AV-nodal properties during atrial fibrillation," *2022 Computing in Cardiology (CinC)*, 2022 (in press).

[5] G. Hindricks, T. Potpara, N. Dagres, E. Arbelo, J. J. Bax, C. Blomström-Lundqvist, G. Boriani, M. Castella, G.-A. Dan, P. E. Dilaveris, *et al.*, "2020 ESC guidelines for the diagnosis and management of atrial fibrillation developed in collaboration with the european association for cardio-thoracic surgery (EACTS) the task force for the diagnosis and management of atrial fibrillation of the european society of cardiology (ESC) developed with the special contribution of the european heart rhythm association (EHRA) of the ESC," *European heart journal*, vol. 42, no. 5, pp. 373–498, 2021.

[6] E. J. Benjamin, P. A. Wolf, R. B. D'Agostino, H. Silbershatz, W. B. Kannel, and D. Levy, "Impact of atrial fibrillation on the risk of death: the framingham heart study," *Circulation*, vol. 98, no. 10, pp. 946–952, 1998.

[7] N. E. Andrew, A. G. Thrift, and D. A. Cadilhac, "The prevalence, impact and economic implications of atrial fibrillation in stroke: what progress has been made?," *Neuroepidemiology*, vol. 40, no. 4, pp. 227–239, 2013.

[8] S. R. Ulimoen, S. Enger, J. Carlson, P. G. Platonov, A. H. Pripp, M. Abdelnoor, H. Arnesen, K. Gjesdal, and A. Tveit, "Comparison of four single-drug regimens on ventricular rate and arrhythmia-related symptoms in patients with permanent atrial fibrillation," *The American journal of cardiology*, vol. 111, no. 2, pp. 225–230, 2013.

[9] A. Di Carlo, L. Bellino, D. Consoli, F. Mori, A. Zaninelli, M. Baldereschi, A. Cattarinussi, M. G. D'Alfonso, C. Gradia, B. Sgherzi, *et al.*, "Prevalence of atrial fibrillation in the italian elderly population and projections from 2020 to 2060 for italy and the european union: the fai project," *EP Europace*, vol. 21, no. 10, pp. 1468–1475, 2019.

[10] Z. Jiang, M. Pajic, S. Moarref, R. Alur, and R. Mangharam, "Modeling and verification of a dual chamber implantable pacemaker," in *International Conference on Tools and Algorithms for the Construction and Analysis of Systems*, pp. 188–203, Springer, 2012.

[11] J. E. Hall, *Guyton and Hall textbook of medical physiology e-Book*. Elsevier Health Sciences, 2010.

[12] H.-T. Shih, "Anatomy of the action potential in the heart.," *Texas Heart Institute Journal*, vol. 21, no. 1, p. 30, 1994.

[13] T. N. James, "The internodal pathways of the human heart," *Progress in cardiovascular diseases*, vol. 43, no. 6, pp. 495–535, 2001.

[14] G. J. Tortora and B. H. Derrickson, *Introduction to the human body*. John Wiley & Sons, 2017.

[15] O. Monfredi, H. Dobrzynski, T. Mondal, M. R. Boyett, and G. M. Morris, "The anatomy and physiology of the sinoatrial node — a contemporary review," *Pacing and clinical electrophysiology*, vol. 33, no. 11, pp. 1392–1406, 2010.

[16] F. L. Meijler and M. J. Janse, "Morphology and electrophysiology of the mammalian atrioventricular node," *Physiological reviews*, vol. 68, no. 2, pp. 608–647, 1988.

[17] S. A. George, N. R. Faye, A. Murillo-Berlioz, K. B. Lee, G. D. Trachiotis, and I. R. Efimov, "At the atrioventricular crossroads: dual pathway electrophysiology

in the atrioventricular node and its underlying heterogeneities," *Arrhythmia & electrophysiology review*, vol. 6, no. 4, p. 179, 2017.

[18] G. K. Moe, J. B. Preston, and H. Burlington, "Physiologic evidence for a dual AV transmission system," *Circulation Research*, vol. 4, no. 4, pp. 357–375, 1956.

[19] T. Kurian, C. Ambrosi, W. Hucker, V. V. Fedorov, and I. R. Efimov, "Anatomy and electrophysiology of the human AV node," *Pacing and clinical electrophysiology*, vol. 33, no. 6, pp. 754–762, 2010.

[20] T. Nikolaidou, O. Aslanidi, H. Zhang, and I. Efimov, "Structure–function relationship in the sinus and atrioventricular nodes," *Pediatric cardiology*, vol. 33, no. 6, pp. 890–899, 2012.

[21] V. V. Fedorov, C. M. Ambrosi, G. Kostecki, W. J. Hucker, A. V. Glukhov, J. P. Wuskell, L. M. Loew, N. Moazami, and I. R. Efimov, "Anatomic localization and autonomic modulation of atrioventricular junctional rhythm in failing human hearts," *Circulation: Arrhythmia and Electrophysiology*, vol. 4, no. 4, pp. 515–525, 2011.

[22] J. Billette, "Atrioventricular nodal activation during periodic premature stimulation of the atrium," *American Journal of Physiology-Heart and Circulatory Physiology*, vol. 252, no. 1, pp. H163–H177, 1987.

[23] A. P. DE Carvalho and D. F. De Almeida, "Spread of activity through the atrioventricular node," *Circulation research*, vol. 8, no. 4, pp. 801–809, 1960.

[24] S. Liu, S. B. Olsson, Y. Yang, E. Hertervig, O. Kongstad, and S. Yuan, "Concealed conduction and dual pathway physiology of the atrioventricular node," *Journal of cardiovascular electrophysiology*, vol. 15, no. 2, pp. 144–149, 2004.

[25] N. Voigt, J. Heijman, Q. Wang, D. Y. Chiang, N. Li, M. Karck, X. H. Wehrens, S. Nattel, and D. Dobrev, "Cellular and molecular mechanisms of atrial arrhythmogenesis in patients with paroxysmal atrial fibrillation," *Circulation*, vol. 129, no. 2, pp. 145–156, 2014.

[26] M. Haissaguerre, P. Jaïs, D. C. Shah, A. Takahashi, M. Hocini, G. Quiniou, S. Garrigue, A. Le Mouroux, P. Le Métayer, and J. Clémenty, "Spontaneous initiation of atrial fibrillation by ectopic beats originating in the pulmonary veins," *New England Journal of Medicine*, vol. 339, no. 10, pp. 659–666, 1998.

[27] P. Santangeli, E. S. Zado, M. D. Hutchinson, M. P. Riley, D. Lin, D. S. Frankel, G. E. Supple, F. C. Garcia, S. Dixit, D. J. Callans, *et al.*, "Prevalence and distribution of focal triggers in persistent and long-standing persistent atrial fibrillation," *Heart Rhythm*, vol. 13, no. 2, pp. 374–382, 2016.

[28] L. Sörnmo, A. Petrėnas, and V. Marozas, *Atrial fibrillation from an engineering perspective*. Springer, 2018.

[29] S. M. Narayan and J. Jalife, "Crosstalk proposal: Rotors have been demonstrated to drive human atrial fibrillation," *The Journal of physiology*, vol. 592, no. pt 15, p. 3163, 2014.

[30] M. Allessie and N. de Groot, "Crosstalk opposing view: Rotors have not been demonstrated to be the drivers of atrial fibrillation," *The Journal of physiology*, vol. 592, no. pt 15, p. 3167, 2014.

[31] R. T. Carrick, B. E. Benson, O. R. Bates, and P. S. Spector, "Competitive drivers of atrial fibrillation: The interplay between focal drivers and multiwavelet reentry," *Frontiers in Physiology*, vol. 12, p. 633643, 2021.

[32] A. Shiroshita-Takeshita, B. J. Brundel, and S. Nattel, "Atrial fibrillation: basic mechanisms, remodeling and triggers," *Journal of Interventional Cardiac Electrophysiology*, vol. 13, no. 3, pp. 181–193, 2005.

[33] M. C. Wijffels, C. J. Kirchhof, R. Dorland, and M. A. Allessie, "Atrial fibrillation begets atrial fibrillation: a study in awake chronically instrumented goats," *Circulation*, vol. 92, no. 7, pp. 1954–1968, 1995.

[34] G. C. Markey, N. Salter, and J. Ryan, "Intravenous flecainide for emergency department management of acute atrial fibrillation," *The Journal of Emergency Medicine*, vol. 54, no. 3, pp. 320–327, 2018.

[35] A. J. Camm, A. Capucci, S. H. Hohnloser, C. Torp-Pedersen, I. C. Van Gelder, B. Mangal, G. Beatch, and A. Investigators, "A randomized active-controlled study comparing the efficacy and safety of vernakalant to amiodarone in recent-onset atrial fibrillation," *Journal of the American College of Cardiology*, vol. 57, no. 3, pp. 313–321, 2011.

[36] F. J. Martínez-Marcos, J. L. García-Garmendia, A. Ortega-Carpio, J. M. Fernández-Gómez, J. M. Santos, and C. Camacho, "Comparison of intravenous flecainide, propafenone, and amiodarone for conversion of acute atrial fibrillation to sinus rhythm," *The American journal of cardiology*, vol. 86, no. 9, pp. 950–953, 2000.

[37] L. Mont, F. Bisbal, A. Hernandez-Madrid, N. Perez-Castellano, X. Viñolas, A. Arenal, F. Arribas, I. Fernández-Lozano, A. Bodegas, A. Cobos, *et al.*, "Catheter ablation vs. antiarrhythmic drug treatment of persistent atrial fibrillation: a multicentre, randomized, controlled trial (SARA study)," *European heart journal*, vol. 35, no. 8, pp. 501–507, 2014.

[38] P. Dorian, "Antiarrhythmic action of β-blockers: Potential mechanisms," *Journal of cardiovascular pharmacology and therapeutics*, vol. 10, no. 4_suppl, pp. S15–S22, 2005.

[39] I. C. Van Gelder, M. Rienstra, H. J. Crijns, and B. Olshansky, "Rate control in atrial fibrillation," *The Lancet*, vol. 388, no. 10046, pp. 818–828, 2016.

[40] S. M. Al-Khatib, N. M. Allen LaPointe, R. Chatterjee, M. J. Crowley, M. E. Dupre, D. F. Kong, R. D. Lopes, T. J. Povsic, S. S. Raju, B. Shah, *et al.*, "Rate- and rhythm-control therapies in patients with atrial fibrillation: a systematic review," *Annals of internal medicine*, vol. 160, no. 11, pp. 760–773, 2014.

[41] J. Park, S. Lee, and M. Jeon, "Atrial fibrillation detection by heart rate variability in poincare plot," *Biomedical engineering online*, vol. 8, no. 1, pp. 1–12, 2009.

[42] J. Lee, Y. Nam, D. D. McManus, and K. H. Chon, "Time-varying coherence function for atrial fibrillation detection," *IEEE Transactions on Biomedical Engineering*, vol. 60, no. 10, pp. 2783–2793, 2013.

[43] G. H. Tison, J. M. Sanchez, B. Ballinger, A. Singh, J. E. Olgin, M. J. Pletcher, E. Vittinghoff, E. S. Lee, S. M. Fan, R. A. Gladstone, *et al.*, "Passive detection of atrial fibrillation using a commercially available smartwatch," *JAMA cardiology*, vol. 3, no. 5, pp. 409–416, 2018.

[44] S. Kwon, J. Hong, E.-K. Choi, E. Lee, D. E. Hostallero, W. J. Kang, B. Lee, E.-R. Jeong, B.-K. Koo, S. Oh, *et al.*, "Deep learning approaches to detect atrial fibrillation using photoplethysmographic signals: algorithms development study," *JMIR mHealth and uHealth*, vol. 7, no. 6, p. e12770, 2019.

[45] M. Henriksson, *Modelling and Quality Assessment of Atrial Fibrillatory Waves*. PhD thesis, Lund University, 2019.

[46] F. Sandberg, M. Stridh, and L. Sornmo, "Frequency tracking of atrial fibrillation using hidden markov models," *IEEE Transactions on Biomedical Engineering*, vol. 55, no. 2, pp. 502–511, 2008.

[47] J. Slocum, A. Sahakian, and S. Swiryn, "Diagnosis of atrial fibrillation from surface electrocardiograms based on computer-detected atrial activity," *Journal of electrocardiology*, vol. 25, no. 1, pp. 1–8, 1992.

[48] A. Petrenas, V. Marozas, L. Sornmo, and A. Lukosevicius, "An echo state neural network for QRST cancellation during atrial fibrillation," *IEEE transactions on biomedical engineering*, vol. 59, no. 10, pp. 2950–2957, 2012.

[49] V. Zarzoso and P. Comon, "Robust independent component analysis by iterative maximization of the kurtosis contrast with algebraic optimal step size," *IEEE Transactions on neural networks*, vol. 21, no. 2, pp. 248–261, 2009.

[50] S. Biton, M. Suleiman, N. B. Moshe, L. Sörnmo, and J. A. Behar, "Estimation of f-wave dominant frequency using a voting scheme," *arXiv preprint arXiv:2209.03762*, 2022.

[51] M. Wallman and F. Sandberg, "Characterisation of human AV-nodal properties using a network model," *Medical & biological engineering & computing*, vol. 56, no. 2, pp. 247–259, 2018.

[52] S. Dash, K. Chon, S. Lu, and E. Raeder, "Automatic real time detection of atrial fibrillation," *Annals of biomedical engineering*, vol. 37, no. 9, pp. 1701–1709, 2009.

[53] F. Plappert, M. Wallman, M. Abdollahpur, P. G. Platonov, S. Östenson, and F. Sandberg, "An atrioventricular node model incorporating autonomic tone," *Frontiers in Physiology*, vol. 13, 2022.

[54] G. Moody, "A new method for detecting atrial fibrillation using RR intervals," *Computers in Cardiology*, pp. 227–230, 1983.

[55] D. G. Whittaker, M. Clerx, C. L. Lei, D. J. Christini, and G. R. Mirams, "Calibration of ionic and cellular cardiac electrophysiology models," *Wiley Interdisciplinary Reviews: Systems Biology and Medicine*, vol. 12, no. 4, p. e1482, 2020.

[56] A. L. Hodgkin and A. F. Huxley, "A quantitative description of membrane current and its application to conduction and excitation in nerve," *The Journal of physiology*, vol. 117, no. 4, p. 500, 1952.

[57] D. Noble, "A modification of the hodgkin—huxley equations applicable to purkinje fibre action and pacemaker potentials," *The Journal of physiology*, vol. 160, no. 2, p. 317, 1962.

[58] K. F. Decker, J. Heijman, J. R. Silva, T. J. Hund, and Y. Rudy, "Properties and ionic mechanisms of action potential adaptation, restitution, and accommodation in canine epicardium," *American Journal of Physiology-Heart and Circulatory Physiology*, vol. 296, no. 4, pp. H1017–H1026, 2009.

[59] J. Tomek, A. Bueno-Orovio, E. Passini, X. Zhou, A. Minchole, O. Britton, C. Bartolucci, S. Severi, A. Shrier, L. Virag, *et al.*, "Development, calibration, and validation of a novel human ventricular myocyte model in health, disease, and drug block," *Elife*, vol. 8, 2019.

[60] M. A. Herrera-Valdez and J. Lega, "Reduced models for the pacemaker dynamics of cardiac cells," *Journal of theoretical biology*, vol. 270, no. 1, pp. 164–176, 2011.

[61] P. Podziemski and J. J. Żebrowski, "A simple model of the right atrium of the human heart with the sinoatrial and atrioventricular nodes included," *Journal of clinical monitoring and computing*, vol. 27, no. 4, pp. 481–498, 2013.

[62] C. C. Mitchell and D. G. Schaeffer, "A two-current model for the dynamics of cardiac membrane," *Bulletin of mathematical biology*, vol. 65, no. 5, pp. 767–793, 2003.

[63] J. Lian, D. Mussig, and V. Lang, "Computer modeling of ventricular rhythm during atrial fibrillation and ventricular pacing," *IEEE transactions on biomedical engineering*, vol. 53, no. 8, pp. 1512–1520, 2006.

[64] A. M. Climent, M. S. Guillem, Y. Zhang, J. Millet, and T. Mazgalev, "Functional mathematical model of dual pathway AV nodal conduction," *American Journal of Physiology-Heart and Circulatory Physiology*, vol. 300, no. 4, pp. H1393–H1401, 2011.

[65] S. Inada, J. Hancox, H. Zhang, and M. Boyett, "One-dimensional mathematical model of the atrioventricular node including atrio-nodal, nodal, and nodal-his cells," *Biophysical journal*, vol. 97, no. 8, pp. 2117–2127, 2009.

[66] V. D. Corino, F. Sandberg, L. T. Mainardi, and L. Sornmo, "An atrioventricular node model for analysis of the ventricular response during atrial fibrillation," *IEEE transactions on biomedical engineering*, vol. 58, no. 12, pp. 3386–3395, 2011.

[67] V. D. Corino, F. Sandberg, F. Lombardi, L. T. Mainardi, and L. Sörnmo, "Atrioventricular nodal function during atrial fibrillation: Model building and robust

estimation," *Biomedical Signal Processing and Control*, vol. 8, no. 6, pp. 1017–1025, 2013.

[68] M. Henriksson, V. D. Corino, L. Sörnmo, and F. Sandberg, "A statistical atrioventricular node model accounting for pathway switching during atrial fibrillation," *IEEE Transactions on Biomedical Engineering*, vol. 63, no. 9, pp. 1842–1849, 2015.

[69] M. Stridh and L. Sornmo, "Spatiotemporal QRST cancellation techniques for analysis of atrial fibrillation," *IEEE Transactions on Biomedical Engineering*, vol. 48, no. 1, pp. 105–111, 2001.

[70] E. W. Dijkstra *et al.*, "A note on two problems in connexion with graphs," *Numerische mathematik*, vol. 1, no. 1, pp. 269–271, 1959.

[71] S. M. Kay, *Fundamentals of statistical signal processing*. Prentice Hall PTR, 1993.

[72] T. T. Nguyen, S. Yang, and J. Branke, "Evolutionary dynamic optimization: A survey of the state of the art," *Swarm and Evolutionary Computation*, vol. 6, pp. 1–24, 2012.

[73] M. Mavrovouniotis, C. Li, and S. Yang, "A survey of swarm intelligence for dynamic optimization: Algorithms and applications," *Swarm and Evolutionary Computation*, vol. 33, pp. 1–17, 2017.

[74] D. Yazdani, R. Cheng, D. Yazdani, J. Branke, Y. Jin, and X. Yao, "A survey of evolutionary continuous dynamic optimization over two decades — part A," *IEEE Transactions on Evolutionary Computation*, vol. 25, no. 4, pp. 609–629, 2021.

[75] D. Yazdani, R. Cheng, D. Yazdani, J. Branke, Y. Jin, and X. Yao, "A survey of evolutionary continuous dynamic optimization over two decades — part B," *IEEE Transactions on Evolutionary Computation*, vol. 25, no. 4, pp. 630–650, 2021.

[76] S. Ruder, "An overview of gradient descent optimization algorithms," *arXiv preprint arXiv:1609.04747*, 2016.

[77] J. Kennedy and R. Eberhart, "Particle swarm optimization," in *Proceedings of ICNN'95-International Conference on Neural Networks*, vol. 4, pp. 1942–1948, IEEE, 1995.

[78] S. Sengupta, S. Basak, and R. A. Peters, "Particle swarm optimization: A survey of historical and recent developments with hybridization perspectives," *Machine Learning and Knowledge Extraction*, vol. 1, no. 1, pp. 157–191, 2018.

[79] O. Farges, J.-J. Bézian, and M. El Hafi, "Global optimization of solar power tower systems using a monte carlo algorithm: Application to a redesign of the PS10 solar thermal power plant," *Renewable Energy*, vol. 119, pp. 345–353, 2018.

[80] X. Ye, B. Chen, P. Li, L. Jing, and G. Zeng, "A simulation-based multi-agent particle swarm optimization approach for supporting dynamic decision making in marine oil spill responses," *Ocean & Coastal Management*, vol. 172, pp. 128–136, 2019.

[81] D. Whitley, "A genetic algorithm tutorial," *Statistics and computing*, vol. 4, no. 2, pp. 65–85, 1994.

[82] S. Katoch, S. S. Chauhan, and V. Kumar, "A review on genetic algorithm: past, present, and future," *Multimedia Tools and Applications*, vol. 80, no. 5, pp. 8091–8126, 2021.

[83] G. Hornby, A. Globus, D. Linden, and J. Lohn, "Automated antenna design with evolutionary algorithms," in *Space 2006*, p. 7242, 2006.

[84] F. Dharma, S. Shabrina, A. Noviana, M. Tahir, N. Hendrastuty, and W. Wahyono, "Prediction of indonesian inflation rate using regression model based on genetic algorithms," *Jurnal Online Informatika*, vol. 5, no. 1, pp. 45–52, 2020.

[85] L. B. Sheiner and T. H. Grasela, "An introduction to mixed effect modeling: concepts, definitions, and justification," *Journal of pharmacokinetics and biopharmaceutics*, vol. 19, no. 3, pp. S11–S24, 1991.

[86] E. Borgonovo and E. Plischke, "Sensitivity analysis: a review of recent advances," *European Journal of Operational Research*, vol. 248, no. 3, pp. 869–887, 2016.

[87] I. M. Sobol, "Sensitivity analysis for non-linear mathematical models," *Mathematical modelling and computational experiment*, vol. 1, pp. 407–414, 1993.

[88] I. M. Sobol, "Global sensitivity indices for nonlinear mathematical models and their monte carlo estimates," *Mathematics and computers in simulation*, vol. 55, no. 1-3, pp. 271–280, 2001.

Part II

Included Papers

Paper I

frontiers in Physiology

ORIGINAL RESEARCH
published: 28 October 2021
doi: 10.3389/fphys.2021.728955

Non-invasive Characterization of Human AV-Nodal Conduction Delay and Refractory Period During Atrial Fibrillation

Mattias Karlsson[1,2], *Frida Sandberg*[2]*, *Sara R. Ulimoen*[3] *and Mikael Wallman*[1]

[1] *Department of Systems and Data Analysis, Fraunhofer-Chalmers Centre, Gothenburg, Sweden,* [2] *Department of Biomedical Engineering, Lund University, Lund, Sweden,* [3] *Department of Medical Research, Vestre Viken Hospital Trust, Bærum Hospital, Drammen, Norway*

During atrial fibrillation (AF), the heart relies heavily on the atrio-ventricular (AV) node to regulate the heart rate. Thus, characterization of AV-nodal properties may provide valuable information for patient monitoring and prediction of rate control drug effects. In this work we present a network model consisting of the AV node, the bundle of His, and the Purkinje fibers, together with an associated workflow, for robust estimation of the model parameters from ECG. The model consists of two pathways, referred to as the slow and the fast pathway, interconnected at one end. Both pathways are composed of interacting nodes, with separate refractory periods and conduction delays determined by the stimulation history of each node. Together with this model, a fitness function based on the Poincaré plot accounting for dynamics in RR interval series and a problem specific genetic algorithm, are also presented. The robustness of the parameter estimates is evaluated using simulated data, based on clinical measurements from five AF patients. Results show that the proposed model and workflow could estimate the slow pathway parameters for the refractory period, R^{SP}_{min} and ΔR^{SP}, with an error (mean ± std) of 10.3 ± 22 and −12.6 ± 26 ms, respectively, and the parameters for the conduction delay, $D^{SP}_{min,tot}$ and ΔD^{SP}_{tot}, with an error of 7 ± 35 and 4 ± 36 ms. Corresponding results for the fast pathway were 31.7 ± 65, −0.3 ± 77, 17 ± 29, and 43 ± 109 ms. These results suggest that both conduction delay and refractory period can be robustly estimated from non-invasive data with the proposed methodology. Furthermore, as an application example, the methodology was used to analyze ECG data from one patient at baseline and during treatment with Diltiazem, illustrating its potential to assess the effect of rate control drugs.

Keywords: atrial fibrillation, atrioventricular node, rate control, mathematical modeling, genetic algorithm, ECG, cardiac electrophysiology

OPEN ACCESS

Edited by:
Axel Loewe, Karlsruhe Institute of Technology (KIT), Germany

Reviewed by:
Andreu M. Climent, Universitat Politècnica de València, Spain
Eugenio Ricci, University of Bologna, Italy

***Correspondence:**
Frida Sandberg
frida.sandberg@bme.lth.se

Specialty section:
This article was submitted to Cardiac Electrophysiology, a section of the journal Frontiers in Physiology

Received: *22 June 2021*
Accepted: *29 September 2021*
Published: *28 October 2021*

Citation:
Karlsson M, Sandberg F, Ulimoen SR and Wallman M (2021) Non-invasive Characterization of Human AV-Nodal Conduction Delay and Refractory Period During Atrial Fibrillation. Front. Physiol. 12:728955. doi: 10.3389/fphys.2021.728955

1. INTRODUCTION

Atrial fibrillation (AF) is the most widespread sustained cardiac arrhythmia with an estimated prevalence of 2–4% in the adult population (Benjamin et al., 2019). During AF, the electrical activity in the atria is highly disorganized, leading to a rapid and irregular ventricular rhythm. In order to reduce these effects, rate control drugs constitute one of the primary therapeutic options

(Hindricks et al., 2020). These drugs are not designed to terminate AF, but rather to lower the heart rate. They do this by modulating the conduction through the AV node, preventing some electrical signals emanating from the atria from being transmitted to the ventricles, thereby reducing the ventricular activation rate. Thus, rate control is often sufficient to improve AF-related symptoms (Hindricks et al., 2020). The choice of first-line rate control drugs can vary between beta-blockers and non-dihydropyridine calcium channel blockers, with digoxin as a second-line option (Hindricks et al., 2020). However, the current method of finding the best treatment for a given patient is largely based on trial and error (Hindricks et al., 2020). Thus, patient specific characterization of AV node properties would be beneficial to achieve optimal rate control.

Functionally, the AV node consists of two pathways, connected to each other before entering the bundle of His (Kurian et al., 2010). The two pathways are referred to as the slow pathway (SP) and the fast pathway (FP), where the FP conducts impulses faster than SP but has a longer refractory period. During sinus rhythm, the impulses are typically conducted through the FP due to its faster conduction rate. During AF, however, conduction may alternate between SP and FP as a result of the rapid arrival of atrial impulses. This, together with concealed conduction, i.e., impulses inside the AV node that do not lead to ventricular activation but still affect the conduction characteristics of following impulses, gives rise to the complex blocking and delay behavior the AV node has been shown to possess.

In order to understand this blocking and delay behavior, mathematical modeling has become an increasingly important tool. Several models of the AV node and its function during AF have previously been proposed, including various descriptions of the conduction delay (Jørgensen et al., 2002; Mangin et al., 2005; Climent et al., 2011) and the refractory period (Rashidi and Khodarahmi, 2005). A model for simulating the ventricular activation capable of replicating both conduction delay and refractory period during AF was proposed by Lian et al. (2006). Another model capable of replicating both conduction delay and refractory period, based on the action potential of the AV node cells and modeled by ordinary differential equations, was proposed by Inada et al. (2009).

However, none of these models were developed with the purpose of ECG based estimation of AV node parameters on a patient specific basis. The models presented in Rashidi and Khodarahmi (2005) and Lian et al. (2006) did not fit parameter values to data, the models presented in Climent et al. (2011) and Inada et al. (2009) were fitted to data from rabbits. The models presented in Jørgensen et al. (2002) and Mangin et al. (2005) were fitted to AF patients, but invasive data was required. To make a model useful in a clinical setting, it should ideally allow for fitting to non-invasive data such as surface electrocardiogram (ECG). A statistical model developed for estimation of AV node parameters from ECG data during AF was first presented in Corino et al. (2011). This model has later been updated and proven to replicate patient specific histograms of the time series between two successive R waves on the ECG (RR interval series) extracted from ECG data, as well as to assess the effect of rate control drugs on the AV node (Henriksson et al., 2015). It is a lumped model structure that still accounts for concealed conduction, relative refractoriness, and dual pathways. However, it lumps conduction delay and refractory period together, making the estimated model parameters difficult to interpret.

In this work we present a network model of the AV node, able to estimate patient specific conduction delay and refractory period from ECG, building on previous work presented in Wallman and Sandberg (2018). The model consists of interconnected nodes forming two pathways, providing a balance between complexity and computational efficiency, and represents both spatial and temporal dynamics of the AV-node. With novel additions to the model structure by including effects from the bundle of His and Purkinje fibers, as well as a tailored workflow taking advantage of dynamics in the data, the model allows for estimation of parameters governing both refractory period and conduction delay in a robust manner from non-invasive data during AF. The ultimate aim of this work is to monitor and predict the outcome of treatment with rate control drugs in clinical settings to assist in treatment selection. In order to do this, a robust characterization of the AV node is needed, and thus the purpose of this study is to: (1) Describe and motivate the model; (2) Present a tailored workflow for estimation of parameters; (3) Demonstrate that presented combination of model and workflow leads to robust parameter estimates that mimic measured data well.

2. MATERIALS AND METHODS

The model of the AV node will be explained in section 2.1, followed by a description of the data used to evaluate said model in sections 2.2 and 2.3. In section 2.4, the methodology for model parameter estimation is explained; which combined with the optimization algorithm described in section 2.5 constitutes the workflow.

2.1. Network Model of the Human AV Node

The model of the AV node, shown in **Figure 1**, consists of a network of nodes and is based on the model presented in Wallman and Sandberg (2018). The model consists of two pathways, representing the SP and the FP, connected with a coupling node. Each pathway is modeled with 10 nodes, where each node corresponds to a localized part of the AV node. Each node can block incoming impulses or send them through adding a conduction delay. All nodes but the coupling node sends impulses to all other nodes connected to it, whereas the coupling node only receives impulses. A new refractory period $[R_i(n)]$ and conduction delay $[D_i(n)]$ are calculated every time a node (i) receives a new impulse (n). The refractory period and conduction delay are based on the stimulation history of the node and are described using exponential functions. These exponential functions have previously been used to fit AV node characteristics (Shrier et al., 1987; Lian et al., 2006; Wallman and Sandberg, 2018), and can be seen in Equations (1–3).

$$R_i(n) = R_{min} + \Delta R(1 - e^{-\tilde{I}_i(n)/\tau_R}) \quad (1)$$

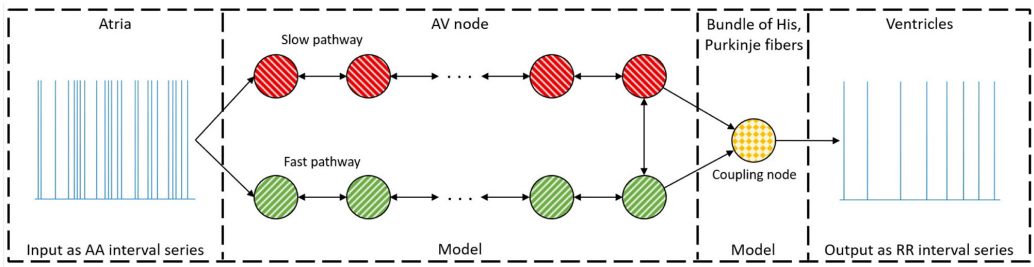

FIGURE 1 | A schematic representation of the proposed model. The arrow indicates the direction an impulse can conduct, and the colors represent nodes with the same parameter sets. For simplicity, only a subset of the ten nodes in each pathway are showed.

$$D_i(n) = D_{min} + \Delta D e^{-\tilde{t}_i(n)/\tau_D} \tag{2}$$

$$\tilde{t}_i(n) = t_i(n) - t_i(n-1) - R_i(n-1) \tag{3}$$

Here $\tilde{t}_i(n)$ refers to diastolic interval preceding impulse n, $t_i(n)$ the arrival time of impulse n at node i, and $t_i(n-1)$ and $R_i(n-1)$ the arrival time and refractory period of impulse $n-1$ at node i, respectively. If $\tilde{t}_i(n)$ is negative, the node will still be in its refractory period and thus the impulse will be blocked. The model parameters defining minimum refractory period, R_{min}; maximum prolongation of refractory period, ΔR; time constant τ_R; minimum conduction delay, D_{min}; maximum prolongation of conduction delay, ΔD; and the time constant τ_D, are assumed to be fixed for the nodes in the SP and FP, respectively.

The coupling node models the total refractoriness and conduction delay introduced by the connection between the AV node and the bundle of His, the Purkinje fibers, and the bundle of His. This node has a separate set of parameters, representing separate functional properties, and will be denoted the His and Purkinje (HP) node. The refractory period for the Purkinje fibers is assumed to not affect the ventricular activation during AF. Thus, the whole refractory period for the HP node is determined by the bundle of His. However, the conduction delay for the HP node is viewed as the time it takes an impulse to travel from the start of the bundle of His to the end of the Purkinje fibers. The conduction delay from the start of the bundle of His until the end of the Purkinje fibers has clinically been showed to have a mean of 60 ms with a standard deviation of 10 ms for patients suffering from AF (Deshmukh et al., 2000). Thus, the conduction delay for the HP node is fixed at 60 ms. The HP node's refractory period is estimated by the mean of the ten shortest RR intervals, RR_{min}.

This results in 12 free parameters for the proposed model, denoted as a parameter vector $\theta = [R^{FP}_{min}, \Delta R^{FP}, \tau^{FP}_R, R^{SP}_{min}, \Delta R^{SP}, \tau^{SP}_R, D^{FP}_{min}, \Delta D^{FP}, \tau^{FP}_D, D^{SP}_{min}, \Delta D^{SP}, \tau^{SP}_D]$. It is assumed that the first node of each pathway is simultaneously stimulated for incoming impulses from the atria. The model can then be used to produce a RR interval series with minimal computational demands using a modified version of Dijkstra's algorithm (Wallman and Sandberg, 2018). A link to the code for the model together with a basic user example can be found at section 5. The total minimum conduction delay and maximum prolongation, defined as $D^{FP}_{min,tot} = N_n D^{FP}_{min}$; $\Delta D^{FP}_{tot} = N_n \Delta D^{FP}$; $D^{SP}_{min,tot} = N_n D^{SP}_{min}$; $\Delta D^{SP}_{tot} = N_n \Delta D^{SP}$; where $N_n = 10$ are the number of nodes in each pathway, are introduced for convenience of presentation.

2.2. ECG Data

This study was based on ambulatory ECG data from the RATe control in Atrial Fibrillation (RATAF) study, which is approved by the regional ethics committee and the Norwegian medicines agency and was conducted in accordance with the Helsinki Declaration (Ulimoen et al., 2013). The RATAF study contains 24-h Holter recordings of 60 patients under baseline and during treatment with four different rate reducing drugs. All patients had permanent AF, no heart failure or symptomatic ischemic heart disease, an age of 71 ± 9 (mean ± std), and 70% were men. To evaluate the presented model, we selected 15 min ECG segments, one for each of five patients, obtained under baseline conditions between 1:00 and 3:00 pm. These five patients were selected to be representative for the whole data set, with varying RR interval series characteristics and an average heart rate ranging between 63 and 140 bpm. In addition, corresponding ECG data obtained during treatment with Diltiazem was also used for one of the five patients.

The RR interval series were extracted from the ECG signals by first detecting the R peaks, before removing RR intervals preceding and following ectopic beats identified based on heartbeat morphology (Lagerholm et al., 2000). Along with this, the mean arrival rate of the atrium-to-atrium (AA) intervals was estimated from the f-waves in the ECG by first extracting the atrial activity from the ECG using spatiotemporal QRST cancellation (Stridh and Sornmo, 2001), before tracking the atrial fibrillatory rate (AFR) using a method based on a hidden Markov model (Sandberg et al., 2008). Finally, correction of the atrial fibrillatory rate by taking the atrial depolarization time into account was used to obtain an estimate of the arrival rate. Here, we denote the true mean arrival rate λ, and the estimated mean arrival rate $\hat{\lambda}$. One value of $\hat{\lambda}$ was obtained for each ECG segment (Corino et al., 2013).

TABLE 1 | Characteristics of the data extracted from ECG and the simulated data, respectively, for all five patients.

Parameter	Patient 1	Patient 2	Patient 3	Patient 4	Patient 5
MEASURED DATA					
Average HR (ms)	76.4	62.7	90.6	111.9	139.9
$\hat{\lambda}$ (Hz)	8.45	9.13	6.73	9.03	10.04
SIMULATED DATA					
Average HR (bpm)	75.3	62.3	93.1	110.5	139.5
λ (Hz)	8.45	9.13	6.73	9.03	10.04
SP ratio (%)	54	60	85	77	92
R_{min}^{FP} (ms)	210	390	379	465	378
ΔR^{FP} (ms)	516	475	594	1.47	383
τ_R^{FP} (ms)	168	217	222	113	145
R_{min}^{SP} (ms)	205	313	280	257	287
ΔR^{SP} (ms)	469	422	233	0.00	103
τ_R^{SP} (ms)	220	40	204	172	227
D_{min}^{FP} (ms)	4.77	1.13	1.44	9.05	6.43
ΔD^{FP} (ms)	11.2	20.6	16.0	20.3	34.4
τ_D^{FP} (ms)	155	237	40.0	40.0	145
D_{min}^{SP} (ms)	21.1	25.4	21.7	16.0	20.2
ΔD^{SP} (ms)	51.9	15.1	4.62	3.74	2.47
τ_D^{SP} (ms)	89.9	232	166	91.1	165

2.3. Simulated Data

Simulated data were created by fitting the model to the RR interval series from the five patients, cf. section 2.5, and using the resulting estimated model parameters to simulate an RR interval series of 20 min. The sequence of atrial impulses arriving to the AV node, and thus the input to the model, were simulated using a Poisson process with the mean arrival rate set to the value of $\hat{\lambda}$ estimated for each patient (Corino et al., 2011; Henriksson et al., 2015). The parameter values used for the simulated data, along with average heart rate of the simulated RR interval series, are summarized in **Table 1**.

2.4. Model Parameter Estimation

To evaluate how well the model matches the extracted RR interval series, a fitness function comparing the model output to the RR interval series is used. In order to take the dynamics of the RR interval series into account, the Poincaré plot is used as a basis for the fitness function. The Poincaré plot is a scatter plot of successive pairs of RR intervals. To use the Poincaré plot as a fitness function, the RR interval series is binned into two dimensional bins centered between 250 and 1,800 ms in steps of 50 ms, resulting in $N = 961$ bins. The error function is computed according to Equation (4).

$$\epsilon = \frac{1}{N}\sum_{i=1}^{N}\left((x_i - \tilde{x}_i)^2/\sqrt{\tilde{x}_i}\right) \tag{4}$$

Here ϵ is the error value, and $\tilde{x}_i$ and x_i the number of RR intervals, in the i-th bin, of the measured data and model output, respectively. The normalization by $\sqrt{\tilde{x}_i}$ is introduced to avoid bins with a large number of data points to dominate the optimization. The square root is used as a trade-off between no normalization, making the bins with a large number of data points dominate, and normalization with the whole measured bin counts, making the accuracy of every bin have the same weight regardless of how much of the data are in that bin. A schematic representation of the parameter estimation process can be seen in **Figure 2**.

2.5. Genetic Algorithm

An initial study of how ϵ varies with varying model parameter values revealed a highly chaotic structure with a large number of local minima. This prompted us to minimize ϵ using a genetic algorithm (GA). A brief description of the algorithm is given below, with more detailed information in the **Supplementary Section 1**. Due to the high dimensional parameter space and the risk of premature convergence early in the optimization, a variant of an island model was used (Wahde, 2008). A schematic representation of the GA is shown in **Figure 3**. As visible in the figure, the full GA can be divided into two sections. The first section consists of five separate GA. This was implemented by restarting the algorithm five times with 300 individuals in each generation. The individuals in each starting run were initialized using a latin hypercube sampling in the ranges: $\{R_{min}^{SP}, R_{min}^{FP}\} \in [250, 600]$ *ms*; $\{\Delta R^{SP}, \Delta R^{FP}\} \in [0, 600]$ *ms*, $\{\tau_R^{SP}, \tau_R^{FP}\} \in [50, 300]$ *ms*; $\{D_{min}^{SP}, D_{min}^{FP}\} \in [0, 30]$ *ms*; $\{\Delta D^{SP}, \Delta D^{FP}\} \in [0, 75]$ *ms*; $\{\tau_D^{SP}, \tau_D^{FP}\} \in [50, 300]$ *ms*. These starting runs last for six generations, and after each run the best 150 of the individuals are saved and used in the second section, the main GA. Thus, the main GA uses a population

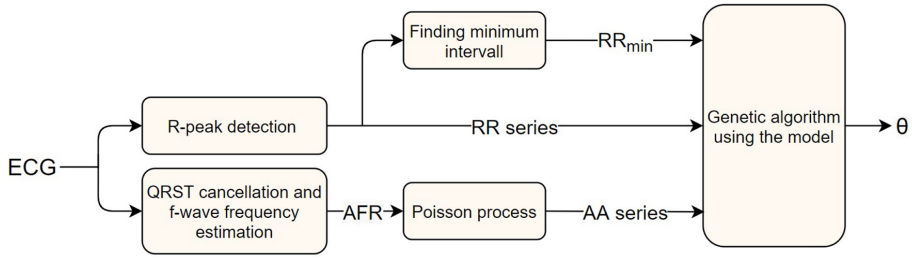

FIGURE 2 | A block diagram of the AV node model parameter estimation workflow, starting with a measured ECG signal and ending with estimated parameters.

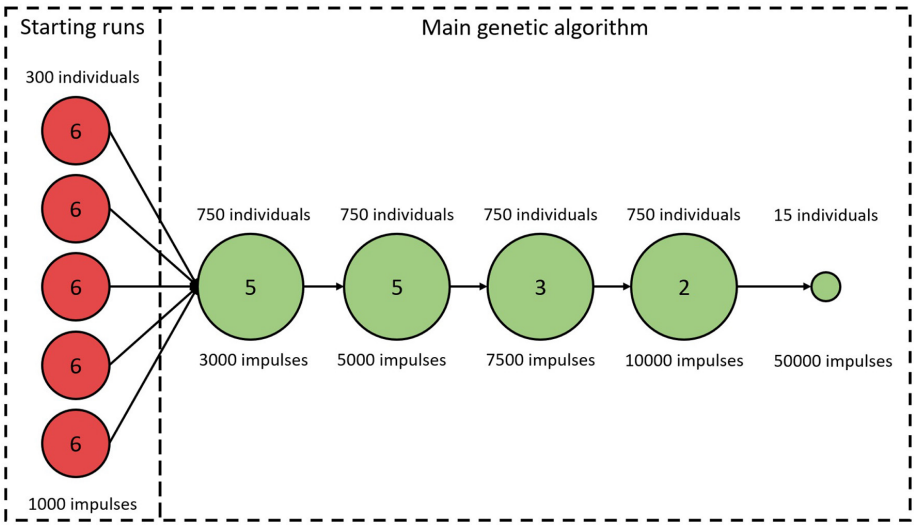

FIGURE 3 | A schematic representation of the genetic algorithm. Circles represent stages of the algorithm with constant number of individuals and L_{RR}. Numbers in circles correspond to the number of iterations before proceeding to the next stage. The last stage is always used, even if the GA terminates early.

of 750 individuals in each generation. For both the starting runs and the main GA, the 2.5% fittest individuals in each generation survives into the next generation unchanged, whereas the remaining individuals are created via tournament selection, two-point crossover, and creep mutation (Wahde, 2008). In order to avoid premature convergence, both incest prevention in the form of mating restriction between too similar individuals during crossover, and a varying mutation rate depending on the diversity of the individuals in each generation were implemented (Wahde, 2008). This process of selection, crossover, and mutation is then continued until termination. The termination of the starting runs always occurs after six generations. The termination for the main GA occurs either when ϵ for the fittest individual in each generation does not change for three generations, or when 15 generations have been run. The fittest individual for the k-th generation, $\hat{\epsilon}_k$, is deemed to have changed if the difference between $\bar{\hat{\epsilon}}(k)$ and $\bar{\hat{\epsilon}}(k-2)$, seen in Equation (5), is lower than 25.

$$\bar{\hat{\epsilon}}(k) = \frac{\hat{\epsilon}_k + \hat{\epsilon}_{k-1} + \hat{\epsilon}_{k-2}}{3} \tag{5}$$

As described in section 2.3, a Poisson process with mean arrival rate $\hat{\lambda}$ was used as input to the model, and due to the stochastic nature of the Poisson process, ϵ varies between realizations. The magnitude of this variation was analyzed by finding a parameter set replicating the extracted RR interval series from patient 3 well, before simulating that parameter set with different lengths of the resulting RR interval series, L_{RR}, as seen in **Figure 4**, left panel. Each L_{RR} was simulated 1,000 times. Moreover, six more

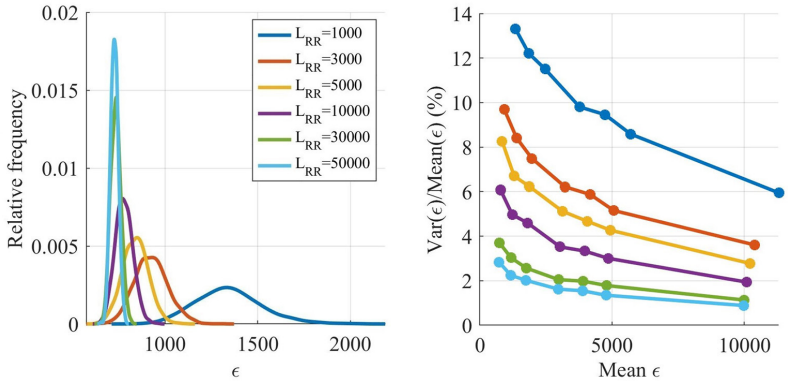

FIGURE 4 | Estimated distribution of ϵ as a function of L_{RR} **(left)**. Variance of ϵ divided by mean of ϵ as a function of the mean of ϵ **(right)**.

parameter sets with increasing ϵ were also simulated 1,000 times with the same L_{RR}, as seen in **Figure 4**, right panel.

The ϵ variation is decreasing with larger L_{RR}, however, the running time for the model is linearly increasing with L_{RR}, and thus shorter outputs are preferable. The variation of ϵ is not as important early in the optimization since the variation relative ϵ is smaller for larger ϵ, see **Figure 4**, right panel. However, after several generations most of the ϵ for individuals found by the GA are low, and thus the variability in ϵ has a larger impact on the algorithm. Therefore, L_{RR} is increased throughout the optimization.

As seen in **Figure 3**, the L_{RR} for all generations in the starting runs were 1,000 impulses. For the main GA, the first five generations used a L_{RR} of 3,000 impulses, the following five generations a L_{RR} of 5,000 impulses, followed by three generations with length of 7,500 impulses, before ending with two 10,000 impulses long generations. To obtain a robust estimate of $\bar{\hat{\epsilon}}(k)$, the individual with the best fit in each generation is evaluated again with a L_{RR} of 10,000. After termination for the main GA, the 15 fittest individuals were tested again, with a L_{RR} of 50,000; this in order to select the fittest individual with a low variation in ϵ.

3. RESULTS

The RR interval series extracted from the ECG along with the simulated data, cf. sections 2.2 and 2.3, are used to evaluate the proposed methodology. In section 3.1, the proposed approach for optimization is compared to using only the main GA with fixed L_{RR}. The robustness and precision of the parameter estimation are evaluated using simulated data in section 3.2. Further, the robustness of the estimates is set in perspective by using the model to estimate AV node characteristics for one of the patients during both baseline and under influence of the calcium channel blocker drug Diltiazem. In section 3.3, the proposed model is compared to the model presented in Wallman and Sandberg (2018).

3.1. Genetic Algorithm

The effect of using an island based start together with varying L_{RR} was evaluated by comparing it to using only the main GA, as described in section 2.5, with L_{RR} fixed at 5,000. The initialization for this fixed GA was the same as for the starting runs, a latin hypercube sampling in the same ranges, and the population size was again 750. Performances of the two methods were evaluated by comparing the error value of the fittest individual for each generation, $\hat{\epsilon}_k$ with the cumulative L_{RR} used for the evaluations, i.e., the accumulated total number of impulses in each generation. For the different starting runs, all runs were computed in parallel so that $\hat{\epsilon}_k$ during this stage is the lowest value out of all the five starting runs. The average results from comparing the two versions of the GA on all five patients, each 100 times, are shown in **Figure 5**. From this it is possible to see that a lower $\hat{\epsilon}_k$, and thus a better fit to the RR interval series, can be found in less computational time using the proposed methodology. For reference, estimating the parameters for one patient using a single core on a standard desktop computer (Intel® Core™ i7-6600U Processor, @ 2.60GHz) requires on average 20 min, with variations due to the different terminating requirements for the GA. It is also possible to see that the termination criteria for a maximum number of generations stated in section 2.5 is typically achieved after the GA has converged.

3.2. Parameter Estimation Robustness

Simulated RR interval series were used to evaluate the robustness of the model parameter estimates. The results from optimizing the model 200 times for the five simulated RR interval series can be seen in **Table 2**, where the mean and standard deviation for each of the 12 estimated parameters, for each of the five patients, are listed. Moreover, the mean error, defined as the difference between the mean value of the estimated parameter

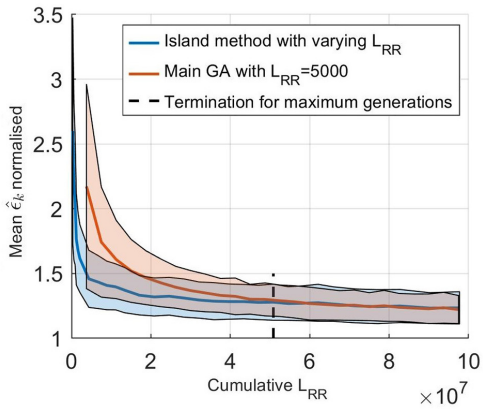

FIGURE 5 | (solid line) Mean normalized $\hat{\epsilon}_k$ of 100 optimizations of the five set of patient data as a function of cumulative L_{RR} for (blue) the island start optimization with varying L_{RR} and (orange) only the main GA with a fix L_{RR} at 5,000. The shaded background represents one standard deviation. Here, $\hat{\epsilon}_k$ is normalized with the best ϵ found for each patient, to account for the fact that the model can not fit each RR interval series equally well.

and the ground truth, averaged over the five patients, are also listed. Furthermore, the mean and standard deviation of the error normalized with respect to the parameter ranges, cf. section 2.5, are presented. From the SP ratio it is evident that the SP is used more for transmission, and from the normalized error, it is evident that the parameters associated with the SP are more robustly estimated. The histogram and Poincaré plots for the five simulated patients with the transmission pathway for each RR interval marked out can be seen in **Supplementary Section 3**, together with the simulated histograms showing the effect of changes to λ.

To set the robustness in perspective, the AV nodal properties were estimated 200 times for a single patient during baseline and under the influence of the non-dihydropyridine calcium channel blocker rate control drug Diltiazem. The results, shown in **Figure 6**, indicate that the uncertainty in the parameter estimation is sufficiently low in order to reveal the drug effect.

3.3. Model Comparison

To evaluate the ability of the model and proposed workflow to represent AF data and to have a frame of reference, the proposed model is compared with the model presented in Wallman and Sandberg (2018); henceforth denoted the reference model. Both models were fitted to the RR interval series from one example patient, and the properties of the resulting simulated RR interval series are shown in the form of histograms, Poincaré plots, and autocorrelations, as seen in **Figure 7**. For both models, the optimizer was run until no change in error value for the fittest individual during ten generations occurred, to assure convergence. Both models used the optimizer described in section 2.5, but the reference model uses a fitness function based on the histogram (Wallman and Sandberg, 2018). It is clear from both the Poincaré plots and the autocorrelation plots that the proposed model can better replicate the dynamics of the RR interval series. The fit to the Poincaré plot can be quantified by the resulting ϵ, which for the proposed model was 1,360, compared to 6,740 for the reference model. Similarly, the value for the first lag autocorrelation was −0.07 for the proposed model and 0.52 for the reference, compared to the ground truth at −0.07.

4. DISCUSSION

In this study, a mathematical model of the AV node, bundle of His, and Purkinje network has been presented together with a fitness function accounting for RR interval dynamics and genetic algorithm tailored to the model. The model and workflow have been evaluated with respect to robustness, accuracy, and ability to represent data, using both measured and simulated data.

Ten nodes in each pathway were used as a trade-off between detail and computation time. A small number of nodes can make the conduction delay larger than the refractory period, allowing impulses to bounce back and forth, whereas a large number of nodes leads to a higher computational demand. The inclusion of a last node in the model as functionally distinct from the SP and FP has previously been used in other models of the AV node (Inada et al., 2009). The incorporation of separate conduction properties for the connecting node introduced both new refractory period and conduction delay parameters. However, literature data suggests that inter-patient variability in conduction time over the bundle of His and the Purkinje network is around 10 ms (Deshmukh et al., 2000), indicating that the parameters representing the conduction delay could be reasonably approximated by a constant value. Furthermore, an initial study was conducted in which the refractory period of the HP node was represented by Equation (1), with three free parameters. This study showed that the parameter values representing the refractory period in the HP node found after optimization matched a constant value of RR_{min}, independent of $\tilde{t}_i(n)$, well; indicating a good approximation (data not shown). For more details about the parameter values of the HP node during the optimizations, see **Supplementary Section 2**.

Reducing the number of free parameters reduces the parameter space in which the GA operates, and in turn decreases the running time as well as increases the robustness for the optimization. The parameters for the HP node were especially advantageous to fix or estimate directly from data. This was partly because the clinical data and analysis of the optimization made it possible, and partly because the most interesting information regarding the AV node is contained in the parameters governing SP and FP. Thus, setting the parameters corresponding to the bundle of His and Purkinje fibers to fixed values enhanced the ability of our method to estimate AV node properties.

The optimizer in this work utilized the fact that the model could be used with varying speed and precision by changing the output length, with higher speed and lower precision at the start and shifting it during the optimization. This change

TABLE 2 | The mean parameter values ± standard deviation of 200 optimizations for the five simulated data sets, together with the mean error ± mean standard deviation for each parameter.

Parameter	Patient 1	Patient 2	Patient 3	Patient 4	Patient 5	Error	Normalized error (%)
R_{min}^{FP} (ms)	311 ± 104	394 ± 53	430 ± 49	424 ± 45	419 ± 72	31.7 ± 65	7.9 ± 16
ΔR^{FP} (ms)	436 ± 74	495 ± 57	479 ± 55	164 ± 131	393 ± 69	-0.3 ± 77	-0.1 ± 12
τ_R^{FP} (ms)	184 ± 38	211 ± 35	168 ± 39	183 ± 63	167 ± 53	9.4 ± 45	3.6 ± 17
R_{min}^{SP} (ms)	225 ± 17	369 ± 71	271 ± 11	247 ± 8	281 ± 5	10.3 ± 22	2.6 ± 6
ΔR^{SP} (ms)	430 ± 26	358 ± 60	247 ± 14	28 ± 20	101 ± 4	-12.6 ± 26	-1.9 ± 4
τ_R^{SP} (ms)	201 ± 29	56 ± 10	216 ± 26	204 ± 55	198 ± 41	2.2 ± 32	0.8 ± 12
$D_{min,tot}^{FP}$ (ms)	65 ± 31	36 ± 22	53 ± 21	69 ± 39	92 ± 38	17 ± 29	5.7 ± 10
ΔD_{tot}^{FP} (ms)	188 ± 92	273 ± 9.6	193 ± 95	248 ± 119	336 ± 145	43 ± 109	5.7 ± 15
τ_D^{FP} (ms)	132 ± 48	150 ± 43	133 ± 47	135 ± 47	154 ± 47	17 ± 46	7.1 ± 19
$D_{min,tot}^{SP}$ (ms)	184 ± 36	245 ± 25	246 ± 23	197 ± 47	209 ± 43	7 ± 35	2.5 ± 12
ΔD_{tot}^{SP} (ms)	395 ± 73	214 ± 45	88 ± 19	66 ± 31	35 ± 11	4 ± 36	0.5 ± 5
τ_D^{SP} (ms)	173 ± 33	187 ± 42	167 ± 39	179 ± 55	183 ± 47	29 ± 43	12 ± 18
Average HR (bpm)	75.3 ± 0.7	62.6 ± 0.5	93.6 ± 0.7	110.9 ± 1	139.2 ± 1	0.2 ± 0.8	-
SP ratio (%)	54	60	85	77	92	-	-

The normalized error ± standard deviation as well as the ratio of impulses passing through the SP are also presented.

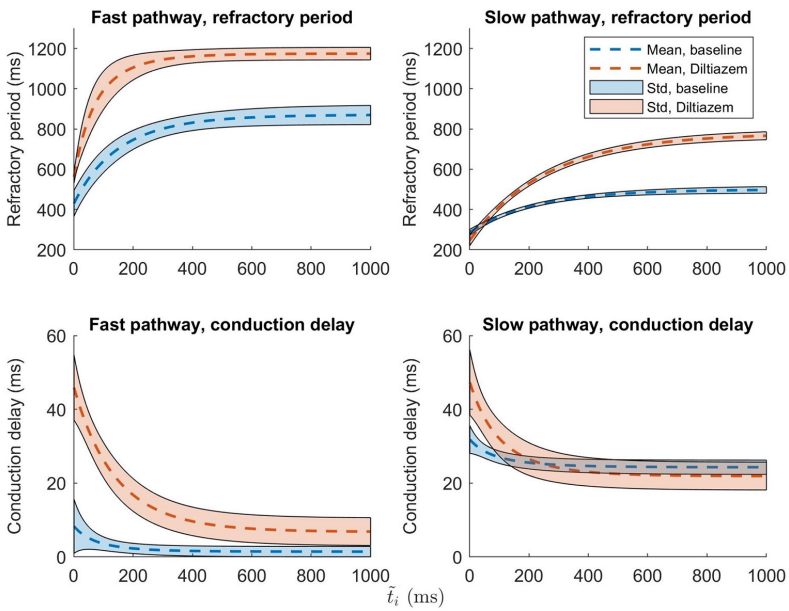

FIGURE 6 | The mean ± one standard deviation, indicated by the shaded background, of the estimate refractory period and conduction delay from Equation (1) and (2), after 200 runs, are plotted for both baseline (blue) and Diltiazem (orange).

in output length also made it possible to run a broad search of the parameter space fast at the start of the optimization by restarting it several times; reducing the risk that a parameter set producing a good fit to the RR interval series was missed. This led to finding parameter sets matching the data faster, as shown in **Figure 5**. With a computing time of 20 min on a standard desktop computer in order to estimate the parameters, it possible to utilize the model without the use of any cloud computing or supercomputer, making it suitable for routine off-line analysis of Holter recordings.

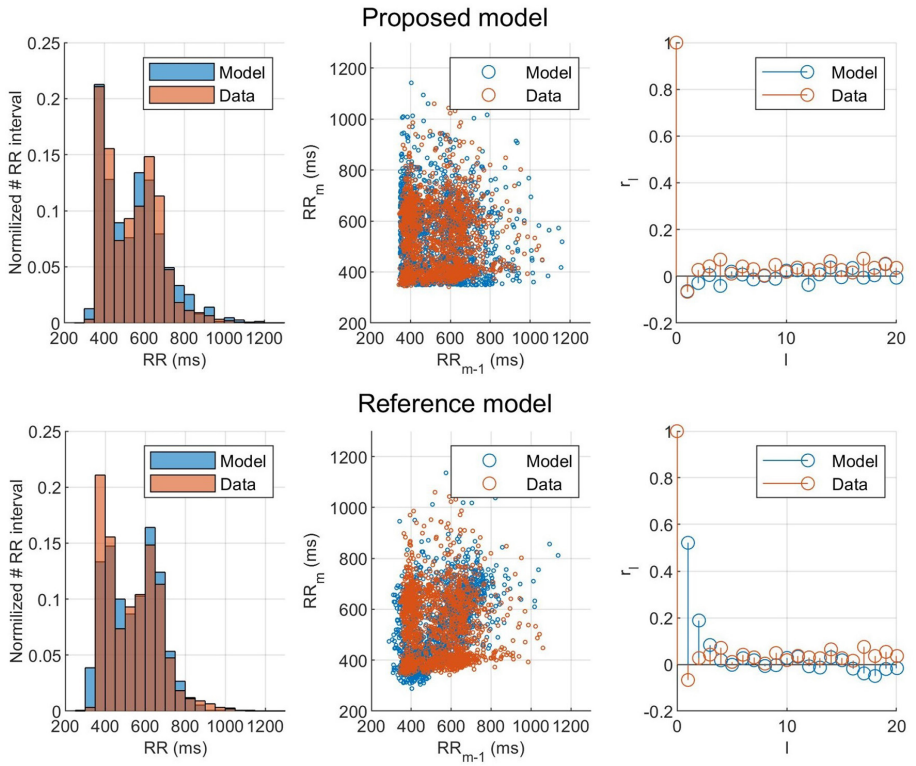

FIGURE 7 | Histogram, Poincaré plot, and autocorrelation representation of the (orange) observed and (blue) modeled RR interval series for **(top)** the fitted proposed model and **(bottom)** the fitted reference model.

The result of taking the RR interval series dynamics into account during the optimization can clearly be seen in **Figure 7**, where the proposed model and fitness function could represent the Poincaré plot with an ϵ five times as low as the reference model. This shows that matching the histograms well, as both models did, does not necessarily mean that the model represents the RR interval dynamics well. Using the Poincaré plot as basis for the fitness function, it was possible to account for the RR interval distribution and the one-step autocorrelation at the same time. It should be noted that the information from the histogram is still indirectly included in the Poincaré plot, which is likely the reason why the proposed fitness function also gave well matched histograms.

Since no ground truth of the estimated parameters is available for the clinical data, it is not possible to directly verify their correctness. However, it is still possible to verify that the parameter values lay within ranges reported in literature. The conduction delay for the HP node is fixed based on clinical data, thus it lies within reasonable ranges by default. The refractory period for the HP node was estimated using RR_{min}, and for the five patients used in this study the range was [292, 655] ms. Comparing this to the bundle branch refractory period of [305, 520] ms, and the His-Purkinje system relative refractory period of [330, 460] ms, reported in Denes et al. (1974), it seems reasonable.

It is difficult to assess AV conduction delay during AF, due to problems in determining which atrial impulse activated the ventricles. However, the total minimum and maximum prolongation of conduction delay parameters of the AV node, $D^{FP}_{min,tot}$, ΔD^{FP}_{tot}, $D^{SP}_{min,tot}$, and ΔD^{SP}_{tot}, have previously been estimated by mathematical models utilizing the relationship between diastolic interval and delay in Equation (2). One such example is the model by Mangin et al. (2005), which uses invasive data, for which the ranges of $D_{min,tot}$, ΔD_{tot}, and τ_D were [80,300], [15,125], and [80,340], respectively. These ranges are of the same order of magnitude as the values obtained for $D_{min,tot}$, ΔD_{tot}, and τ_D in the present study, cf **Table 2**. It should be noted that the present model, contrary to the Mangin model, has two pathways where shorter delays are expected for the FP than for the SP.

The maximum refractory period, defined as the sum of R_{min} and ΔR, can be compared with electrophysiological measurements of the AV node effective refractory period. The values obtained in the present study were in the ranges [466, 973] and [257, 735] ms for the FP and SP, respectively. AV node effective refractory periods from patients with reentrant tachycardia have been reported in the ranges 361 ± 57 and 283 ± 48 ms for the FP and SP, respectively (Natale et al., 1994). As expected, the FP has larger values in both model and measurements.

The use of simulated data was necessary in order to have a ground truth to compare the estimated parameters with and in turn evaluate the methodology. From these five simulated data sets, it is clear that all of them primarily used the SP, cf. **Table 2**, although the SP ratio differed. This higher usage of the SP may be a contributing factor to that the parameters representing the SP were more accurately estimated than the parameters representing the FP. Moreover, the parameters τ_R^{SP}, τ_R^{FP}, τ_D^{SP}, and τ_D^{FP} all have a larger error, which might imply that they have smaller overall effect on the model output. Further, histograms and Poincaré plots highlighting the transmission pathway for the RR intervals (cf. **Supplementary Section 3**) show that longer RR intervals tend to be transmitted via the FP, which is to be expected given its lower total conduction time. More interestingly, it is evident that different histogram peaks generated by the model are not created solely from one pathway, but stem from complex interaction between both the FP and SP. Moreover, it should also be noted that the difference in heart rate between the observed RR interval series and the RR series produced by the fitted model was less than one beat per minute.

It is evident from the example in **Figure 6** that the uncertainty in conduction delay and refractory period introduced by the parameter estimation is generally lower than the effect of the drug, thus suggesting that it is possible to assess the effect of rate control drugs on the AV node from non-invasive data. For the example patient, the difference in conduction delay for the SP between baseline and Diltiazem is minimal for $\tilde{t}_i > 200$ ms. However, one patient is not enough to know if this is a feature specific to this particular patient, a property of the investigated drug, or an artifact of the model formulation. The effect of rate control drugs on the AV node refractory period have previously been investigated (Sandberg et al., 2015), and with the proposed methodology a similar investigation can be done for AV node conduction delay.

4.1. Limitations and Future Work

The main limitation of the present study is the lack of comparison between the estimated parameter and the ground truth AV node characteristics, making the results more difficult to evaluate. Although simulated data was used as a substitute, it is not fully known how closely it matches reality. Another limitation is the assumption that both pathways are activated simultaneously, an assumption that may not be valid, since the electrical activity in the atria is highly disorganized. The variation in output originating from the stochastic input sequence can also be seen as a limitation to the proposed model, since the output for a single set of parameters can vary depending on the realization of the input sequence. However, without electrical measurements in the atria, it is not possible to model the exact behavior of the AV node.

Moreover, due to the computational time of estimating the parameters for each simulated RR interval series 200 times, only a subset of RATAF was used. However, the five patients were selected to ensure a representative subset based on their RR interval series characteristics. It should be noted that the focus of the present study is to evaluate the robustness in parameter estimation rather than analysis of the RATAF data set. Using the model to analyze the entire RATAF data set, including all patients, drugs, and time segments for outcome prediction forms a natural next step in this line of inquiry, and efforts toward this goal are ongoing at the time of writing.

Example results, cf. **Figure 6**, suggest that the estimates of refractory period and conduction delay are sufficiently robust to detect changes in response to treatment with rate control drugs. However, this needs to be verified in a larger study population. By using the model to simulate the treatment effect of different drugs in a patient-specific setting, it might be possible to predict the outcome of the drug treatment and thus assist in treatment selection. Furthermore, it could also be useful in drug development, by aiding in understanding what AV node properties are affected by a novel compound, and in what way.

5. CONCLUSION

We have described and motivated a network model of the AV node, bundle of His, and Purkinje network. The model is demonstrated to be able to represent RR interval series extracted from ECG data well, both in the forms of histograms, Poincaré plots, and autocorrelation. This was made possible using the presented problem specific fitness function and optimization algorithm, taking advantage of the model's ability to increase running speed at the cost of precision. The robustness in parameter estimation enabled fitting of delay specific parameters from the AV node solely based on the ECG. It also made it possible to detect changes to the model parameters originating from the use of a rate control drug.

In summary, the combination of model and parameter estimation workflow presented here constitutes a significant improvement on previous AV node modeling efforts, suggesting the possibility to use ECG measurements to analyze drug effect on the AV node on a patient specific level.

DATA AVAILABILITY STATEMENT

The simulated data supporting the conclusions for this article will be available from the authors upon request. The measured data are owned by Vestre Viken Hospital Trust, and requests for access can be made to Sara R. Ulimoen. The code for the model together with an user example can be found at https://github.com/FraunhoferChalmersCentre/AV-node-model.

ETHICS STATEMENT

The studies involving human participants were reviewed and approved by the Norwegian Medicines Agency. The patients/participants provided their written informed consent to participate in this study.

AUTHOR CONTRIBUTIONS

MK, FS, and MW contributed to conception and design of the study. SU gathered and organized all raw data. FS computed and organized all RR interval series and λ. MK designed the changes to the model as well as the genetic algorithm with advice, suggestions, and supervision from FS and MW, and wrote the manuscript. FS and MW supervised the project and revised the manuscript during all the writing process. All authors contributed to manuscript revision, read, and approved the submitted version.

FUNDING

This work was supported by the Swedish Foundation for Strategic Research (Grant FID18-0023), the Swedish Research Council (Grant VR2019-04272), and the Crafoord Foundation (Grant 20200605).

SUPPLEMENTARY MATERIAL

The Supplementary Material for this article can be found online at: https://www.frontiersin.org/articles/10.3389/fphys.2021.728955/full#supplementary-material

REFERENCES

Benjamin, E. J., Muntner, P., Alonso, A., Bittencourt, M. S., Callaway, C. W., Carson, A. P., et al. (2019). Heart disease and stroke statistics-2019 update a report from the american heart association. *Circulation* 139, e56–e528. doi: 10.1161/CIR.0000000000000659

Climent, A. M., Guillem, M. S., Zhang, Y., Millet, J., and Mazgalev, T. (2011). Functional mathematical model of dual pathway AV nodal conduction. *Am. J. Physiol. Heart Circ. Physiol.* 300, H1393–H1401. doi: 10.1152/ajpheart.01175.2010

Corino, V. D., Sandberg, F., Lombardi, F., Mainardi, L. T., and Sörnmo, L. (2013). Atrioventricular nodal function during atrial fibrillation: model building and robust estimation. *Biomed. Signal Process. Control* 8, 1017–1025. doi: 10.1016/j.bspc.2012.10.006

Corino, V. D., Sandberg, F., Mainardi, L. T., and Sornmo, L. (2011). An atrioventricular node model for analysis of the ventricular response during atrial fibrillation. *IEEE Trans. Biomed. Eng.* 58, 3386–3395. doi: 10.1109/TBME.2011.2166262

Denes, P., Wu, D., Dhingra, R., Pietras, R. J., and Rosen, K. M. (1974). The effects of cycle length on cardiac refractory periods in man. *Circulation* 49, 32–41. doi: 10.1161/01.CIR.49.1.32

Deshmukh, P., Casavant, D. A., Romanyshyn, M., and Anderson, K. (2000). Permanent, direct his-bundle pacing: a novel approach to cardiac pacing in patients with normal his-Purkinje activation. *Circulation* 101, 869–877. doi: 10.1161/01.CIR.101.8.869

Henriksson, M., Corino, V. D., Sörnmo, L., and Sandberg, F. (2015). A statistical atrioventricular node model accounting for pathway switching during atrial fibrillation. *IEEE Trans. Biomed. Eng.* 63, 1842–1849. doi: 10.1109/TBME.2015.2503562

Hindricks, G., Potpara, T., Dagres, N., Arbelo, E., Bax, J. J., Blomström-Lundqvist, C., et al. (2020). 2020 ESC guidelines for the diagnosis and management of atrial fibrillation developed in collaboration with the European Association of Cardio-Thoracic Surgery (EACTS) the Task Force for the Diagnosis and Management of Atrial Fibrillation of the European Society of Cardiology (ESC) developed with the special contribution of the European Heart Rhythm Association (EHRA) of the ESC. *Eur. Heart J.* 42, 373–498. doi: 10.1093/eurheartj/ehaa612

Inada, S., Hancox, J., Zhang, H., and Boyett, M. (2009). One-dimensional mathematical model of the atrioventricular node including atrio-nodal, nodal, and nodal-his cells. *Biophys. J.* 97, 2117–2127. doi: 10.1016/j.bpj.2009.06.056

Jørgensen, P., Schäfer, C., Guerra, P. G., Talajic, M., Nattel, S., and Glass, L. (2002). A mathematical model of human atrioventricular nodal function incorporating concealed conduction. *Bull. Math. Biol.* 64, 1083–1099. doi: 10.1006/bulm.2002.0313

Kurian, T., Ambrosi, C., Hucker, W., Fedorov, V. V., and Efimov, I. R. (2010). Anatomy and electrophysiology of the human AV node. *Pacing Clin. Electrophysiol.* 33, 754–762. doi: 10.1111/j.1540-8159.2010.02699.x

Lagerholm, M., Peterson, C., Braccini, G., Edenbrandt, L., and Sornmo, L. (2000). Clustering ECG complexes using hermite functions and self-organizing maps. *IEEE Trans. Biomed. Eng.* 47, 838–848. doi: 10.1109/10.846677

Lian, J., Mussig, D., and Lang, V. (2006). Computer modeling of ventricular rhythm during atrial fibrillation and ventricular pacing. *IEEE Trans. Biomed. Eng.* 53, 1512–1520. doi: 10.1109/TBME.2006.876627

Mangin, L., Vinet, A., Pagé, P., and Glass, L. (2005). Effects of antiarrhythmic drug therapy on atrioventricular nodal function during atrial fibrillation in humans. *Europace* 7, S71–S82. doi: 10.1016/j.eupc.2005.03.016

Natale, A., Klein, G., Yee, R., and Thakur, R. (1994). Shortening of fast pathway refractoriness after slow pathway ablation. effects of autonomic blockade. *Circulation* 89, 1103–1108. doi: 10.1161/01.CIR.89.3.1103

Rashidi, A., and Khodarahmi, I. (2005). Nonlinear modeling of the atrioventricular node physiology in atrial fibrillation. *J. Theoret. Biol.* 232, 545–549. doi: 10.1016/j.jtbi.2004.08.033

Sandberg, F., Corino, V. D., Mainardi, L. T., Ulimoen, S. R., Enger, S., Tveit, A., et al. (2015). Non-invasive assessment of the effect of beta blockers and calcium channel blockers on the AV node during permanent atrial fibrillation. *J. Electrocardiol.* 48, 861–866. doi: 10.1016/j.jelectrocard.2015.07.019

Sandberg, F., Stridh, M., and Sornmo, L. (2008). Frequency tracking of atrial fibrillation using hidden Markov models. *IEEE Trans. Biomed. Eng.* 55, 502–511. doi: 10.1109/TBME.2007.905488

Shrier, A., Dubarsky, H., Rosengarten, M., Guevara, M., Nattel, S., and Glass, L. (1987). Prediction of complex atrioventricular conduction rhythms in humans with use of the atrioventricular nodal recovery curve. *Circulation* 76, 1196–1205. doi: 10.1161/01.CIR.76.6.1196

Stridh, M., and Sornmo, L. (2001). Spatiotemporal QRST cancellation techniques for analysis of atrial fibrillation. *IEEE Trans. Biomed. Eng.* 48, 105–111. doi: 10.1109/10.900266

Ulimoen, S. R., Enger, S., Carlson, J., Platonov, P. G., Pripp, A. H., Abdelnoor, M., et al. (2013). Comparison of four single-drug regimens on ventricular rate and arrhythmia-related symptoms in patients with permanent atrial fibrillation. *Am. J. Cardiol.* 111, 225–230. doi: 10.1016/j.amjcard.2012.09.020

Wahde, M. (2008). *Biologically Inspired Optimization Methods: An Introduction*. Gothenburg: WIT Press.

Wallman, M., and Sandberg, F. (2018). Characterisation of human AV-nodal properties using a network model. *Med. Biol. Eng. Comput.* 56, 247–259. doi: 10.1007/s11517-017-1684-0

Conflict of Interest: The authors declare that the research was conducted in the absence of any commercial or financial relationships that could be construed as a potential conflict of interest.

Publisher's Note: All claims expressed in this article are solely those of the authors and do not necessarily represent those of their affiliated organizations, or those of the publisher, the editors and the reviewers. Any product that may be evaluated in this article, or claim that may be made by its manufacturer, is not guaranteed or endorsed by the publisher.

Paper II

frontiers | Frontiers in Physiology

TYPE Original Research
PUBLISHED 04 October 2022
DOI 10.3389/fphys.2022.976526

OPEN ACCESS

EDITED BY
Axel Loewe,
Karlsruhe Institute of Technology,
Germany

REVIEWED BY
Haibo Ni,
University of California, Davis,
United States
Michela Masè,
Institute of Mountain Emergency
Medicine, Eurac Research, Italy

*CORRESPONDENCE
Frida Sandberg,
frida.sandberg@bme.lth.se

SPECIALTY SECTION
This article was submitted to Cardiac
Electrophysiology,
a section of the journal
Frontiers in Physiology

RECEIVED 23 June 2022
ACCEPTED 05 September 2022
PUBLISHED 04 October 2022

CITATION
Karlsson M, Wallman M, Platonov PG,
Ulimoen SR and Sandberg F (2022), ECG
based assessment of circadian variation
in AV-nodal conduction during
AF—Influence of rate control drugs.
Front. Physiol. 13:976526.
doi: 10.3389/fphys.2022.976526

ECG based assessment of circadian variation in AV-nodal conduction during AF—Influence of rate control drugs

Mattias Karlsson[1,2], Mikael Wallman[1], Pyotr G. Platonov[3], Sara R. Ulimoen[4] and Frida Sandberg[2]*

[1]Department of Systems and Data Analysis, Fraunhofer-Chalmers Centre, Gothenburg, Sweden, [2]Department of Biomedical Engineering, Lund University, Lund, Sweden, [3]Department of Cardiology, Clinical Sciences, Lund University, Lund, Sweden, [4]Vestre Viken Hospital Trust, Department of Medical Research, Bærum Hospital, Drammen, Norway

The heart rate during atrial fibrillation (AF) is highly dependent on the conduction properties of the atrioventricular (AV) node. These properties can be affected using β-blockers or calcium channel blockers, mainly chosen empirically. Characterization of individual AV-nodal conduction could assist in personalized treatment selection during AF. Individual AV nodal refractory periods and conduction delays were characterized based on 24-hour ambulatory ECGs from 60 patients with permanent AF. This was done by estimating model parameters from a previously created mathematical network model of the AV node using a problem-specific genetic algorithm. Based on the estimated model parameters, the circadian variation and its drug-dependent difference between treatment with two β-blockers and two calcium channel blockers were quantified on a population level by means of cosinor analysis using a linear mixed-effect approach. The mixed-effects analysis indicated increased refractoriness relative to baseline for all drugs. An additional decrease in circadian variation for parameters representing conduction delay was observed for the β-blockers. This indicates that the two drug types have quantifiable differences in their effects on AV-nodal conduction properties. These differences could be important in treatment outcome, and thus quantifying them could assist in treatment selection.

KEYWORDS

atrial fibrillation, atrioventricular node, circadian variation, mathematical modeling, genetic algorithm, mixed effect modeling, ECG, rate control drugs

1 Introduction

Atrial fibrillation (AF) is the most common arrhythmia in the world, with a prevalence of 2–4% in the adult population Benjamin et al. (2019), reaching 7% for those aged 65 and above Di Carlo et al. (2019). It is characterized by rapid and irregular contraction of the atria, originating from highly disorganized electrical activity, and associated with an increased risk of mortality, mainly due to stroke or heart failure Hindricks et al. (2021).

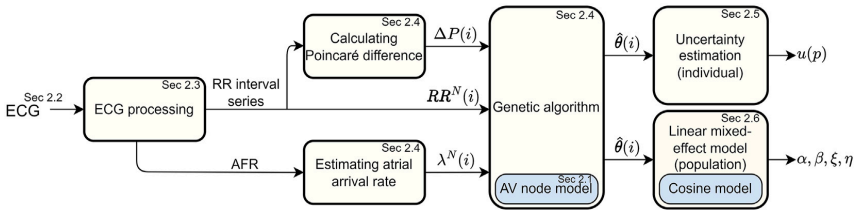

FIGURE 1
A flowchart of the overall framework for estimating AV node conduction properties on an individual and a population level.

The electrical impulses in the atria are conducted via the atrioventricular (AV) node to reach and activate the ventricles. The AV node can block and delay incoming impulses based on its refractory period and conduction delay properties. During AF - when the AV node is bombarded with impulses from the atria - blocking of impulses prevents the heart from racing, but may not be sufficient to maintain a normal heart rate and will still result in significant beat-to-beat variability in the ventricular activation Corino et al. (2015b); Mase et al. (2017).

To remedy this, rate control drugs can be used in order to modify the conduction properties of the AV node. There are two main types of rate control drugs used for AF treatment; β-blockers and calcium channel blockers Hindricks et al. (2021). As the name suggests, β-blockers block the β-receptors in AV node cells, decreasing the effect of the sympathetic nervous system, whereas calcium channel blockers prevent the L-type calcium channels from opening, thereby reducing the conduction in the AV node cells. Both types of drugs have been shown effective in reducing the heart rate during AF Ulimoen et al. (2013). However, the optimal treatment for a given patient is often chosen empirically. Since the two drug types have different physiological effects on the AV node conduction properties, assessing the drug-induced changes in these AV node properties could provide an important step toward personalized treatment. One of the main differences between the two drug types is the effect on the sympathetic nervous system, which can be quantified by the circadian variation in the AV node conduction properties. Furthermore, previous studies have shown a significant difference in the predominant RR interval between day and night, without a difference in dominant atrial cycle length, suggesting circadian variation in the AV node conduction properties Climent et al. (2010).

Conduction properties of the AV node have previously been characterized using mathematical models based on measurements of the electrical activity in the heart Shrier et al. (1987); Billette and Nattel (1994); Sun et al. (1995). Several models of the AV node during AF have been proposed; both based on invasive data from rabbits Inada et al. (2009); Climent et al. (2011) and humans Jørgensen et al. (2002); Mangin et al. (2005); Masè et al. (2012, 2015), and on non-invasive data from humans Corino et al. (2011, 2013); Henriksson et al. (2015). We have previously presented a network model of the AV node capable of assessing the refractory period and the conduction delay of the AV node from 20-min ECG segments Karlsson et al. (2021). However, continuous assessment of AV conduction delay and refractoriness from 24-hour ECG recordings has not previously been performed; such assessment enables analysis of long-term variations in AV conduction properties.

The aim of the present study is to develop a framework for long-term ECG-based assessment of conduction properties in the AV node, and to utilize this framework for analysis of circadian variation and its drug-induced changes in a cohort of 60 patients with persistent AF Ulimoen et al. (2013). To accomplish this, we propose a problem-specific optimization algorithm able to continuously estimate the model parameters from the previously presented network model Karlsson et al. (2021). Furthermore, the uncertainty of the parameter estimates is assessed using a variant of Sobol's method Sobol (2001), and the drug-induced differences in circadian variation between β-blockers and calcium channel blockers on a population level are quantified using a linear mixed-effect model.

2 Materials and methods

A schematic overview of the methodology is given in Figure 1. The ECG data (Section 2.2) is first processed in order to extract a RR interval series and an atrial fibrillatory rate (AFR) trend, as described in Section 2.3. The RR interval series is then divided into segments of length N, and the AFR trend is used to estimate the atrial arrival rate in the corresponding time interval. The AV node model (Section 2.1) is fitted to the ECG-derived data using a tailored optimization algorithm, as described in Section 2.4, in order to obtain model parameter estimates. Furthermore, the Poincaré plot difference, which quantifies the rate of change of RR series characteristics, is used to tune hyper-parameters in the optimization algorithm during parameter estimation. The uncertainty of the estimated model

parameters is investigated using a variant of Sobol's method, as described in Section 2.5. Finally, cosinor analysis is used to quantify circadian variation in the model parameter trends, and a linear mixed effects modeling approach is used to investigate drug-dependent differences on a population level, as described in Section 2.6.

2.1 AV node model

A network model of the human AV node, shown in Figure 2, is used to characterize the conduction delay and refractory period. A brief description of the model is given here, for more details, see Karlsson et al. (2021). The model describes the AV node as an interconnected network of nodes, each capable of transmitting incoming impulses. The model consists of 21 nodes; divided into a fast pathway (FP) with ten nodes, a slow pathway (SP) with ten nodes, and a coupling node. The nodes can react to an incoming impulse either by blocking - if the node is in its refractory state - or by conducting it to all adjacent nodes after adding a conduction delay, after which the node returns to its refractory state. The refractory period ($R_j(n)$) and the conduction delay ($D_j(n)$) of node j following an impulse n are given by,

$$R_j(n) = R_{min} + \Delta R\left(1 - e^{\frac{-\tilde{t}_j(n)}{\tau_R}}\right) \quad (1)$$

$$D_j(n) = D_{min} + \Delta D e^{\frac{-\tilde{t}_j(n)}{\tau_D}}, \quad (2)$$

where $\tilde{t}_j(n)$ is the diastolic interval preceding impulse n,

$$\tilde{t}_j(n) = t_j(n) - t_j(n-1) - R_j(n-1), \quad (3)$$

and $t_j(n)$ is the arrival time of impulse n at node j. When $\tilde{t}_j(n)$ is negative, the impulse will be blocked since the node is in its refractory state. The parameters $R_{\min}$, ΔR, τ_R, $D_{\min}$, ΔD, and τ_D are fixed for all nodes in the SP and the FP, respectively. This results in the 12 model parameters

TABLE 1 The interpretation of the model parameters. Superscripts indicating the pathway (SP, FP) are omitted to avoid redundancy.

Parameter	Parameter description
$R_{\min}$	Minimum refractory period, attained for short diastolic intervals
ΔR	Maximum prolongation of the refractory period, attained for long diastolic intervals.
τ_R	Time constant for the refractory period, determining the impact of the diastolic interval
$D_{\min}$	Minimum conduction delay, attained for short diastolic intervals
ΔD	Maximum prolongation of the conduction delay, attained for long diastolic intervals.
τ_D	Time constant for the conduction delay, determining the impact of the diastolic interval

$\boldsymbol{\theta} = [R_{\min}^{FP}, \Delta R^{FP}, \tau_R^{FP}, R_{\min}^{SP}, \Delta R^{SP}, \tau_R^{SP}, D_{\min}^{FP}, \Delta D^{FP}, \tau_D^{FP}, D_{\min}^{SP}, \Delta D^{SP}, \tau_D^{SP}]$. For convenience, the interpretation of the model parameters are given in Table 1. For the coupling node, the delay is fixed to 60 ms, and the refractory period is fixed to the mean of the ten shortest RR intervals in the data used for model parameter estimation, $RR_{\min}$.

The input to the model - representing impulses arriving from the atria - is created using a Poisson process with mean arrival rate λ. The output of the model represents the time points for ventricular activation, and thus the differences between adjacent elements in the output vector represent the RR intervals.

2.2 ECG data

The RATe control in Atrial Fibrillation (RATAF) study Ulimoen et al. (2013) acquired 24-hour ambulatory ECGs during baseline and under the influence of four rate control drugs; the two calcium channel blockers verapamil and diltiazem, and the two β-blockers metoprolol and carvedilol. The study population consists of 60 patients with permanent AF, no heart failure, or symptomatic ischemic heart disease. The study was approved by the regional ethics

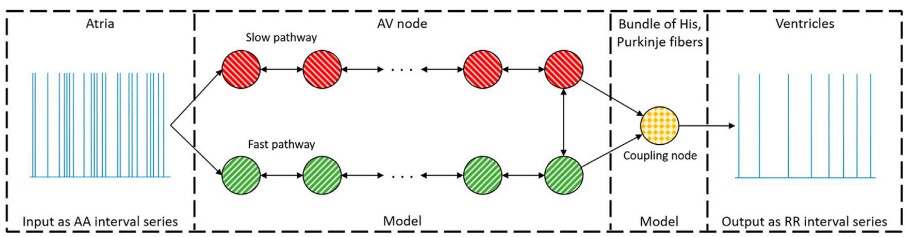

FIGURE 2
A schematic representation of the network model where the yellow node represents the coupling node, the red nodes the SP, the green nodes the FP, and arrows the direction for impulse conduction. For readability, only a subset of the 21 nodes is shown.

committee and the Norwegian Medicines Agency and conducted in accordance with the Helsinki Declaration. The trend in the AV node refractory period and conduction delay from these five 24-hour ECG recordings per patient is assessed by estimations of the trends in $\boldsymbol{\theta}$.

2.3 ECG processing

The RR interval series is extracted from the ECG, where RR intervals following and preceding QRS-complexes with deviating morphology are excluded from the series Lagerholm et al. (2000). Due to excessive noise in the ECGs, some RR intervals are missed, leading to an unrealistically low heart rate. Thus, the data are divided into minute-long non-overlapping segments, and all segments with a heart rate lower than 20 bpm are removed, occasionally resulting in gaps in the signals. The signals with a total duration shorter than 12 h or with less than 20 h between start and end are excluded from further analysis. After excluding data according to these criteria, data from 59 patients remained for inclusion in this study. The number of patients with data considered to be of sufficient duration for analysis and the average duration of these recordings for the different treatments are shown in Table 2.

The f-waves in the ECG are extracted using spatiotemporal QRST cancellation Stridh and Sornmo (2001). The AFR trends are then estimated by tracking the fundamental frequency of the extracted f-wave signal using a hidden Markov model-based approach Sandberg et al. (2008); resulting in a resolution for the AFR trends of one minute.

2.4 Parameter estimation

The atrial arrival rate, λ, is estimated by correcting the AFR trend, taking the atrial depolarization time into account Corino et al. (2013). Outliers in the estimated λ trends are excluded based on visual inspection guided by cluster analysis. The resulting trends are low-pass filtered using a sliding triangular window filter with a width equal to 70.

The model parameters $\boldsymbol{\theta}$ are assumed to vary over time, making this a dynamic optimization problem. Thus, the data are first divided into overlapping data segments of $N = 1000$ RR intervals; where N is chosen to give a good balance between resolution and robustness of the estimates. Each data segment contains one segment-specific mean arrival rate $\lambda^N(i)$ calculated as the mean of the λ trend in the segment starting at RR interval i, as well as one RR interval series, $\boldsymbol{RR}^N(i)$. The estimated parameters of a data segment starting at RR interval i is denoted by $\hat{\boldsymbol{\theta}}(i)$.

A fitness function based on the Poincaré plot - a scatter plot of successive pairs of RR intervals - is used to quantify the difference between observed and simulated RR series. The Poincaré plots are binned into two-dimensional bins with a width of 50 m, centered between 250 and 1800 m, forming a two-dimensional histogram. The error function (ϵ), i.e., the inverse fitness function, is then calculated from the number of samples in the bins according to Eq. 4,

$$\epsilon = \frac{1}{K}\sum_{k=1}^{K}\frac{\left(x_k^N - \frac{N}{N_{sim}}\tilde{x}_k^{N_{sim}}\right)^2}{\sqrt{\frac{N}{N_{sim}}\tilde{x}_k^{N_{sim}}}}, \tag{4}$$

where K is the number of bins, N_{sim} is the number of RR intervals simulated with the model, and x_k^N and $\tilde{x}_k^{N_{sim}}$ are the numbers of RR intervals in the k-th bin of the observed data and model output, respectively.

A genetic algorithm (GA) is used to search for the values of $\boldsymbol{\theta}$ yielding the minimum ϵ. A GA consists of a population of individuals that evolves based on their fitness value towards a solution using selection, crossover, and mutation Wahde (2008).

By assuming that a large change in the Poincaré plot relates to a large change in parameter values, it is possible before starting the optimization to decide when the optimization algorithm should focus on exploration or exploitation. As a heuristic for this, we introduce the difference in the Poincaré plots ($\Delta P(i)$), according to Eq. 5,

TABLE 2 The number of recordings and recording length (mean ± std) analyzed in this study following exclusion of recordings with insufficient signal quality, as described in Section 2.3.

Drug	Number of recordings	Recordings length (h)
Baseline	51	20.88 ± 2.85
Verapamil	53	21.92 ± 2.39
Diltiazem	56	21.71 ± 2.44
Metoprolol	53	21.87 ± 1.98
Carvedilol	57	21.23 ± 2.65
Total	270	21.52 ± 2.59

$$\Delta P(i) = \frac{1}{K}\sum_{k=1}^{K}\left(x_k^{N_{\Delta P}}(i) - x_k^{N_{\Delta P}}(i+1000)\right)^2, \quad (5)$$

where $x_k^{N_{\Delta P}}(i)$ and $x_k^{N_{\Delta P}}(i+1000)$ are the number of RR intervals in the k-th bin of the Poincaré plot for the RR interval series starting at interval i and $i + 1000$, respectively. Moreover, the segment length $N_{\Delta P}$ is set to 2000. The Poincaré plot difference, $\Delta P(i)$, is used to tune hyper-parameters in the optimization algorithm.

The GA used for estimating $\hat{\boldsymbol{\theta}}(i)$ has a population size of 400 individuals - where each individual is a vector of values for $\boldsymbol{\theta}$ - and uses tournament selection, a two-point crossover, and creep mutation Wahde (2008). The number of generations the GA runs before switching to the next data segment varies from 1 when $\Delta P(i) < 800$; to 2 when $800 \leq \Delta P(i) < 2000$; to 3 when $\Delta P(i) \geq 2000$. The step size for the sliding windows is determined by the trade-off between the resolution and the computing cost, and is set to 108 s; resulting in 800 steps for full 24-hour measurements. Thus, there will be 800 estimated $\hat{\boldsymbol{\theta}}(i)$ for a 24-hour measurement. As noted previously, there are also gaps in the data. Thus, the step size will partly vary to match the start and end of the RR segments, to ensure that all data are used. For reference, estimating the $\hat{\boldsymbol{\theta}}(i)$ trend from a 24-hour RR and λ series using a single core on a standard desktop computer (Intel® Core™ i7-6600U Processor, @ 2.60 GHz) requires on average 4 hours.

Since the Poisson process used to create the model input is stochastic, ϵ varies between realizations. This variation is dependent on the number of RR intervals generated from the model, where more RR intervals reduce the variation but require more computing power. To have a good balance between computing power and stability, N_{sim} is set to 1500. However, the ten fittest individuals in each generation are re-evaluated, with $N_{sim} = 5000$, before the individual with the best fit for each data segment, $\hat{\boldsymbol{\theta}}(i)$, is saved.

The individuals for the first generation are randomly initialized using a latin hypercube sampling in the ranges: $\{R_{\min}^{SP}, R_{\min}^{FP}\} \in [150, 650]\ ms$; $\{\Delta R^{SP},\ \Delta R^{FP}\} \in [0,\ 700]\ ms$; $\{\tau_R^{SP}, \tau_R^{FP}\} \in [40, 300]\ ms$; $\{D_{\min}^{SP}, D_{\min}^{FP}\} \in [0, 30]\ ms$; $\{\Delta D^{SP},\ \Delta D^{FP}\} \in [0,\ 75]\ ms$; $\{\tau_D^{SP}, \tau_D^{FP}\} \in [40, 300]\ ms$. These values are also used as boundaries for the model parameters. Hence, the difference between the upper bound and the lower bound for the parameters is the range that the parameters can vary within, here denoted $r(p)$ and in vector form $\boldsymbol{r}$, where p is the parameter index ordered as in $\boldsymbol{\theta}$.

To reduce the risk of premature convergence and to maintain a good diversity in the population, immigrants - individuals not created from the current population - are used. These immigrants are created using three different methods; 1) by saving and then re-using the ten most fit individuals and their model output per generation; 2) by running eight computationally faster GA, using only 16 individuals and $N_{sim} = 750$, simultaneously; and 3), by random sampling. The number of immigrants is dependent on $\Delta P(i)$ and is created in equal proportion using the three different creation methods. These new individuals are then introduced into the population at the start of every new data segment by replacing the individuals with the lowest fitness. More specific details about the GA are found in Supplementary Material, Section 1.

2.5 Parameter uncertainty estimation

A variant of Sobol's method Sobol (2001) is used to derive the uncertainty for each estimated parameter set $\hat{\boldsymbol{\theta}}(i)$. The contribution to the output variance ($v(p)$) for a parameter p, including the variation caused by its interaction with all the other parameters, is estimated by the following procedure. Firstly, two 30 x 12 matrices ($\boldsymbol{A}$ and $\boldsymbol{B}$), where 30 is the number of sampled parameter vectors, are generated by samples from a quasi Monte Carlo procedure based on the Latin hypercube design. Unlike Sobol's method - which samples in the whole parameter range - these samples are generated within $\hat{\boldsymbol{\theta}}(i) \pm 0.075\boldsymbol{r}$, hence within a hyper-rectangle covering 15% of the total range of each parameter. Secondly, 12 new matrices, $\boldsymbol{AB}_p$ are created by replacing the p-th column in $\boldsymbol{A}$ with the p-th from $\boldsymbol{B}$. Thirdly, ϵ is calculated for each parameter set in the matrices by running the model, before the expected value of the contribution to the output variance is estimated according to Eq. 6 Sobol (2001).

$$\hat{v}(p) = \frac{1}{2\cdot 30}\sum_{q=1}^{30}\left(\epsilon_{A_q} - \epsilon_{AB_{pq}}\right)^2. \quad (6)$$

Here ϵ_{A_q} and $\epsilon_{AB_{pq}}$ quantifies the difference between the observed RR series and the model output as given in Eq. 4, for the parameter sets in $\boldsymbol{A}$ and $\boldsymbol{AB}_p$, respectively.

The estimated $\hat{v}(p)$ are then, together with the mean ($\bar{\epsilon}$) and standard deviation (σ_ϵ) of the 30 realizations of $\hat{\boldsymbol{\theta}}(i)$, used to calculate a parameter uncertainty estimate according to Eq. 7.

$$u(p) = \frac{0.15r(p)}{\sqrt{\hat{v}(p)} - \sigma_\epsilon}0.1\bar{\epsilon}. \quad (7)$$

Here $0.15r(p)$ originates from the distance between $\hat{\boldsymbol{\theta}}(i)$ and the border of the sampled hyper-space, and $\sqrt{\hat{v}(p)} - \sigma_\epsilon$ from the difference between the error variation inside the hyper-space and at $\hat{\boldsymbol{\theta}}(i)$. Hence, the fraction relates to the slope-intercept between the parameter distance and the uncertainty. The remaining product relates this slope to 10% of the mean error for $\hat{\boldsymbol{\theta}}(i)$. Thus, the interpretation of $u(p)$ is: 'Assuming interaction between all model parameters, how large a step can be taken for parameter p before the contribution to ϵ for $\hat{\boldsymbol{\theta}}(i)$ is increased by 10%'. This was then repeated for all $\hat{\boldsymbol{\theta}}(i)$ for all patients and drugs.

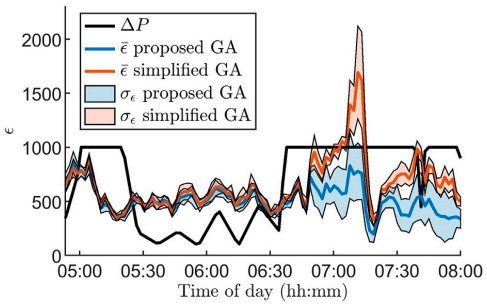

FIGURE 3
Mean (colored lines) and standard deviation (colored areas) of the error ϵ for 100 segments for the proposed genetic algorithm (blue) and a standard genetic algorithm (red) together with the Poincare difference $\Delta P(i)$ (black line), defined in Eq. 5, for data from one patient at baseline during 3 hours. The standard deviation and mean are based on ten runs of the algorithms. Note that $\Delta P(i)$ is scaled with $\frac{1}{5}$ for readability.

2.6 Circadian variation

The drug-dependent circadian variation for the estimated AV node parameters is quantified using linear mixed-effect modeling, i.e., using a statistical model comprising both fixed effects and random effects. The model used consists of a 24-hour periodic cosine with mean $\boldsymbol{m}$, amplitude $\boldsymbol{a}$, and phase $\boldsymbol{\phi}$, as seen in Eqs. 8, 9, and 10.

$$\boldsymbol{y}_{pat,m}(t) = \boldsymbol{m}_{pat,m} + \boldsymbol{a}_{pat,m} \cos\left(\frac{2\pi}{24}t + \boldsymbol{\phi}\right) \tag{8}$$

$$\boldsymbol{m}_{pat,m} = \boldsymbol{\alpha} + \boldsymbol{\alpha}_m + \boldsymbol{\eta}_{pat} + \boldsymbol{\eta}_{pat,m} \tag{9}$$

$$\boldsymbol{a}_{pat,m} = \boldsymbol{\beta} + \boldsymbol{\beta}_m + \boldsymbol{\xi}_{pat} + \boldsymbol{\xi}_{pat,m} \tag{10}$$

Here $\boldsymbol{y}_{pat,m}(t)$ represents the estimated parameter trends of patient *pat* during treatment $m \in$ {Baseline, Verapamil, Diltiazem, Metoprolol, Carvedilol}. Moreover, t corresponds to the time of the day, in hours, of the RR interval i that the estimated $\hat{\boldsymbol{\theta}}(i)$ relates to. Furthermore, $\boldsymbol{\alpha}$, $\boldsymbol{\alpha}_m$, $\boldsymbol{\beta}$, and $\boldsymbol{\beta}_m$ represent the fixed-effects; with $\boldsymbol{\alpha}$ and $\boldsymbol{\beta}$ corresponding to the mean value for the mean and amplitude during baseline, and $\boldsymbol{\alpha}_m$ and $\boldsymbol{\beta}_m$ to the average deviation from the baseline values, caused by the drugs. The random effects $\boldsymbol{\eta}_{pat}$, $\boldsymbol{\eta}_{pat,m}$, $\boldsymbol{\xi}_{pat}$, and $\boldsymbol{\xi}_{pat,m}$ correspond to the individual deviation from the fixed-effects, and are assumed to be sampled from a zero-mean gaussian distribution. During baseline, $\boldsymbol{\alpha}_m$, $\boldsymbol{\beta}_m$ and $\boldsymbol{\eta}_{pat,m}$, $\boldsymbol{\xi}_{pat,m}$ are assumed to be zero. For a given individual, $\boldsymbol{\phi}$ is assumed to be equal for all 12 model parameters and is estimated by means of principal component analysis of the $\hat{\boldsymbol{\theta}}(i)$ trends. The 12 vectors created by projecting the data onto the 12 principal components are fitted to a cosine with mean m_c, amplitude a_c, and phase ϕ_c, where c indicates the c-th principal component, using the simplex search method Lagarias et al. (1998). The phase, ϕ, is set equal to the ϕ_c associated with the highest a_c. Moreover, for cases where $\boldsymbol{a}_{pat,m}$ is negative, a phase-shift of π is added to ensure that all the amplitudes are positive.

With $\boldsymbol{\phi}$ estimated, $\boldsymbol{\alpha}$, $\boldsymbol{\alpha}_m$, $\boldsymbol{\beta}$, $\boldsymbol{\beta}_m$, $\boldsymbol{\eta}_{pat}$, $\boldsymbol{\eta}_{pat,m}$, $\boldsymbol{\xi}_{pat}$, and $\boldsymbol{\xi}_{pat,m}$ are fitted using the linear mixed-effects model function 'fitlme ()' in MATLAB (The MathWorks Inc. Version R2019b); using the full covariance matrix with the Cholesky parameterization and the maximum likelihood for estimating parameters of the linear mixed-effects model with trust region based quasi-Newton optimizer as settings.

An assessment of the goodness of fit for the linear mixed-effect model is calculated as the RMSE between the modeled cosine and the estimated parameters. For easier comparison between parameters, the RMSE for each parameter is weighted by their respective range, $r(p)$.

2.7 Statistic analysis

The estimated parameters $\hat{\boldsymbol{\theta}}(i)$, as well as AFR and HR, were averaged for each recording, and significant difference between the averages at baseline and under the four drugs were assessed one-by-one using the paired two-sided Wilcoxon signed rank test Woolson (2007) with the Benjamini–Hochberg correction Benjamini and Hochberg (1995). Patients with missing recordings (cf. Table 2) at baseline or the drug in question were excluded from the analysis. A p-value below 0.05 after correction was considered significant.

3 Results

Figure 3 illustrates the advantages of using the GA proposed in Section 2.4 for parameter estimation by comparing it to a standard version of the GA. For the standard GA, all hyper-parameters, as well as the number of generations per data segment, are fixed and thus do not take advantage of $\Delta P(i)$. To highlight the differences between the algorithms, we zoom in on a three hour long segment where the RR series characteristics change rapidly. It is clear that ϵ increases along with $\Delta P(i)$ for the standard GA, in contrast to the proposed GA.

From the GA we acquire one estimate per data segment, for all 59 patients and all drugs, resulting in a total of 175,640 $\hat{\boldsymbol{\theta}}(i)$. To give the reader a sense of the match between the model output and RR interval series obtained from the ECG, we present two examples of Poincaré plots and histograms together with the associated RR interval series. One corresponds to the median ϵ, and one where ϵ is higher than 95% of all ϵ, as shown in Figure 4. It is evident that the histograms and Poincaré plots from the model output and data are similar for both cases, indicating a good match to data in most data segments. However, there is a considerable difference on a beat-to-beat level, as indicated by the RR interval series. Moreover, $\hat{\boldsymbol{\theta}}(i)$ for one patient at baseline is shown in Figure 5, where clear changes over time can be seen.

TABLE 3 Recording averages of estimated model parameters, AFR, and HR at baseline and during treatment with the four different drugs (mean ± standard deviation). Differences from baseline are evaluated using the Wilcoxon signed rank test with the Benjamini–Hochberg correction; significant difference from baseline for the drugs, with false discovery rate at 0.05, is indicated with *.

Parameter	Baseline	Verapamil	Diltiazem	Metoprolol	Carvedilol
$R^{FP}_{\min}$ (ms)	435 ± 139	488 ± 134*	518 ± 118*	489 ± 126*	476 ± 123*
ΔR^{FP} (ms)	403 ± 195	478 ± 190*	488 ± 202*	495 ± 180*	483 ± 172*
τ^{FP}_{R} (ms)	175 ± 59	165 ± 63	163 ± 64	162 ± 58	167 ± 57
$R^{SP}_{\min}$ (ms)	241 ± 102	280 ± 125*	287 ± 124*	260 ± 114	269 ± 123
ΔR^{SP} (ms)	231 ± 176	274 ± 201	301 ± 215*	312 ± 187*	274 ± 186*
τ^{SP}_{R} (ms)	180 ± 60	183 ± 62	171 ± 63	176 ± 62	176 ± 63
$D^{FP}_{\min}$ (ms)	5.3 ± 4.5	5.4 ± 4.8	5.4 ± 4.7	5.9 ± 4.5	5.3 ± 4.5
ΔD^{FP} (ms)	18.9 ± 16.9	21.7 ± 17.2	22.1 ± 17.3	21.8 ± 16.7	21.4 ± 16.9
τ^{FP}_{D} (ms)	141 ± 54	144 ± 50	145 ± 53	149 ± 50	142 ± 53
$D^{SP}_{\min}$ (ms)	21.0 ± 5.3	21.6 ± 5.1	22.5 ± 5.2*	21.7 ± 4.8	21 ± 5.2
ΔD^{SP} (ms)	26.3 ± 21.4	23.8 ± 20.9	19.6 ± 20.7*	22.6 ± 21.2	21.5 ± 20.8
τ^{SP}_{D} (ms)	185 ± 68	184 ± 57	183 ± 65	186 ± 58	180 ± 65
HR (bpm)	95 ± 13	80 ± 12*	74 ± 10*	81 ± 10*	84 ± 11*
AFR (Hz)	4.96 ± 0.34	4.56 ± 0.45*	4.71 ± 0.44*	4.86 ± 0.40*	4.81 ± 0.51*

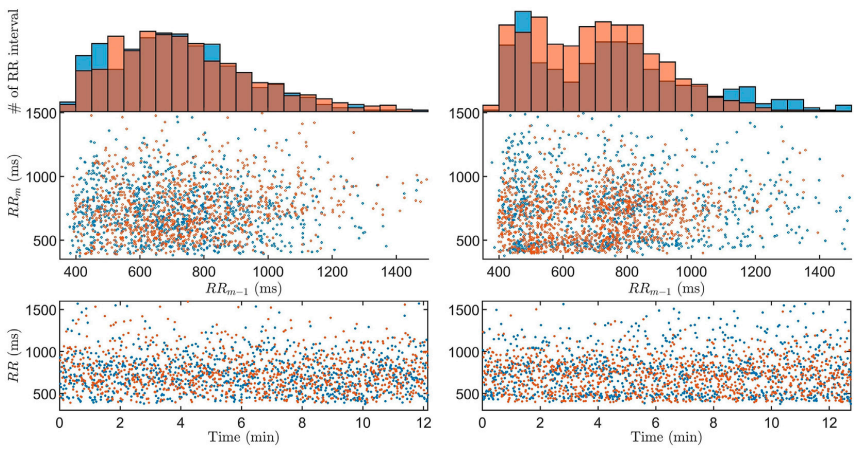

FIGURE 4
The Poincaré plot with associated histogram and RR interval series of data (blue) and model output (orange) for the $\hat{\theta}(i)$ corresponding to the median ϵ (left) and to the $\hat{\theta}(i)$ which ϵ is higher than 95% of all ϵ (right).

Recording averages of estimated model parameters, AFR, and HR at baseline and during treatment with the four different drugs are shown in Table 3. Significant differences, as described in Section 2.7, are indicated in the table by "*". This shows a significant increase in the refractory period in the FP for all drugs, as well as a significant decrease in heart rate and AFR for all drugs.

3.1 Uncertainty estimation

The average $u(p)$, as explained in Eq. 7, normalized with $r(p)$, are shown in Figure 6. From this, it is evident that the model parameters relating to the SP are more robustly estimated than their FP counterpart, and that the model parameters relating to the

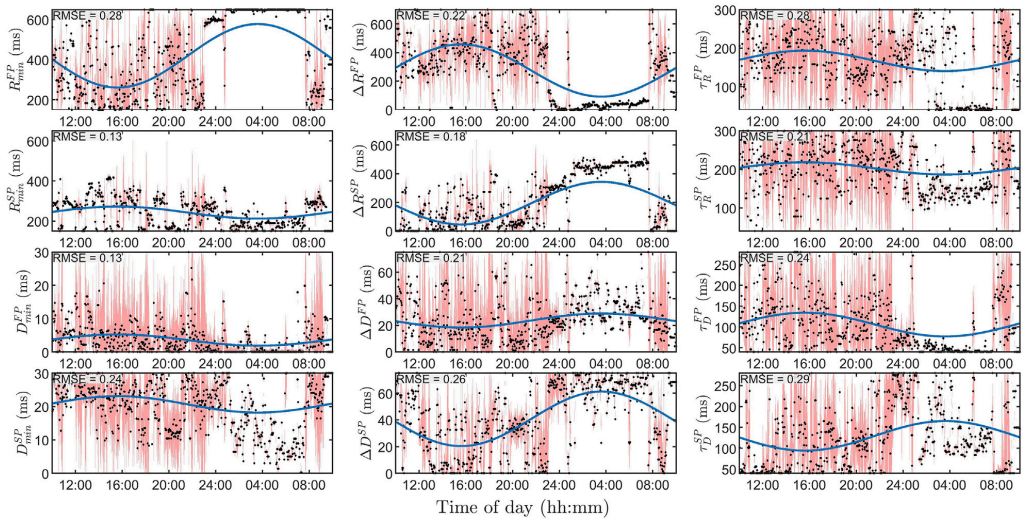

FIGURE 5
Estimated model parameters $\hat{\boldsymbol{\theta}}(i)$ (black dots), with corresponding uncertainty estimates *PU* (red areas), along with the fitted cosine (blue lines) used for the circadian variation, for one patient during baseline. In each panel, the RMSE is reported as a measure of goodness of fit between $\hat{\boldsymbol{\theta}}(i)$ and the fitted cosine. Left column shows the parameters relating to the minimum conduction delay or refractory period, the middle column the parameters relating to the maximum prolongation, and the right column to the time constants. For further explanation of the model parameters, see Table 1.

refractory period are more robustly estimated than their conduction delay counterpart. Most noteworthy is the lower uncertainty for R^{SP}_{min} and ΔR^{SP}, suggesting a higher impact on the output of the model.

The uncertainty estimates, $u(p)$, for one patient are shown as red background for each $\hat{\boldsymbol{\theta}}(i)$ in Figure 5, where again $u(p)$ for the refractory parameters in the SP is lower. There is also a clear difference in $u(p)$ between nighttime and daytime, where the uncertainty is much lower at night.

3.2 Circadian variation

In Figure 5 we also show an example of the circadian variation (blue lines) for the aforementioned patient, as explained in Eqs. 8, 9, and 10, where a clear distinction between night and day can be seen for most parameters. The average RMSE for the 12 model parameters seen in Figure 5 is 0.22, which can be compared with the average RMSE for all patients and treatment of 0.16 ± 0.03 (mean ± std).

The mean and standard deviation of the circadian variation phase ϕ was 1.03 ± 0.74 rad; corresponding to an extreme value at approximately 04:00 am ± 2.8 h.

The fixed-effects $\boldsymbol{\alpha}_m$ and $\boldsymbol{\beta}_m$ and their respective 95% confidence interval, normalized with $r(p)$, are shown in Figure 7, where the fixed-effects represent the average difference in effect with respect to baseline that the drugs have on the population. It is evident from $\boldsymbol{\alpha}_m$ in Figure 7 (top panel) that all rate control drugs on average increase the refractory period in both pathways; with a significant increase ($p < 0.05$) in R^{FP}_{min} and Δ^{FP} for all drugs, in R^{SP}_{min} for all but metoprolol, and in ΔR^{SP} for all but verapamil. Moreover, differences between the β-blockers and the calcium channel blockers can be observed. Most noticeably for the amplitude ($\boldsymbol{\beta}_m$) of ΔD^{FP} and ΔD^{SP}, where the two β-blockers have a distinctly negative effect in comparison with the two calcium channel blockers.

Detailed results for the estimated fixed and random effects can be found in the Supplementary Material, Section 2.

4 Discussion

In this study, we have presented a mathematical framework able to continuously estimate model parameters representing the conduction delay and refractory period of the AV node during 24 h for patients with permanent AF from ECG data. Trends in the estimated model parameters were analyzed using a mixed-effects model to study the circadian variation, where drug-dependent differences could be seen.

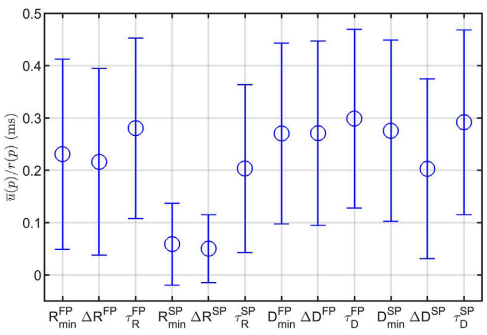

FIGURE 6
Mean (circles) ± one standard deviation (bars) of the parameter uncertainty estimates $u(p)$ over all recordings and all patients, normalized with the parameter ranges $r(p)$. Note that the model parameters R^{SP}_{min} and ΔR^{SP} have a lower uncertainty, indicating a higher impact on the resulting model outcome.

The model has previously been shown to be able to represent measured data in the form of histograms and Poincaré plots for 20-min long segments Karlsson et al. (2021). However, continuously estimating model parameters representing the refractory period and conduction delay in the AV node has previously not been possible. A previous study of the RR interval series has indicated that one interval delay in the autocorrelation gives sufficient information to replicate the dynamics of the RR interval series Karlsson et al. (2021). Hence, the Poincaré plot was chosen as a basis for the fitness function in order to take the one interval delay of the RR interval series into account, something that is not possible with an one-dimensional distribution representation such as the histogram. Moreover, since the model describes the impulses from the atria as a stochastic process, it is not possible to have a beat-to-beat level of detail in the fitness function, as evident by the RR interval series in Figure 4.

The choice of segment length N is a trade-off between robustness and time-resolution. The segment length N was set to 1000 RR intervals, corresponding to a time duration of 11 : 53 ± 03 : 28 (mm:ss), to capture changes in RR series characteristics on this time-scale while allowing sufficient estimation accuracy. As a consequence of the choice of N = 1000, the bin size of 50 m was used for the Poincaré plot-based error function. A smaller bin size would allow a more detailed match between model output and data, but would require more RR intervals.

From Figure 4, it is evident that the model and workflow can replicate the histogram and Poincaré plot of obtained RR interval series even for the case with the 95% highest ϵ. This was made possible by using the problem-specific GA presented in Section 2.4. Evolutionary algorithms - such as GA - and particle swarm optimization are the most common optimization algorithms used for solving dynamic optimization problems Yazdani et al. (2021); Mavrovouniotis et al. (2017).

One of the main challenges with dynamic optimization problems is the balance between exploration and exploitation, i.e., between searching for different promising regions of the search space, or searching for the optimal solutions within an already promising region. To keep a good level of exploration, the diversity in the population - usually defined as the average Euclidean distance between the individuals in the population - is often monitored. Thus, diversity loss is one of the most critical challenges Yazdani et al. (2021). A great number of methods have been developed to address this diversity loss, often based on randomizing individuals in the population that are too similar to others. For example, crowding - letting new individuals replace

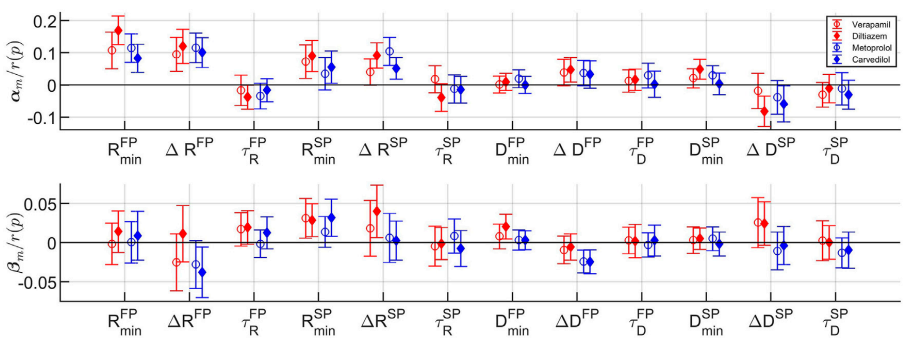

FIGURE 7
The fixed effects with corresponding 95% confidence intervals for the cosinor mean ***m*** (top) and cosinor amplitude ***a*** (bottom) for each model parameter (cf. Table 1) and drug. Confidence intervals not overlapping zero indicate significant difference from baseline (p <0.05).

the most similar individual in the population Kordestani et al. (2014) - or based on the age of the individuals Das et al. (2013). For GA, it is also possible to combat diversity loss by regulating the mutation rate. However, maintaining a good level of exploration using diversity does not take any information about the data into account. In contrast, changing the mutation rate, the number of immigrants, and the number of generations per segment using $\Delta P(i)$ - as was done in this study - takes information about the data directly into account. Additionally, the number of immigrants in the proposed GA ranges from 10–70%, which limits the initialization's effect on the overall results. Moreover, the results in Figure 3 indicate that the proposed problem-specific optimization method yields a better fit compared to the standard approach when the characteristics of the data change rapidly. On the other hand, when the characteristics of the data change slowly, the performance is similar even though the proposed algorithm is using fewer generations per segment. The number of RR intervals simulated with the model for each parameter set, N_{sim}, was set to 1500 in the GA based on a trade-off between computational complexity and variation based on the stochastic input sequence to the model. A simulation study relating the variation in ϵ and N_{sim} which was used to guide the decision is shown in the Supplementary Material, Section 1. Moreover, the thresholds for ΔP to determine how many generations are to be run per data segment were set so that approximately 55% are run for 1 generation, 30% are run for 2 generations, and the remaining 15% are run for 3.

A variation of Sobol's method was used to estimate the contribution to output variance for each model parameter, which was related to an increase in error by 10%. This more complex methodology was preferred over a one-at-a-time approach due to the large effect that interaction between model parameters has on the model output. Note that, unlike more traditional uncertainty estimates, this is not directly connected to a probability, since the error function used does not have a proper probabilistic interpretation. Thus, the uncertainty shall only be interpreted as a relative measure between the model parameters, between patients, and between the time of day. For example, it is evident in Figure 5 that the uncertainty for this patient is much lower during nighttime than daytime.

A linear mixed-effect model based on a cosinor analysis was used to derive the circadian variations. This method was used to quantify the circadian variation for the different drugs over the whole population, as well as the individual response to the drugs. The focus of this study is on the population effects of the different drug types in order to understand the drug-dependent differences in the conduction properties, something that needs to be understood before the method could be applicable on an individual level. Even though the focus of this study is on the population level, the individual responses are still of interest, especially for future work. For example, to predict individual responses to different drugs. As shown in Figure 5, the individual match is not optimal, thus a better tool for capturing the circadian variation is believed to be needed before robust analysis on an individual level is feasible. However, the cosinor analysis is an established model for characterizing circadian variation and has previously been used on the RATAF data-set to study heart rate variation Corino et al. (2015a).

From Table 3, in the parameters $R^{FP}_{\min}$ and ΔR^{FP}, we see a significantly increased refractory period relative to baseline in the FP for all four drugs. In addition, a significant increase in the SP for either $R^{SP}_{\min}$, or ΔR^{SP} could also be seen for all drugs. This increase is also visible in the fixed effect parameters $\boldsymbol{\alpha}_m$ in Figure 7, top panel. Electrophysiological studies of the two calcium channel blockers verapamil and diltiazem as well as the β-blocker metoprolol have shown that the drugs increase the refractoriness in the AV node Leboeuf et al. (1989); Talajic et al. (1992); Rizzon et al. (1978). Moreover, carvedilol has been shown to increase the effective refractory period in the atria during AF Kanoupakis et al. (2004). However, to the best of our knowledge, no studies have been conducted to determine the effect of carvedilol specifically for the refractory period in the AV node. Furthermore, conduction properties in the atria influence the model through the mean arrival rate λ, and thus affect the estimated parameters.

In addition, from Figure 7 bottom panel, it is shown that the two β-blockers reduce the circadian variation of the conduction delay more than the calcium channel blockers, as evident by ΔD^{FP} and ΔD^{SP}. Stimulation of the β_1-receptors - regulated by the autonomic nervous system - have been shown to increase the conduction velocity in the AV node Gordan et al. (2015). Hence, blocking this receptor using β-blocking drugs might decrease the autonomic nervous system effect, and thus reduce the circadian variation, yielding the presented results.

Also seen in Figure 7, the model parameters for the two β-blockers often behave similarly. However, the model parameters for the calcium channel blockers verapamil and diltiazem do not always align. In fact, the values for $\boldsymbol{\alpha}_m$ and $\boldsymbol{\beta}_m$ for verapamil are in several cases - most noticeably for $R^{FP}_{\min}$ for $\boldsymbol{\alpha}_m$ and ΔR^{FP}, ΔR^{SP}, and $D^{FP}_{\min}$ for $\boldsymbol{\beta}_m$ - similar to those of the two β-blockers. Interestingly, it has previously been proposed that the pharmacological effects of verapamil may partly be due to some degree of β-blockade Drici et al. (1993).

Moreover, the large confidence intervals in Figure 7, where the majority includes zero, are most likely due to the high inter-patient variability in parameter values. A confidence interval that includes zero would indicate that there is no significant difference from baseline. The high inertia and simplicity of the cosine are other factors in this. For example, some patients have more than one section with parameter values close to those during the night - possibly due to periods of sleep during the day - which a cosine with a period of 24 h could not capture.

4.1 Study limitations and future perspectives

The present model of the AV node accounts for dual pathway physiology and rate dependent changes in conduction delay and refractoriness and can simulate retrograde conduction. However, it is not able to simulate some physiological interesting phenomena such as AV node re-entry.

A limited range for the model parameters was used to make the optimization more efficient. The choice of the boundaries was guided by electrophysiological measurements from previous clinical studies while keeping a conservative range to not exclude realistic values. The maximal refractory period for the model - given as the sum of $R_{\min}$ and ΔR - lies in the range [150, 1350] ms and was set to include the effective refractory period of the AV node, which has been reported as 361 ± 57 and 283 ± 48 m for the FP and SP, respectively Natale et al. (1994). Furthermore, the conduction delay of the whole model is given by the sum of $D_{\min}$ and ΔD multiplied by the number of nodes, which lies in the range [0, 1050] ms. Thus, it includes all realistic PR intervals, which rarely exceed 200 m Schumacher et al. (2017). Even though the boundaries were conservatively chosen, we cannot exclude the possibility that a different choice would have affected the resulting parameter values. Moreover, since the parameters might be hard to interpret, combining the model parameters associated with the same conduction property, i.e., the two refractory periods and the two conduction delays, to create more interpretable representations, is interesting.

As mentioned before, high inertia and simplicity of the cosine are limiting factors for the assessment of circadian variation. However, the cosinor analysis is an established model for characterizing circadian variation and is thus important for clear and interpretable results. Using the estimated uncertainty to weight the estimated parameters is one possible approach to make the cosine fit the estimates better. Other methods to capture the differences in the AV node parameters over time, such as time-frequency analysis of the estimated parameter trends, should also be investigated.

It should be noted that the estimated model parameters are not clinically validated for assessment of AV node refractoriness and conduction delay. Hence, the clinical significance of the results should be interpreted with caution. However, the overall findings for the different drugs on the whole population are, as discussed above, in accordance with electrophysiological studies. Another limitation is the sample size of 60 patients in combination with the high inter-patient variability in parameter values, as seen in the large standard deviation in Table 3. This makes the population estimates more uncertain, partly causing the large confidence intervals seen in Figure 7.

A natural continuation of this work is to analyze the estimated model parameters during baseline, possible in combinations with other factors such as age or gender, to predict the mean heart rate under the influence of the different drugs. This in turn could be used to assist in personalized treatment selection during AF.

5 Conclusion

We have presented a framework - including a mathematical model and a genetic algorithm - which for the first time enables characterization of the refractory period and the conduction delay of the AV node during 24 h for patients with permanent AF, solely based on non-invasive data.

With ECG from AF patients during baseline and under the influence of different rate control drugs, a mixed-model framework was used on the estimated model parameters to compare the impact on circadian variation between drugs. From this, differences in conduction delay could be identified between β-blockers and calcium channel blockers, which was previously unknown.

Data availability statement

The data analyzed in this study is subject to the following licenses/restrictions: The estimated model parameters $\boldsymbol{\theta}_{(i)}$ and associated uncertainty estimate u(p) supporting the conclusions for this article will be available from MK upon request. The ECG data are owned by Vestre Viken Hospital Trust, and requests for access can be made to SU. The code for the model together with an user example can be found at https://github.com/FraunhoferChalmersCentre/AV-node-model.

Ethics statement

The studies involving human participants were reviewed and approved by Regional ethics committee and the Norwegian Medicines Agency. The patients/participants provided their written informed consent to participate in this study.

Author contributions

MK, FS, and MW contributed to the conception and design of the study. SU was responsible for the clinical study. FS was responsible for the ECG pre-processing and estimation of the RR interval series and AFR trends. MK wrote the manuscript and designed the genetic algorithm, the method for the uncertainty estimation, and the circadian variation model, with advice, suggestions, and supervision from FS and MW. PP and SU analyzed and gave medical interpretations of the results. FS and MW supervised the project and reviewed the manuscript during the whole writing process. All authors contributed to manuscript revision, read, and approved the submitted version.

Funding

This work was supported by the Swedish Foundation for Strategic Research (Grant FID18-0023), the Swedish Research Council (Grant VR 2019–04272), and the Crafoord Foundation (Grant 20200605).

Conflict of interest

The authors declare that the research was conducted in the absence of any commercial or financial relationships that could be construed as a potential conflict of interest.

Publisher's note

Supplementary material

The Supplementary Material for this article can be found online at: https://www.frontiersin.org/articles/10.3389/fphys.2022.976526/full#supplementary-material

References

Benjamin, E. J., Muntner, P., Alonso, A., Bittencourt, M. S., Callaway, C. W., Carson, A. P., et al. (2019). Heart disease and stroke statistics-2019 update a report from the American heart association. *Circulation* 139, e56–e528. doi:10.1161/CIR.0000000000000659

Benjamini, Y., and Hochberg, Y. (1995). Controlling the false discovery rate: A practical and powerful approach to multiple testing. *J. R. Stat. Soc. Ser. B Methodol.* 57, 289–300. doi:10.1111/j.2517-6161.1995.tb02031.x

Billette, J., and Nattel, S. (1994). Dynamic behavior of the atrioventricular node: A functional model of interaction between recovery, facilitation, and fatigue. *J. Cardiovasc. Electrophysiol.* 5, 90–102. doi:10.1111/j.1540-8167.1994.tb01117.x

Climent, A. M., Guillem, M. S., Husser, D., Castells, F., Millet, J., and Bollmann, A. (2010). Role of the atrial rate as a factor modulating ventricular response during atrial fibrillation. *Pacing Clin. Electrophysiol.* 33, 1510–1517. doi:10.1111/j.1540-8159.2010.02837.x

Climent, A. M., Guillem, M. S., Zhang, Y., Millet, J., and Mazgalev, T. (2011). Functional mathematical model of dual pathway av nodal conduction. *Am. J. Physiol. Heart Circ. Physiol.* 300, H1393–H1401. doi:10.1152/ajpheart.01175.2010

Corino, V. D., Platonov, P. G., Enger, S., Tveit, A., and Ulimoen, S. R. (2015a). Circadian variation of variability and irregularity of heart rate in patients with permanent atrial fibrillation: Relation to symptoms and rate control drugs. *Am. J. Physiol. Heart Circ. Physiol.* 309, H2152–H2157. doi:10.1152/ajpheart.00300.2015

Corino, V. D., Sandberg, F., Lombardi, F., Mainardi, L. T., and Sörnmo, L. (2013). Atrioventricular nodal function during atrial fibrillation: Model building and robust estimation. *Biomed. Signal Process. Control* 8, 1017–1025. doi:10.1016/j.bspc.2012.10.006

Corino, V. D., Sandberg, F., Mainardi, L. T., and Sornmo, L. (2011). An atrioventricular node model for analysis of the ventricular response during atrial fibrillation. *IEEE Trans. Biomed. Eng.* 58, 3386–3395. doi:10.1109/TBME.2011.2166262

Corino, V. D., Ulimoen, S. R., Enger, S., Mainardi, L. T., Tveit, A., and Platonov, P. G. (2015b). Rate-control drugs affect variability and irregularity measures of rr intervals in patients with permanent atrial fibrillation. *J. Cardiovasc. Electrophysiol.* 26, 137–141. doi:10.1111/jce.12580

Das, S., Mandal, A., and Mukherjee, R. (2013). An adaptive differential evolution algorithm for global optimization in dynamic environments. *IEEE Trans. Cybern.* 44, 966–978. doi:10.1109/TCYB.2013.2278188

Di Carlo, A., Bellino, L., Consoli, D., Mori, F., Zaninelli, A., Baldereschi, M., et al. (2019). Prevalence of atrial fibrillation in the Italian elderly population and projections from 2020 to 2060 for Italy and the European Union: The fai project. *Europace* 21, 1468–1475. doi:10.1093/europace/euz141

Drici, M., Jacomet, Y., Iacono, P., and Lapalus, P. (1993). Is verapamil also a non-selective beta blocker? *Int. J. Clin. Pharmacol. Ther. Toxicol.* 31, 27–30.

Gordan, R., Gwathmey, J. K., and Xie, L.-H. (2015). Autonomic and endocrine control of cardiovascular function. *World J. Cardiol.* 7, 204–214. doi:10.4330/wjc.v7.i4.204

Henriksson, M., Corino, V. D., Sörnmo, L., and Sandberg, F. (2015). A statistical atrioventricular node model accounting for pathway switching during atrial fibrillation. *IEEE Trans. Biomed. Eng.* 63, 1842–1849. doi:10.1109/TBME.2015.2503562

Hindricks, G., Potpara, T., Dagres, N., Arbelo, E., Bax, J. J., Blomström-Lundqvist, C., et al. (2021). 2020 ESC guidelines for the diagnosis and management of atrial fibrillation developed in collaboration with the European association for cardio-thoracic surgery (EACTS) the task force for the diagnosis and management of atrial fibrillation of the European society of cardiology (ESC) developed with the special contribution of the European heart rhythm association (EHRA) of the ESC. *Eur. Heart J.* 42, 373–498. doi:10.1093/eurheartj/ehaa612

Inada, S., Hancox, J., Zhang, H., and Boyett, M. (2009). One-dimensional mathematical model of the atrioventricular node including atrio-nodal, nodal, and nodal-his cells. *Biophys. J.* 97, 2117–2127. doi:10.1016/j.bpj.2009.06.056

Jørgensen, P., Schäfer, C., Guerra, P. G., Talajic, M., Nattel, S., and Glass, L. (2002). A mathematical model of human atrioventricular nodal function incorporating concealed conduction. *Bull. Math. Biol.* 64, 1083–1099. doi:10.1006/bulm.2002.0313

Kanoupakis, E. M., Manios, E. G., Mavrakis, H. E., Tzerakis, P. G., Mouloudi, H. K., and Vardas, P. E. (2004). Comparative effects of carvedilol and amiodarone on conversion and recurrence rates of persistent atrial fibrillation. *Am. J. Cardiol.* 94, 659–662. doi:10.1016/j.amjcard.2004.05.037

Karlsson, M., Sandberg, F., Ulimoen, S. R., and Wallman, M. (2021). Non-invasive characterization of human av-nodal conduction delay and refractory period during atrial fibrillation. *Front. Physiol.* 12, 728955. doi:10.3389/fphys.2021.728955

Kordestani, J. K., Rezvanian, A., and Meybodi, M. R. (2014). Cdepso: A bi-population hybrid approach for dynamic optimization problems. *Appl. Intell. (Dordr).* 40, 682–694. doi:10.1007/s10489-013-0483-z

Lagarias, J. C., Reeds, J. A., Wright, M. H., and Wright, P. E. (1998). Convergence properties of the Nelder–Mead simplex method in low dimensions. *SIAM J. Optim.* 9, 112–147. doi:10.1137/s1052623496303470

Lagerholm, M., Peterson, C., Braccini, G., Edenbrandt, L., and Sornmo, L. (2000). Clustering ecg complexes using hermite functions and self-organizing maps. *IEEE Trans. Biomed. Eng.* 47, 838–848. doi:10.1109/10.846677

Leboeuf, J., Lamar, J., Massingham, R., and Ponsonnaille, J. (1989). Electrophysiological effects of bepridil and its quaternary derivative cerm 11888 in closed chest anaesthetized dogs: A comparison with verapamil and diltiazem. *Br. J. Pharmacol.* 98, 1351–1359. doi:10.1111/j.1476-5381.1989.tb12684.x

Mangin, L., Vinet, A., Pagé, P., and Glass, L. (2005). Effects of antiarrhythmic drug therapy on atrioventricular nodal function during atrial fibrillation in humans. *Europace* 7, S71–S82. doi:10.1016/j.eupc.2005.03.016

Mase, M., Disertori, M., Marini, M., and Ravelli, F. (2017). Characterization of rate and regularity of ventricular response during atrial tachyarrhythmias. insight on atrial and nodal determinants. *Physiol. Meas.* 38, 800–818. doi:10.1088/1361-6579/aa6388

Masè, M., Glass, L., Disertori, M., and Ravelli, F. (2012). Nodal recovery, dual pathway physiology, and concealed conduction determine complex av dynamics in human atrial tachyarrhythmias. *Am. J. Physiol. Heart Circ. Physiol.* 303, H1219–H1228. doi:10.1152/ajpheart.00228.2012

Masè, M., Marini, M., Disertori, M., and Ravelli, F. (2015). Dynamics of av coupling during human atrial fibrillation: Role of atrial rate. *Am. J. Physiol. Heart Circ. Physiol.* 309, H198–H205. doi:10.1152/ajpheart.00726.2014

Mavrovouniotis, M., Li, C., and Yang, S. (2017). A survey of swarm intelligence for dynamic optimization: Algorithms and applications. *Swarm Evol. Comput.* 33, 1–17. doi:10.1016/j.swevo.2016.12.005

Natale, A., Klein, G., Yee, R., and Thakur, R. (1994). Shortening of fast pathway refractoriness after slow pathway ablation. effects of autonomic blockade. *Circulation* 89, 1103–1108. doi:10.1161/01.cir.89.3.1103

Rizzon, P., Di Biase, M., Chiddo, A., Mastrangelo, D., and Sorgente, L. (1978). Electrophysiological properties of intravenous metoprolol in man. *Br. Heart J.* 40, 650–655. doi:10.1136/hrt.40.6.650

Sandberg, F., Stridh, M., and Sornmo, L. (2008). Frequency tracking of atrial fibrillation using hidden markov models. *IEEE Trans. Biomed. Eng.* 55, 502–511. doi:10.1109/TBME.2007.905488

Schumacher, K., Dagres, N., Hindricks, G., Husser, D., Bollmann, A., and Kornej, J. (2017). Characteristics of pr interval as predictor for atrial fibrillation: Association with biomarkers and outcomes. *Clin. Res. Cardiol.* 106, 767–775. doi:10.1007/s00392-017-1109-y

Shrier, A., Dubarsky, H., Rosengarten, M., Guevara, M. R., Nattel, S., and Glass, L. (1987). Prediction of complex atrioventricular conduction rhythms in humans with use of the atrioventricular nodal recovery curve. *Circulation* 76, 1196–1205. doi:10.1161/01.cir.76.6.1196

Sobol, I. M. (2001). Global sensitivity indices for nonlinear mathematical models and their Monte Carlo estimates. *Math. Comput. Simul.* 55, 271–280. doi:10.1016/s0378-4754(00)00270-6

Stridh, M., and Sornmo, L. (2001). Spatiotemporal qrst cancellation techniques for analysis of atrial fibrillation. *IEEE Trans. Biomed. Eng.* 48, 105–111. doi:10.1109/10.900266

Sun, J., Amellal, F., Glass, L., and Billette, J. (1995). Alternans and period-doubling bifurcations in atrioventricular nodal conduction. *J. Theor. Biol.* 173, 79–91. doi:10.1006/jtbi.1995.0045

Talajic, M., Lemery, R., Roy, D., Villemaire, C., Cartier, R., Coutu, B., et al. (1992). Rate-dependent effects of diltiazem on human atrioventricular nodal properties. *Circulation* 86, 870–877. doi:10.1161/01.cir.86.3.870

Ulimoen, S. R., Enger, S., Carlson, J., Platonov, P. G., Pripp, A. H., Abdelnoor, M., et al. (2013). Comparison of four single-drug regimens on ventricular rate and arrhythmia-related symptoms in patients with permanent atrial fibrillation. *Am. J. Cardiol.* 111, 225–230. doi:10.1016/j.amjcard.2012.09.020

Wahde, M. (2008). *Biologically inspired optimization methods: An introduction*. Southampton: WIT press.

Woolson, R. F. (2007). *Wilcoxon signed-rank test*. Wiley encyclopedia of clinical trials, 1–3.

Yazdani, D., Cheng, R., Yazdani, D., Branke, J., Jin, Y., and Yao, X. (2021). A survey of evolutionary continuous dynamic optimization over two decades—Part a. *IEEE Trans. Evol. Comput.* 25, 609–629. doi:10.1109/tevc.2021.3060014

LUND UNIVERSITY

Licentiate Dissertation
ISBN: 978-91-8039-483-3 (print)
ISBN: 978-91-8039-484-0 (electronic)
ISRN: LUTEDX/TEEM – 1132– SE
Report-nr: 5/22